uOttawa

L'Université canadienne
Canada's university

FACULTÉ DES ÉTUDES SUPÉRIEURES ET POSTOCTORALES

uOttawa

L'Université canadienne
Canada's university

FACULTY OF GRADUATE AND POSDOCTORAL STUDIES

Bahram Zargar

AUTEUR DE LA THÈSE / AUTHOR OF THESIS

M.A.Sc. (Mechanical Engineering)

GRADE / DEGREE

Department of Mechanical Engineering

FACULTÉ, ÉCOLE, DÉPARTEMENT / FACULTY, SCHOOL, DEPARTMENT

Model Development, Validation and Nonlinear Control of Pneumatic Suspensions

TITRE DE LA THÈSE / TITLE OF THESIS

Dr. A. Fahim

DIRECTEUR (DIRECTRICE) DE LA THÈSE / THESIS SUPERVISOR

Dr. A. Jnifene

CO-DIRECTEUR (CO-DIRECTRICE) DE LA THÈSE / THESIS CO-SUPERVISOR

EXAMINATEURS (EXAMINATRICES) DE LA THÈSE / THESIS EXAMINERS

Dr. N. Baddour

Dr. R. Langlois

Gary W. Slater

Le Doyen de la Faculté des études supérieures et postdoctorales / Dean of the Faculty of Graduate and Postdoctoral Studies

Model Development, Validation and Nonlinear Control of Pneumatic Suspensions

Thesis Submitted

to The School of Graduate Studies

in partial fulfillment of the requirements for

the Degree of Masters in Applied Sciences

in Mechanical Engineering

By

Bahram Zargar

January 2007

Ottawa-Carleton Institute for

Mechanical and Aerospace Engineering

University of Ottawa

Ottawa, Ontario, Canada K1N 6N5

Your file Votre référence
ISBN: 978-0-494-32492-9
Our file Notre référence
ISBN: 978-0-494-32492-9

Abstract

Pneumatic suspensions are widely used at present in the truck industry. The passive controllability of the parameters of these suspensions makes them suitable for load adapted suspensions. However, active control of these systems is challenging because of their parameter uncertainties and their highly nonlinear behavior. The ultimate goal of this research is to develop an active pneumatic suspension system to improve the ride comfort and performance of car suspensions. For this purpose, dimensional analysis was applied to the half car model of the Honda Civic. The conventional suspension of the Honda Civic was replaced by a pneumatic suspension. Its scaled half car model was designed and built. The parameters of the air spring were identified by carrying out a series of static experiments and frequency analysis on the physical air spring/load system. The mathematical model was validated by experimental results. Different nonlinear controllers were applied to the mathematical model of a quarter car Honda Civic equipped with an active pneumatic suspension. The first order sliding mode feedback linearization controller (SMFLC) with parameter estimator offers the best ride comfort and performance. The performance of this controller is further studied on the half car model in the presence of different model uncertainties.

Acknowledgement

I would like to extend my deepest acknowledgement and gratefulness to all my teachers and professors, from my childhood till now who made me a better citizen of the world.

Foremost I would like to express my sincere gratitude and appreciation to my supervisor and co-supervisor, Dr. Atef Fahim and Dr. Amor Jnifene for providing me with the unique opportunity to work on this challenging topic, and for sharing their knowledge and wisdom with me. I appreciate their expert guidance and mentorship, and their constructive comments.

I also thank many of my friends for making my stay in the University of Ottawa memorable.

Finally, I wish to express my most loving thanks to my dear and understanding wife, Maryam, whose support throughout my research made it possible.

Last but not least, I thank my family specially my parents, my first teachers who taught me how to live. Who not only taught me the alphabet of life but also raised me to learn. I cannot find enough words to thank for their continuous everlasting support since my birth till today.

Table of Contents

List of Figures

List of Tables

Nomenclauture

^	superscript denoting the estimated variables and parameters
~	superscript denoting the parameter estimation error
α	angle of the force with horizontal axis
α_v	vertical root mean square acceleration
α_t	transverse root mean square acceleration
θ	pitch angle
θ_d	desired pitch angle of the reference model
λ	triple pole
λ_f	forgetting factor
λ_0	initial forgetting factor
v	summation of the power products of the different output derivatives
ξ	damping ratio
π	Pi-number
Π_1	stiffness Pi-number
Π_2	damping Pi-number
Π_3	force Pi-number
Π_4	inertia Pi-number
ρ_1	density of air in air supply
ρ_2	density of the air at this cross section
ϕ	boundary layer thickness
Φ_k	independent random phase angle
Ψ	functions of known parameters
ω_{np}	pitch natural frequency
ω_{nb}	bounce natural frequency
ω_n	natural frequency
Ω	spatial frequency
a	distance between front axle to the center of mass of the car body

$\boldsymbol{a}$	vector of unknown parameters
A	air spring effective area
A	maximum area of orifice
$\hat{A}$	estimated effective area
A_{12}	inlet orifice area
A_{23}	outlet orifice area
$\overline{A}_{12}$	dimensionless inlet orifice are
$\overline{A}_{23}$	dimensionless outlet orifice are
$\mathbf{A_{eff}}$	effective area at 100 psig and recommended design height
$\overline{A}_{eff}$	dimensionless effective area
A_{mean}	mean effective area
A_k	amplitude
A_p	effective projected area
b	distance between rear axle to the center of mass of the car body
B_r	damping coefficient of rear suspension
B_r	damping coefficient of front suspension
c	damping coefficient
c_1, c_2	constants
C_B	scale factor of damping
C_d	scale factor of orifice diameter
C_F	scale factor of force
C_K	scale factor of stiffness
C_L	scale factor of length
C_m	scale factor of mass
C_P	scale factor of pressure
C_T	time scale factor
C_{Te}	scale factor of temperature
e	tracking error
E	expected value
E	tracking error vector

$\mathbf{e}_1$	prediction error vector
"f"	parameters subscripts of the front axle
f	temporal frequency
F	force
F_0	payload supported by air spring in atmosphere pressure
F_c	optimized actuator force
F_l	force exerted to the payload by the air spring
F_y	force in y direction
$G(\Omega)$	one sided spatial PSDs
h	air spring height
$\mathbf{h}$	maximum assembly height of the air spring
J	moment of inertia
k	smallest order of the output derivative in which the input appears
k_0	maximum value of the magnitude of $\mathbf{P}$
K	constant
$\mathbf{K}$	sliding mode gain matrix
K_A	stiffness of air spring
K_i	control gain corresponding to i^{th} derivative of the output
K_a	acceleration gain
K_f	spring stiffness of front suspension
K_p	proportional gain
K_r	spring stiffness of rear suspension
K_{tr}	stiffness of rear tire
K_{tf}	stiffness of front tire
K_v	velocity gain
K_s	sliding mode gain
L	length dimension
l	length
m	mass
M	mass dimension
M_2	mass of air in air spring

$\hat{m}_s$	estimated sprung mass
M_s	sprung mass
m_{ur}	rear unsprung mass
m_{uf}	front unsprung mass
m_s	mass supported by air spring
n	polytropic process coefficient
N_{12}	ratio of inlet and critical mass flow rates
N_{23}	ratio of outlet and critical mass flow rates
P	pressure
$\mathbf{P}(t)$	estimator gain matrix
p	estimator gain
P_1	stagnation pressure (total pressure)
P_2	air spring pressure
$\overline{P}_{21}$	the ratio of air spring pressure to the air supply pressure
$\overline{P}_{32}$	the ratio of atmospheric pressure to the air spring pressure
P_I	performance index was defined
p_i	dimension of ith element in the dimensional table
r	is the desired reference input
"r"	parameters subscripts of the rear axle
R	gas constant
$\mathbf{R}$	reference input vector
r_{mean}	mean radius of air spring cross section
r_y	radius of gyration of the sprung mass
$\mathbf{S}$	sliding function vector
$S(\Omega)$	power spectral density
S	function of the tracking error
T	time dimension
T_1	total temperature
T_2	air spring temperature
T_3	the temperature of atmosphere
Te	temperature dimension
t_d	time delay

Tr	transmissibility
U	unit
$\mathbf{U}$	input vector
u	input of the system
u_c	control input
$\mathbf{U}_c$	control input vector
u_2	air velocity at the inlet orifice
V	vehicle velocity
V_0	ratio of surge tank volume to air spring volume
V_2	air spring volume
$\mathbf{V_2}$	air spring volume at 100 psig and recommended design height
$\overline{V}_2$	dimensionless air spring volume
V_l	Lyapunov function
w	temporal angular frequency
w_k	discrete frequency
$\mathbf{w}$	air spring natural frequency at 100 psig and recommended design height
$\boldsymbol{W}$	functions of known variables
w_0	wheel natural frequency
W_{12}	mass flow rate at inlet orifice
W_{12}	mass flow rate at outlet orifice
W_{cr}	critical mass flow rate
y	system output
$\mathbf{Y}$	output vector
$\boldsymbol{Y}$	vector of measurable variables
y_d	model reference output
$\mathbf{Y}_d$	desired output vector of the reference model
Y_i	logarithm of the dimension of ith element in the dimensional table
X	state vector
z	heave
Z_1, Z_2, Z_3	logarithm of basic units
Z_{cm}	height of the center of mass the () and the

$\overline{Z}_r$	dimensionless road roughness
Z_{rf}	road unevenness exciting the front axle
Z_{rr}	road unevenness exciting the rear axle
Z_s	vertical position of mass supported by air spring
$\overline{Z}_s$	dimensionless sprung mass displacement
$\hat{\ddot{Z}}_s$	estimated sprung mass acceleration
Z_{sd}	desired heave displacement of the reference model
$\overline{Z}_u$	dimensionless unsprung mass displacement

CHAPTER 1

Introduction

1.1 Motivation

According to World Health Organization, around 1.2 million people are killed in car accidents and around 50 million get injured each year. A significant percent of these accidents can be prevented by improving the vehicle stability using more reliable suspension systems. Suspension systems not only play a significant role in vehicle stability and handling, but also they are responsible for drivers and passengers ride comfort. Different types of suspension systems have been developed to improve ride comfort and handling stability of vehicles. But these two criteria are dramatically opposite to each other. Thus increasing handling stability decreases ride comfort and vice versa. This problem led the motor vehicle industry to actively explore a new generation of active suspension system for consumer vehicles. In active suspensions, the stiffness and damping ratio of the suspension system are tuned based on the ride condition to guarantee both ride comfort and handling stability. Among all developed suspension systems, those with controllable and adjustable parameters are candidates for active suspensions. One of these is the pneumatic suspension. Pneumatic suspensions are favored because of their high payload capacity, durability and ability for self-leveling. At present, the majority of heavy duty vehicles manufactured are equipped with this type of suspension.

Pneumatic cylinders were used in the first generation of pneumatic suspensions. They were replaced later by the flexible walled pneumatic spring as the rubber technology capitalized on the idea. This new generation of pneumatic springs is known simply as the air spring. Even though air springs have many advantages over pneumatic cylinders, their flexible wall makes their mathematical model imprecise and highly nonlinear. Therefore, conventional controllers are not applicable to them and robust nonlinear controllers are required to improve the suspension performance.

1.2 Objective and Methodology

The ultimate goal of this research is to apply a robust and reliable controller to pneumatic suspension system to improve ride comfort. To reach this goal, it is vital to understand different sources of model uncertainty in the mathematical model of an air spring. The mathematical model should be verified by physical air spring/load system experimentation. Applying a judiciously chosen set of nonlinear controllers to a simple quarter car model and comparing their performances, is a useful exercise to choose the most promising one for further study. The controller with the best performance and ride comfort would then be applied to the pneumatic half car model of the Honda Civic equipped with pneumatic spring suspension to verify its performance.

1.3 Thesis Outline

A literature survey was conducted on ride comfort, presented in Chapter 2. The papers are categorized by their subjects. The literature survey covers most of the topics, helpful in developing a realistic nonlinear control for pneumatic suspension. The covered topics are: comfort criteria, road profile modeling, suspensions types, vehicle suspension models, pneumatic vibration isolator, air spring modeling and pneumatic active suspensions.

In Chapter 3, the mathematical model of a conventional half car model is presented. The dimensional analysis is applied, and the scaling laws required to develop a similitude scaled model are derived. The parameters of the Honda Civic are scaled down based on the obtained scaled laws. The proper air spring is chosen based on the scaled stiffness. A 2M2A Firestone air spring is chosen to replace the conventional spring/damper. Finally, the designed and built scaled half car model of the Honda Civic is presented.

The mathematical model of an air spring, quarter car and half car models equipped with pneumatic springs are presented in Chapter 4. Dimensional analysis is applied to

the mathematical models of these systems. The dimensionless mathematical models are derived. The scaling laws to build the similitude scale models of these systems are also presented.

Chapter 5 presents the identification of the air spring parameters and model validation. The experimental setup, used to perform different static and dynamic experiments on the 2M2A Fireston air spring, is presented. The static characteristics of the air spring are obtained through a series of static experiments. Based on the obtained data, the effective areas for different pressures and air spring assembly heights are inferred. The behaviour of effective area is analyzed. The frequency responses of the air spring are obtained under different pressures and payloads. The linear mathematical model of the air spring is identified for each pair of payloads and pressures. The possibility of modeling the air spring by a single linear or quasilinear mathematical model is discussed. The frequency responses of the physical air spring/load system and its nonlinear mathematical model are compared. The sensitivity analysis is conducted on the mathematical model of the air spring.

Chapter 6 consists of two sections. In the first section, the road profile is simulated as a Gaussian random signal. The algorithms of feedback linearization control, model reference control, and different types of sliding mode control and parameter estimator are presented. These controllers are applied to the quarter car model with pneumatic suspension with different types of uncertainties, such as uncertainty in volume, effective area, and assembly height of the air spring. Their performances are compared. Their sensitivity curves are plotted and compared. The effect of the payload variation on the parameter estimator is discussed. In the second part of Chapter 6, the controller with the best performance in the first section is applied to the half car model and its performance is discussed.

CHAPTER 2

Literature Review

2.1 Introduction

Ride comfort is an active field of research that covers many topics. Among these are road profiling, human body vibration, vehicle dynamics, and passive, active and semi-active suspension systems. In early studies on ride comfort, the road was usually simulated as a sinusoidal, triangular or step function, but later it has been shown that the road profile is more like a random signal than a simple periodic or aperiodic function. Since then, road profiling itself became a branch of research that involves stochastic analysis in order to find a proper model for the road profile that can be used for design and simulation purposes. Human body vibration and research aimed at criteria for expressing ride comfort has been on going since 1930. Reiher and Meister [1] were the first to develop such a criterion in 1930's. The second ride comfort criterion known as Janeway's comfort was developed in 1965. Smith and Simong's research in 1975 and Healey's works are some significant works in this field which is still an active branch of research.

The research on passive suspension is mostly focused on optimizing the suspension system parameters. In fact, as new optimization methods are developed, they are applied to the car suspension to improve the ride comfort. However, currently, active and semi-active suspensions are the most active researched topics on suspension. The research on these topics is mostly focused on applying new control techniques to these suspension systems and investigating new types of dampers which can be easily controlled to filter road roughness more efficiently.

The most significant works on finding ride comfort criteria are presented in the following section.

2.2 Ride Comfort Criteria

The ability of the human body to withstand vibration and the search for reasonable criteria for ride comfort have been the subjects of many studies; five significant works in this area were reviewed and are reported here.

2.2.1 Reiher and Meister Criterion

In early 1930s, Reiher and Meister [1] introduced 6 tolerance ranges for the human body under vibration. Their criterion is based on experimental results carried out on 25 people between the ages of 20 to 37. Each person was exposed to sinusoidal vertical or horizontal movement on a shaking table for 10 minutes at different frequencies. The tolerance ranges are classified as imperceptible, slightly perceptible, distinctly perceptible, strongly perceptible (annoying), unpleasant (disturbing), and very disturbing (injurious). Figure 2.1 illustrate the six different tolerance ranges introduced by Reiher and Meister. The tolerance to vibration decreases as the frequency increases. The experimental results prove that human body tolerates low frequencies better than high frequencies.

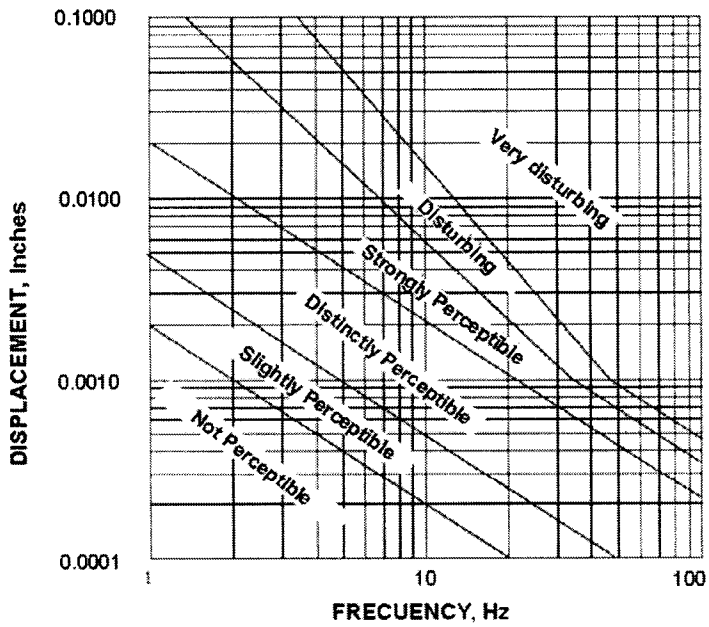

Figure 2.1: Six tolerance level by Reiher and Meister [2]

2.2.2 Janeway's Comfort Criterion

In 1957, Janeway et al [3] introduced a new criterion for ride comfort. This became latter to be known as Janeway's Criteria. The Janeway's comfort criterion considers three ranges of frequency and introduces different ride comfort measures for each range. Between 1-6 Hz the peak value of "jerk" (the multiplication of the amplitude and the cube of the circular frequency) has been used as a measure and its maximum amplitude should not exceed 12.6 m/s^3 (496 in/s^3). In the range of 6 to 20 Hz, the measure used is "acceleration" (the product of the amplitude and the square of the circular frequency) and its value should be less than 0.33 m/s^2 (13 in/s^2). The measure used in the range of 20 to 60 Hz is the peak value of "velocity" (the product of the amplitude and the circular frequency), and its magnitude should not exceed 2.7 mm/s (0.105 in/s).

2.2.3 Smith et al Research

In 1976, Smith et al [4] showed experimentally that the root mean square (rms) acceleration is an excellent measure for ride comfort. They correlated the rms acceleration with the mean ride rating of 78 raters for two different cars, a 1974 Buick Century and a Ford Maverick. The experiments were carried out on 18 sections of roads with different roughnesses. The mean rating for each section was obtained and linearly correlated with the rms acceleration for that section.

Figure 2.2 shows the main result of Smith and his co-authors. The horizontal axis is the mean personal rating numbered from 1 to 5; with 5 being the rate for the best ride comfort and 1 being that to the worst one. The figure shows that the small rms acceleration range corresponds to the best ride comfort and that high rms acceleration range corresponds to the worst ride comfort. Curve fitting of the obtained data show that the Mean Personal Rating (MPR) is a function of the rms acceleration and given by:

$$MPR = 5.43 - 40(\alpha_v^{\,2} + \alpha_l^{\,2})^{\frac{1}{2}} \qquad 2.1$$

where α_v and α_t are the vertical and transverse rms acceleration in g unit respectively.

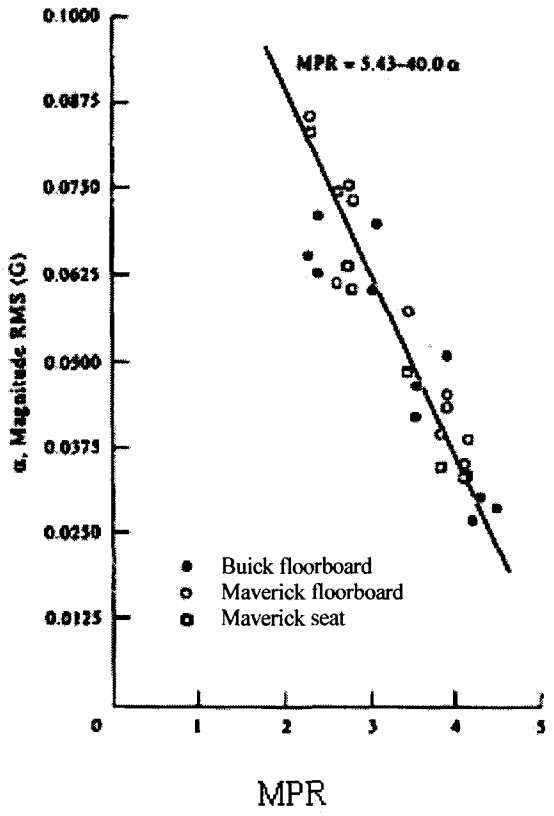

Figure 2.2: Least Square curve fit to experimental rms accelerations versus mean personal ratings (Smith et al 1976[4]) taken from[5]

2.2.4 ISO 2631 Standard for Ride Comfort

While several standards on ride comfort exist, only that of the ISO 2631 [6] is reported here. Figures 2.3 and 2.4 show fatigue limits introduced by the International Standards Organization (ISO) in 1972. Figure 2.3 shows the reduced proficiency limits for vertical vibration in terms of root mean square value (rms) of acceleration. The graph shows that the human vibration tolerance depends on four factors: magnitude, frequency, duration, and direction of vibration. The tolerance boundary decreases as duration increases but the shape of the curves stays the same. These curves can be used to adjust workers efficiency. Whenever health or safety limits are desired, the curves are shifted up by a factor of 6 dB. When comfort limits are required the curves are shifted down by

a factor of 10 dB. The curves also show that the frequency field in which human body is more affected lie between 4 and 8 Hz.

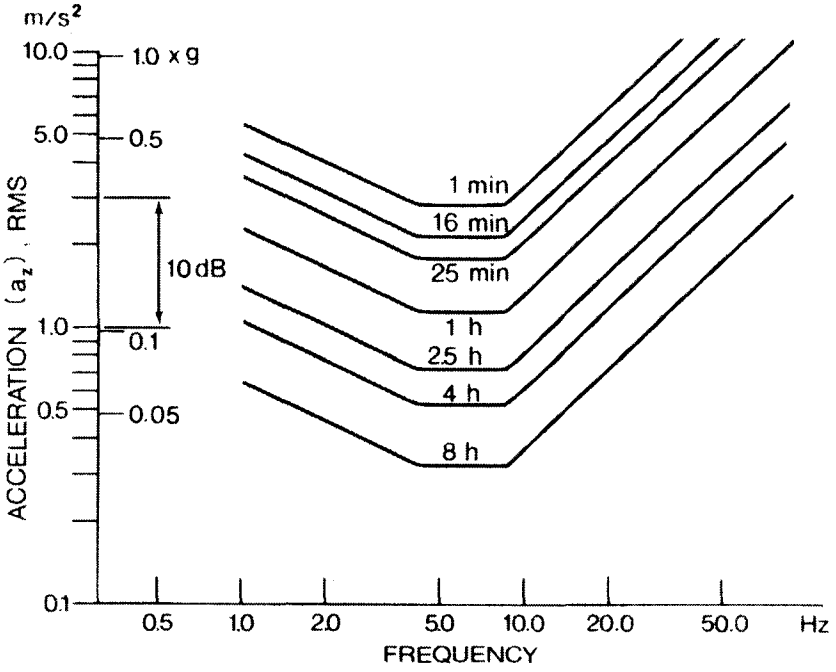

Figure 2.3: Limits of whole-body vibration for fatigue in vertical direction [5]

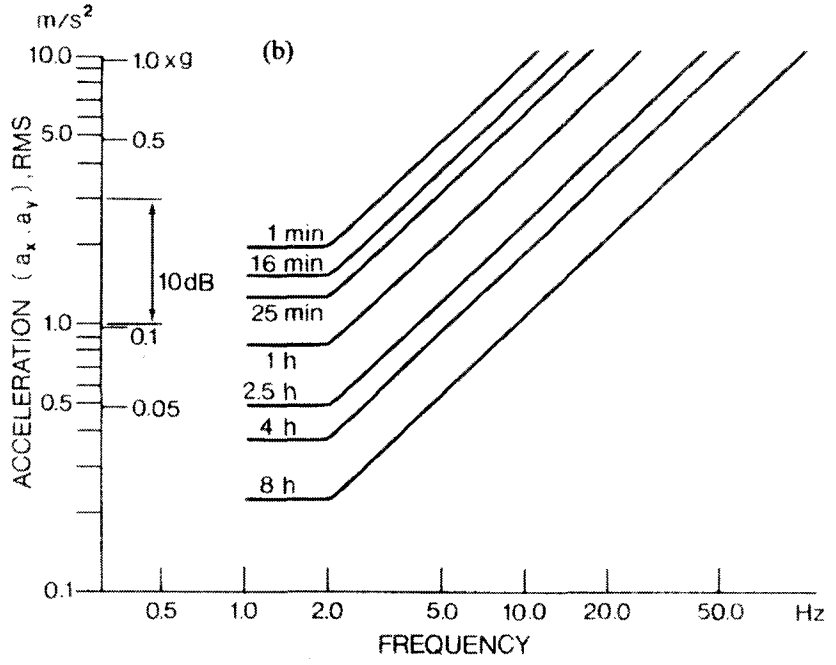

Figure 2.4: Limits of whole-body vibration for fatigue in transverse direction [5]

The curves are straight lines at low frequency, indicating that jerk is constant. As such, for low frequency, jerk can be used as a good criterion for ride comfort. However at high frequency the lines are parallel to the bisector of the first quadrant, indicating that the amplitude of the velocity is constant. Therefore the ISO fatigue limits verify the Janeway's criterion.

Frequencies less than 1 Hz produce sensations which can be related to motion sickness. Above 80 Hz, the effect of vibration depends very much on the part of the body under study and on the skin conditions, as local vibrations become the governing factor to give general guidelines. There are also resonance fields at which some parts of the body vibrate with large amplitudes. For example the thorax-abdomen resonance frequency is around 3-6 Hz, while that for the head-neck-shoulder combination is around 20-30 Hz. The resonance frequency of the eyeballs is around 60-90 Hz and that for the jaw-skull system around is 100-220 Hz [7].

2.2.5 Healey's Results

In 1977 Healey [8] carried out a series of experiments on a 1974 Buick Century sedan traveling at a constant speed of 50 m/h (80 km/h) on several different roadways. The roads were categorized as rough, medium and smooth. Rough roadways correspond to secondary roads; medium roads correspond to average quality US highways, and smooth roadways correspond to US interstate highways. The vertical and lateral acceleration were measured using a box fitted with accelerometers fixed beneath the driver's seat. The one-third octave rms values were compared to the ISO guide for one hour and eight hours fatigue decreased proficiency. Three considerable peaks could be distinguished on the drawn plots. Healey has interpreted these peaks as follows: The peak at 1 Hz corresponds to combined body modes of heave, pitch and roll, while the peak around 12-18 Hz corresponds to wheel axle bounce and roll modes, and finally the peak around 30 Hz is associated with flexible body modes and tire non-uniformity. The experiments on the Buick show that the one-third octave rms acceleration spectra lie

below the 8-hour ISO guide in both the low and high range except for the rough roadway.

Moreover, Healey has compared the experimental results for the Buick and the Ford Maverick on a very smooth section of US highway 290 and concluded that the smaller car, the Ford Maverick, has higher vibration levels at 2 Hz and 18 Hz for the vertical acceleration and at 18 Hz for the lateral acceleration.

He has summarized the obtained result in a table. Table 2.1 shows the values of rms acceleration in both vertical and lateral direction for rough, medium and smooth roads with their corresponding rating range.

Table 2.1 Root mean square for Buick on three roadways with different roughness

Road	Vertical	Lateral	Rating Range
Rough	>.055 rms g	>.024 rms g	2-3
Medium	.03 to .055 rms g	.015 to .024 rms g	3-4
Smooth	<.03 rms g	<.015 rms g	4-5

2.3 Road Profile Modeling

Without having a realistic model of the road, simulating a vehicle suspension to study the ride comfort and road handling is useless; therefore, modeling the road unevenness itself is an area of research and many papers have been published during the past four decades. ElBeheiry in 1995 has listed 52 papers on this subject in his literature survey bibliography paper [9]. Early researchers have simulated road roughness as a step function, rectangular or sinusoidal signal but later research showed that road roughness resembles more a random signal than other types of signals. ISO has classified the road profiles into 8 separate groups and introduced their power spectra density as shown in Figure 2.5. "A" stands for a very good profile and "H" for a very rough one [10].

Even though the random signal is the most realistic road unevenness model, step signals are widely used in simulation to compare the behavior of different suspensions.

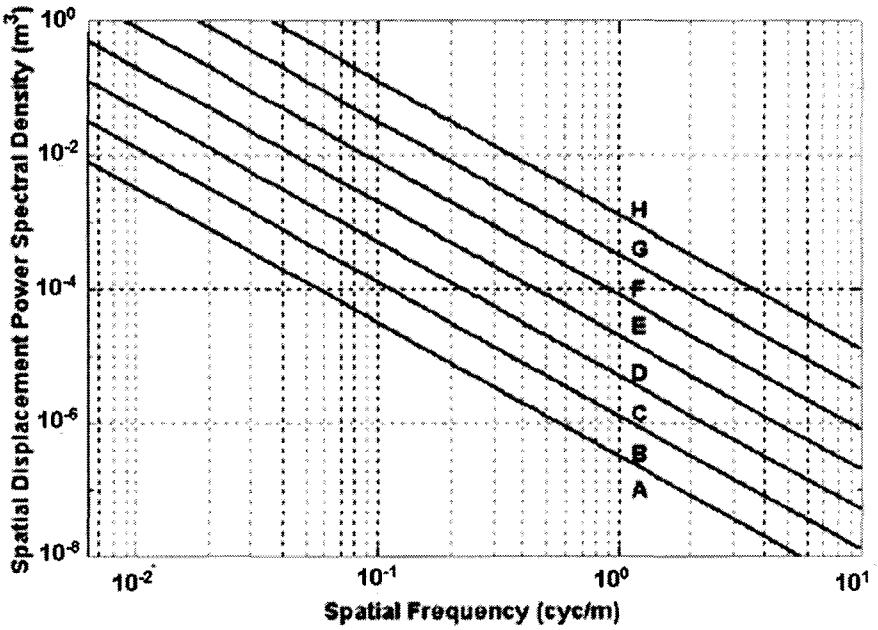

Figure 2.5 Different types of road profile proposed by ISO [10]

2.4 Vehicle Suspension Models

Researchers have commonly used three different vehicle models to analyse ride comfort, rolling, and handling problems. These models are: the full car model, the half car model, and the quarter car model. Schematic diagrams of these models are shown respectively in Figure 2.6a, 2.6b and 2.6c.

All models have two separate masses, an unsprung mass and a sprung mass. The unsprung mass includes wheels, axles, gear drives and other components which are mounted directly on the axle of the vehicle. The sprung mass includes the car body and all other parts of the vehicle supported by suspensions, and also includes the passengers and the payload. The sprung mass of a full car model (Figure 2.6.a) has 3 degrees of freedom (heave, pitch angle, and roll angle). Considering one degree of freedom for each wheel, then a full car model has 7 degrees of freedom. The sprung mass of a half car model (Figure 2.6.b) has 2 degrees of freedom (pitch angle and heave), considering one degree of freedom for each axle, a half car model has 4 degrees of freedom. The quarter car model (Figure 2.6.c) has 2 degrees of freedom, one for unsprung mass and the other for the sprung mass.

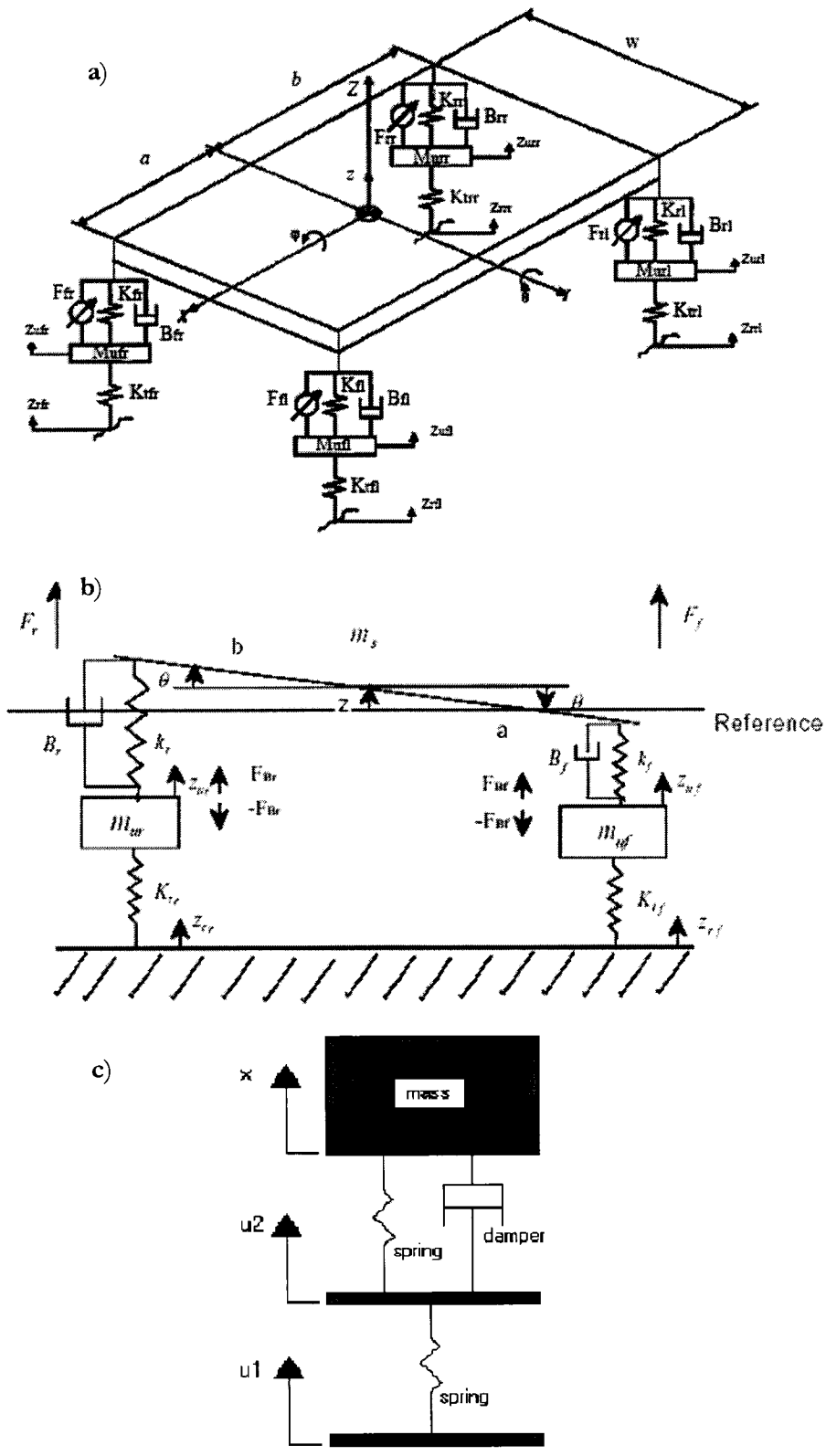

Figure 2.6: Vehicle models a) full car model,
b) half car model, c) quarter car model

Genta [7] obtained the equation of motion of a vehicle on an elastic suspension using the Lagrange equation. He showed how a full car model can be reduced to a half car model or a quarter car model and still be useful for studying the ride comfort. The vehicle on elastic suspension has been modeled as a lumped parameter system with a rigid body. The sprung mass is connected to the unsprung masses through massless springs and dampers. In turn, these unsprung masses are connected to the ground through massless springs and dampers simulating the tires. (6+2n) equations of motions has been obtained where n is the number of axles.

Genta [7] showed that if the speed of the vehicle is a known function of time, the equations form two completely uncoupled sets of (3+n) equations each. The first set deals with the lateral behavior of the vehicle and contains the lateral displacement, yaw and roll angles of the sprung mass, and the roll angle of each axle. The second set deals with the "suspension motion" of the vehicle (ride behavior) and contains the pitch angle, the longitudinal and the vertical displacement of the sprung mass and the vertical displacement of each unsprung mass. The latter set can be further uncoupled by separating the longitudinal dynamics and ride comfort equations. This can, however, be done subject to the following assumptions: a) Existence of a symmetry plane, b) perfect linearity of the behavior of the springs and shock absorbers c) the angles must be small enough to allow the linearization of their trigonometrical functions. Even if nonlinear functions of tire angles appear in the equations of motion, the equations of handling and ride comfort would remain uncoupled [7]. If the aerodynamic term which causes the lack of symmetry of the stiffness matrix is neglected, due to its small magnitude, only a small error is introduced [7]. The vehicle in this case can be modeled as a beam with elastic and damped supports which are connected to the ground through the unsprung masses. In fact under some assumptions the full car model can be reduced to half car model to study the ride comfort of the vehicle. Moreover, Genta [7] explained under which circumstances the half car model can be reduced to a quarter car model. He has defined the dynamic index as follows:

$$I_d = \frac{r_y^2}{ab} \qquad 2.2$$

where r_y is the radius of gyration of the sprung mass, and a and b are the distance between front and rear axle to car body centre of mass respectively. If I_d=1 the

suspension motions of the front and the rear parts of the vehicle are uncoupled and the vehicle can be modeled as two separate quarter car models with two degrees of freedom each. In a real vehicle this condition may never be met. This model is known as the quarter car model (Figure 2.6.c) and is widely used to study the dynamic behavior of the car suspension. Some research has been done on validating these models, the most significant was done by Smith and Sigmen [11] which is reported next.

Smith and Sigman (1981) [11] have modeled a 1979 Ford Fairmont as a modified half car model with two additional degrees of freedom for the driver and the vehicle engine dynamics. The modeled vehicle was traversing Ford's Dearborn Proving Ground at a speed of 55 mph. They have compared the predicted acceleration of the sprung mass and the unsprung masses with the measured corresponding acceleration. Figure 2.7, from Hrovat (1997) [5], shows Smith and Sigman's main result. There is an agreement between the predicted and measured acceleration up to 12 HZ. In fact, there is an agreement between predicted and measured results as long as the car is not affected by high frequency unmodeled modes such as flexible modes, tire unbalance, and various nonlinearities.

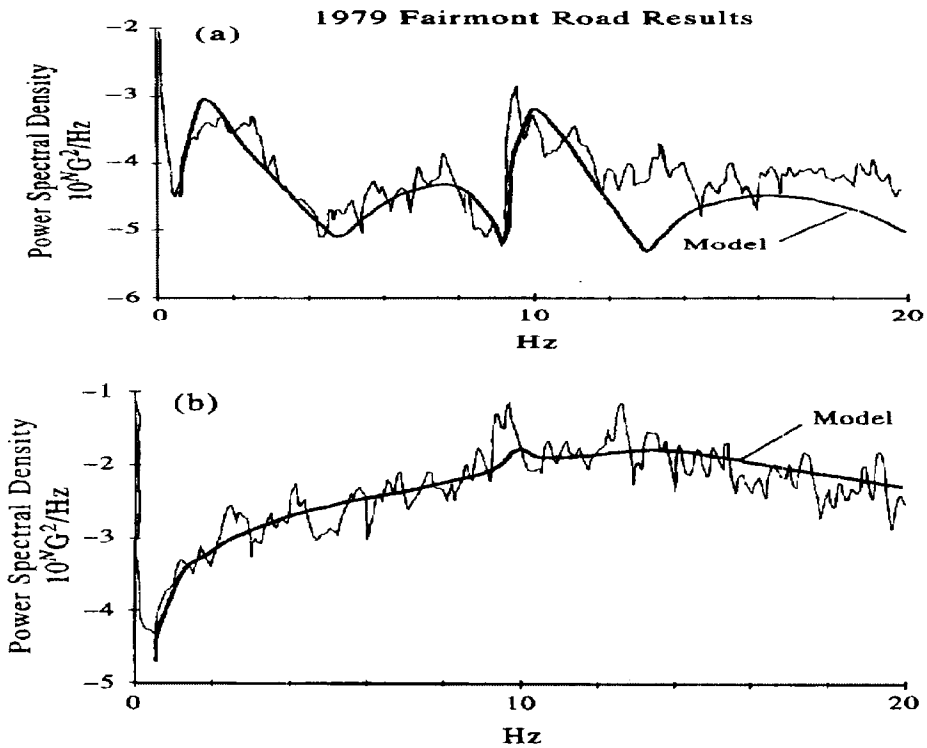

Figure 2.7 Comparison between measured and predicted acceleration Power Spectral Density a) sprung mass b) unsprung mass [5]

2.5 Suspension Types

Three different types of suspensions have been developed: passive suspension, semi active suspension, and active suspension (Figure 2.8). Passive suspension, known as conventional suspension, consists of a spring which is a resilient member and an energy dissipater such as a damper (Figure 2.8.a) to absorb the vibration energy.

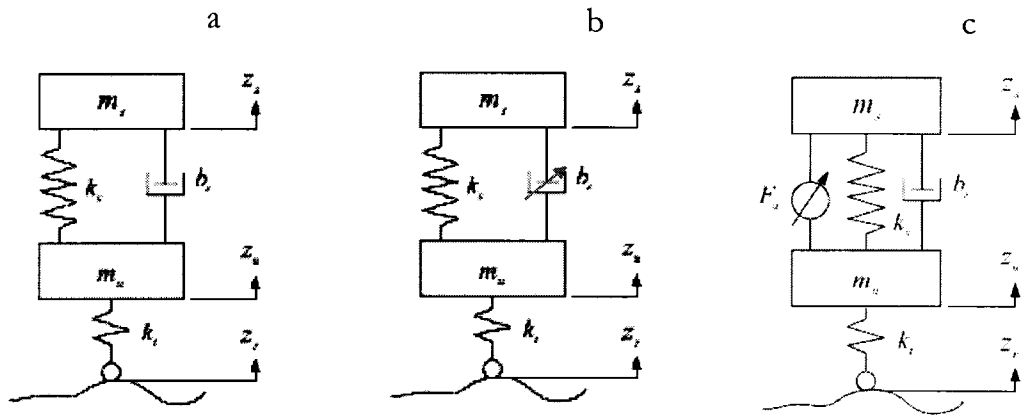

Figure 2.8: Different types of suspensions: a) passive, b) semi-active, c) active

The parameters of a passive suspension are constant in different situations and no external source of energy is used. Different types of springs and dampers have been implemented in the vehicle industry, such as coiled, leaf and air springs; and hydraulic, pneumatic, hydro-pneumatic, and magnetic dampers. Even though passive suspensions have been used for years and are still in use, they have a major drawback. Research on the behavior of passive suspensions has shown that optimal suspension configurations for ride comfort, handling and load carrying problems conflict with each other. While a soft stiffness is required to achieve a good ride comfort over a wide range of frequencies, good handling capability demands a stiff spring at a frequency close to the natural frequency of the unsprung mass and its suspension. Moreover, a high damping ratio is required to reduce the amplitude of vibration around the natural frequency of sprung mass and its suspension, while good vibration isolation for the sprung mass at high frequencies demands a low damping ratio. These conflicts can be solved just by

controlling the stiffness and damping ratio of the suspension. This fact spawned research on active suspensions (Figure 2.8.c).

Unlike passive suspensions, an external energy source is required for active suspensions. The spring and damper in the conventional suspension system are replaced by a force actuator such as an electro-hydraulic or an electro- pneumatic system.

Different control techniques have been implemented to improve the ride comfort and handling of vehicles, such as adaptive control, fuzzy logic control, neural networks and nonlinear control. Since active suspensions need an external source of energy, they are complex and expensive. An intermediary suspension system between the two extremes is the semi-active suspension (Figure 2.8.b). It remedies to some extent the drawbacks of passive suspensions but is considerably less costly and complex than active suspensions. In semi-active suspensions, the spring/damper magnitudes and ratios can be set at will by the operator, or a controller depending on the payload and terrain. In other words, the dissipation energy level is controlled to modify both handling and ride comfort. Some important research works on passive, active and semi-active suspension are reviewed in the following sections.

2.5.1 Passive suspension

Conventional suspensions contain passive components such as coils, leaf springs, torsion bars, and viscous dampers. These components are the primary elements that have been used in passive suspensions. Later, springs with rubber, fluids such as liquids and gases or combinations of them have been used to improve the suspension performance. Even though passive suspensions are not ideal, their simplicity, reliability, and cost make them competitive with advanced and controlled suspensions [9]. Research on passive suspensions can be categorized in three areas: design, optimization and modeling.

Empirical criteria to choose the parameters of suspensions were introduced by Maurice Olley in 1930s. These criteria have been expressed in [7] as follows:

- The vertical stiffness of the front suspension must be about 30 % lower than that of the rear suspension.
- The bounce frequency should be less than 1.2 times of the pitch frequency.
- Neither frequency should be greater than 1.3 Hz.
- The roll frequency should be approximately equal to the bounce and pitch frequency.

The first criterion can be explained by the time lag between the excitation of the rear and front suspensions. The time lag introduces a pitch motion to the vehicle dynamics. If the rear suspension is stiffer, the reaction of the rear suspension will be faster. The faster the rear suspension reaction is, the smaller the time lag is, and consequently the smaller the pitch motion becomes. According to Ginta [7] the second criterion is fulfilled by modern cars. The relationship between pitch and bounce natural frequencies can be expressed as follows:

$$\omega_{np} = \sqrt{\frac{1}{I_d}}\omega_{nb} \qquad 2.3$$

where ω_{np} denotes the pitch natural frequency and ω_{nb} denotes the bounce natural frequency. In order to have a good ride property, the dynamics index defined by Equation 2.2 should be close to unity. The dynamic index of sport cars is around 0.8, and that of conventional passenger cars is between 0.9-1.0. The dynamic index of some front-wheel-drive cars is ≥ 1.2 [10].

Sharp and Crolla in 1987 did a literature review on vehicle suspension system design [12]. Some design consideration were suggested to choose the suspension components such as unsprung masses and tires based on the sprung mass and the load applied on each tire. The first design considerations suggests that the ratio of the sprung mass to the unsprung mass should be around 5 for small cars and 8 for large cars. The second one which is based on empirical results suggests that the ratio of the stiffness of the tires to the weight supported by them should be 40 to 50 (m^{-1}).

The conflict between ride comfort, handling and load variation control is the topic of many studies. Research on the quarter car model has shown that there is a conflict between ride comfort and work space [13, 14]. The ride comfort requires soft springs

and dampers, but a softer spring requires a larger work space. The main discomfort problem arises around the natural frequency of sprung mass and its suspension, where the spring forces are more dominant than damper forces. Around the natural frequency of the unsprung mass system, the damper forces are more dominant than spring forces [15].

For a given stiffness, the optimal damping for ride comfort is less than optimal for tire load variation [15]. This difference worsens by decreasing the stiffness. In conventional suspensions, the optimal damping to maximize ride comfort is less than half of the optimal one to minimize tire load variations. If the damping is designed based on maximum ride comfort, a sacrifice of 21% in the rms of tire load variations will occur. If the damper is designed based on minimizing the tire load variation control, 19% of ride comfort will be sacrificed [16].

Reducing the stiffness for good ride comfort and decreasing damping to use this efficiently makes controlling of tire load variation very difficult. Therefore, reducing the stiffness and damping ratio is useful when enough suspension working space is available and at the same time handling is not important. This may happen when a vehicle with reasonable suspension working space is traveling on a straight and smooth road.

The combination of spring stiffness and damping coefficient that results in the best ride comfort are close to those required for the best control of wheel load when the working space of two cases are the same [16, 17]. If this combination is used in a vehicle suspension with normal working space, it causes the following results: a) the spring stiffness is not sufficient to minimize the static load variation b) the system cannot have sufficient handling stability, and c) the system cannot control the roll angle sufficiently in cornering. If a combination of stiffness and damping ratio is to be used for a vehicle navigating a straight road and no variation in static load is anticipated, this combination should be chosen based on the roughest possible condition [12].

An adequate stiffness is required for a conventional suspension to have reasonable handling performance, and for a given stiffness, a compromise should be made between optimal damping for ride comfort and the ideal one for rough roads [12]. Stiffer springs

are required on rougher roads to decrease the oscillation amplitude. Therefore, it is useful if the stiffness of a suspension system increases as the road becomes rougher. This idea leads to the use of "bump and rebound buffers". As the excitation amplitude increases, the contact between buffer elements increases, and consequently the suspension becomes stiffer. This nonlinearity improves the suspension performance. The nonlinearity between force and velocity in a damper improves the suspension performance as well [12].

Segal and Lang [18] have shown that the force-velocity curve of a hydraulic damper is not symmetric and exhibits hysteresis characteristics. Thompson [15] has studied this asymmetry using a quarter car model exposed to positive and negative excitations. For small excitations, the optimal damping is symmetrical as long as there is contact between the tire and the ground. The asymmetry is related to the size of the excitation. Even though larger damping improves the response for a positive excitation, it has a negative effect when the system is exposed to a negative excitation. Therefore, asymmetry is advantageous for the suspension when the excitation is large and when the contact between the tire and the ground is lost.

In [19] it has been shown that high damping friction on smooth roads reduces ride comfort, and is suggested that for a medium size car the friction force should not be greater than 40 N.

2.5.2 Active Suspension

Since passive suspensions have fixed parameters, these parameters have to be chosen based on a compromise between handling, load carrying and ride comfort. Many attempts have been made to solve this problem by developing a variable parameter suspension. Active suspensions are the first type of variable parameter suspensions used to cope with this problem. As Figure 2.8.c shows, the spring and damper of conventional suspensions are replaced by a force actuator which can be hydraulic, electro-mechanic, pneumatic or magnetic. Active suspensions also contain sensors such as an accelerometer, potentiometer, force transducer, a controller which produces control commands and an external source of energy. Therefore, an active suspension is

able to store, dissipate or introduce energy to the suspension and change the suspension parameters such as stiffness and damping ratio based on different operation conditions.

Thompson [20] showed that an active suspension improves considerably the suspension performance. Sharp and Hassan [17] have used a quarter car model to compare the performance of active and passive suspensions with the same available work space. The sprung mass was 5 times heavier than the unsprung mass and the ratio of the tire stiffness to the applied load was considered to be 40.8 m^{-1}. In the case of unlimited workspace or a smooth road, the performance of the passive suspension is almost the same as the active one when the passive suspension is optimized for this special condition. The most important advantage of active suspensions is their ability to optimize the suspension performance under different conditions. Even though the performances of active suspensions and passive suspensions are the same on the smooth road, as the roughness increases, the active suspensions show considerable improvement in ride comfort and handling control. Active suspensions improve ride comfort by 15% and handling by 10%.

Karnopp [21] brought up the following question: "is increasing the suspension performance worth increasing the cost and the complexity of the system by implementing active suspensions?" For an active suspension it is not possible to achieve any desired performance. While full state feedback control makes it possible to move the eigenvalues of a suspension system to any arbitrary location in the state space and achieve any desired transfer function denominator, Karnopp [21] proved that it is not possible to achieve any desired numerator. He used a quarter car model to prove this. It was also shown that depending upon the vehicle parameters, the idealized fully active suspension only slightly improves the performance of the system, compared to the passive or semi-active suspension. But he emphasizes that it does not mean active suspensions are not beneficiary, because the results are based on a simple form of active suspensions.

In 1979, Karnopp [22] published an article entitled "Are active suspension really necessary?" Two different configurations of a quarter car model were implemented, one with one degree of freedom, and the other with two-degree of freedom. The latter has the same components as the former, except that the wheel is simulated by a spring.

The objective was to keep the relative deflection between the sprung mass displacement and the road profile small and to decrease the maximum acceleration due to the actuator force. The optimal actuator force for the one DOF system was calculated. It was shown that even though this optimal force can be produced actively, it cannot be produced passively. The reason is that the road profile derivative appears in an element of the optimal force. Therefore, it can just be achieved partially using a passive suspension.

In the case of the quarter car model with two-degrees of freedom, it was shown that no damping force can effectively control the resonance of the system. This means the performance of the passive suspension was not sufficiently satisfactory while the active suspension, using partial state feedback control, results in a reasonable performance. Finally it was concluded that replacing passive suspensions by active ones results in a more significant improvement on complex systems than simple ones. When the system is complicated, the performance of the best passive suspension is still poor.

In 1995, Karnopp [23] reviewed historically the development of active suspensions. It was reported that the first active suspension was built by Federspiel-Labrosse in 1954 and was tested on Citroen 2CV. A hydraulic actuator was used and the valves were controlled by a pendulum. The next attempt for using active suspension was made by Obson and Allen in 1965, they used inertia effects to measure acceleration and control the valves of a hydraulic actuator.

Implementing the active suspension using electronic controllers started in the 1980s. Toyota implemented an active suspension using electronic parts for its Soerer in 1983. Group Lotus Car Companies patented and implemented an active suspension in 1984. This suspension had a high bandwidth and was used for racing cars. Active suspensions were commercially available on Toyota and Nissan by the 1990s. While they had considerable advantage over passive suspension, they increased the weight of the vehicle and were expensive. Research on active suspension continued to reduce their complexity and cost [23].

As new techniques such as optimal, adaptive, fuzzy, neural networks and sliding mode controls were developed in control theory, they were implemented on vehicle

suspensions, but always the complexity and the cost remained an issue. In 1997, Hrovat reviewed the research on optimal active suspensions [5].

2.5.3 Semi-Active Suspension

Due to the complexity, cost, reliability, and robustness of active suspensions, semi-active suspensions were developed as a compromise. Their performance lies somewhere in between that of passive and active suspensions but they are reliable, simple and less costly than active ones. The hardware and control configuration of semi-active and active suspensions are similar, but the force actuator in the active suspension is replaced by an adjustable damper in parallel to a spring in the semi-active one. Unlike active suspensions no external energy is introduced into the system. The system is just able to store and dissipate the energy.

In 1974, Karnopp et al [24] used a 1 DOF quarter car model to show that semi-active suspensions can achieve almost the same performance as active suspensions.

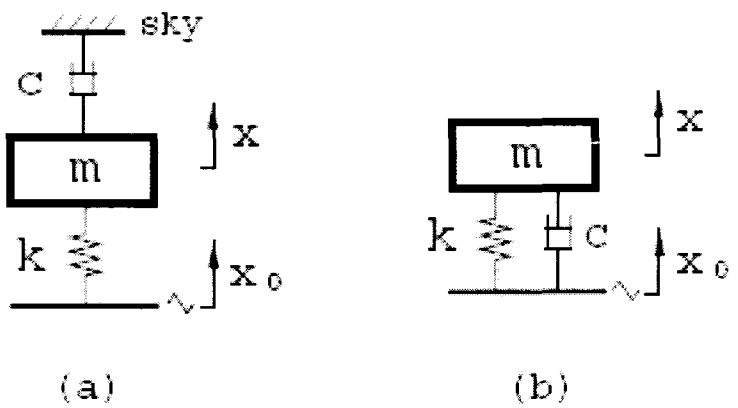

Figure 2.9: a) Skyhook 1 DOF quarter car model b) passive 1DOF quarter car model

The system shown in Figure 2.9.a was used. The performance index PI was defined as:

$$PI = c_1 E(\dot{x}^2) + c_2 E(x - x_0) \qquad 2.4$$

where c_1 and c_2 are constants and E denotes expected value. The optimized actuator force F_c to minimize PI is obtained as follows:

$$F_c = c\dot{x} + k(x - x_0) \tag{2.5}$$

where c and k are the damping coefficient and spring stiffness respectively. In order to produce F_c passively, a configuration similar to Figure 2.9.a is required, but this is not a practical configuration. Therefore, the configuration shown in 2.9.b can be implemented instead. Even though producing F_c passively is not practical, it can be produced actively. The frequency response of skyhook, Figure 2.9.a, and passive suspension, Figure 2.9.b, were compared [24]. The active suspension improves the response around the natural frequency and at the frequencies higher than it. The passive suspension improves the response around the natural frequency but makes the response worse at higher frequencies.

The second factor in Equation 2.5 can be produced using a passive suspension, but the first factor ($c\dot{x}$) cannot be produced passively. To produce this element, an active actuator has to be implemented. This idea led Karnopp et al [24] to implement a semi-active suspension. They replaced the conventional damper by a controllable damper. The controller sometimes demands external energy, but the damper can just dissipate the energy. The easiest way is to set the damper force to zero whenever the system needs energy generation. The following conditions are considered:

$$\begin{aligned}
&if \quad \dot{x}(\dot{x} - \dot{x}_0) > 0 \Rightarrow F_d = c\dot{x} \\
&if \quad \dot{x}(\dot{x} - \dot{x}_0) < 0 \Rightarrow F_d = 0 \\
&if \quad \dot{x}(\dot{x} - \dot{x}_0) = 0 \Rightarrow \begin{cases} if \quad \dot{x} = 0 \Rightarrow F_d = 0 \\ if \quad \dot{x} \neq 0 \Rightarrow F_d = c\dot{x} \end{cases}
\end{aligned} \tag{2.6}$$

This makes the performance of semi-active and active suspensions different. The frequency responses of active, semi-active and passive suspensions were compared. It was shown that the performance of semi-active is somewhere between passive and active suspensions. At high frequencies, its performance is very close to the active suspension (skyhook), but close to the natural frequency, it is not as good as the active suspension. They proposed an electro-hydraulic actuator performing as a semi-active force actuator with a small power supply. Even though the concept of the semi-active was shown using a very elementary system, it can be implemented on more complex systems. Similar results were obtained by using a 2 DOF quarter car model [24].

Karnopp in 1995 [23] reviewed historically the works on semi-active suspension. The basic idea of semi-active suspension, as was discussed before, was introduced by Karnopp and Crosby in the 1970's. It took almost one decade to build a shock absorber based on this principal and test it on an American car in Germany. Later on, different types of semi-active suspension were built and implemented. Semi-active suspension was available commercially since the early 1990s [23].

Research on semi-active suspensions is focused on the modeling of different types of damper, and building and implementing better adjustable dampers such as magnetorheological (MR) dampers and pneumatic suspensions. Since this research is focused on pneumatic suspensions, some of the literature dealing with this topic is reviewed in the following section.

2.6 Pneumatic Vibration Isolator

In 1884, a patent was issued to Charles Lewis entitled;" Pneumatic Springs for railroad Cars, Locomotives, Burden-Cars, Bumpers." It took almost a century before the rubber manufacturing industries could produce a reliable air spring.

In 1961, Cavanaugh [25] studied a double sided damping air spring. He had shown the transmissibility properties of pneumatic isolators for the first time. For many years, research on the vibration isolator was focused on improving the transmissibility at high frequencies. Figure 2.10 illustrates the transmissibility of a conventional suspension. The high damping ratio curves have low transmissibility around the natural frequency, but at high frequencies, their transmissibility is considerably higher than low damping ratio curves.

The first trials (Waller and Benham 1963 [26]) were focused on using two springs and switching between them depending on the frequency range. The high stiffness spring is used for low frequencies; and in the high frequency region a low stiffness spring is used as shown in Figure 2.11. The drawback of the system is the discontinuities resulting from switching.

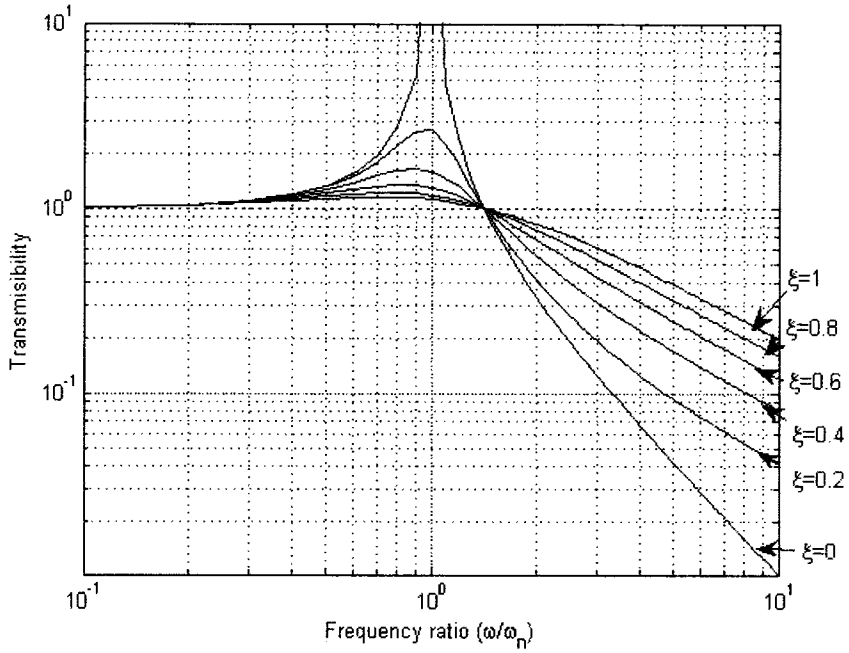

Figure 2.10 Transmissibility of conventional suspension

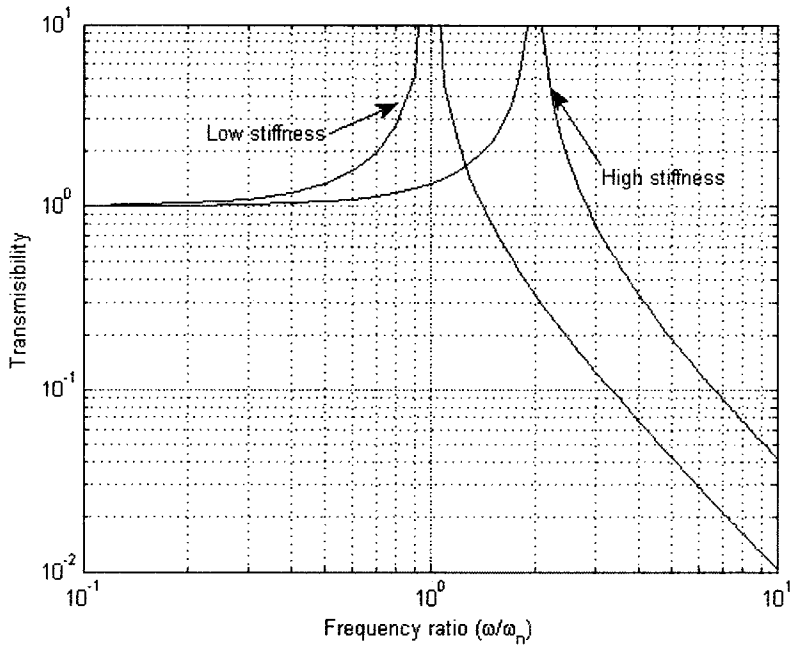

Figure 2.11 Transmissibility of "dual frequency" isolator with no damping

In 1966, Soleiman and Tajer-Ardabili [27] overcame this problem by using a surge tank connected to an air spring through a capillary resistance. At low frequencies, the transmissibility of the capillary is high, causing the pressure change in the air spring to

affect the tank. Therefore, the volume of the isolator is the sum of that of the air spring and the surge tank. At high frequencies, the transmissibility of the capillary is low such that pressure change in the air spring does not affect the surge tank the isolator volume is equal to that of the air spring alone. Since the capillary introduces damping to the system, the damping is high at low frequencies and very low at high frequencies, therefore the performance of the isolator improves considerably. The transmissibility Tr of the system is given by:

$$Tr = \left\{ \frac{1+(2\xi\omega/\omega_n)^2}{(1-\omega^2/\omega_n{}^2)^2+(2\xi\omega/\omega_n(1-\frac{\omega^2}{(1+V_0)\omega_n}))^2} \right\} \qquad 2\text{-}7$$

where V_0, ξ and ω_n are the ratio of surge tank volume to air spring volume, the damping ratio and the natural frequency of the system. The transmissibility of this system for $V_0 = 3$ is plotted in Figure 2.12.

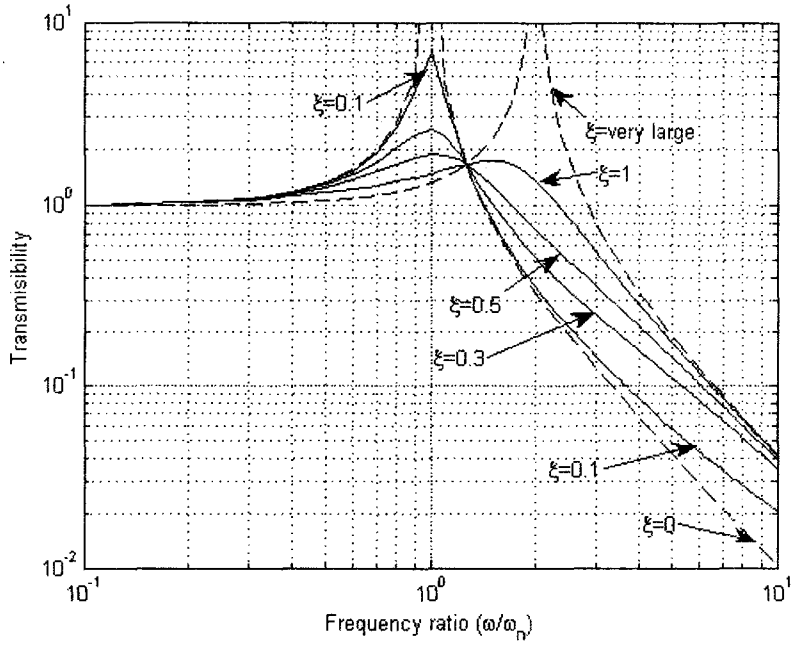

Figure 2.12 Transmissibility of self-damped pneumatic isolator

The drawback of this configuration is that the switching stiffness is in the wrong way. Since the stiffness is inversely proportional to the volume, at low frequencies, where the volume is large, the stiffness is small, and at high frequency, where the volume is small, the stiffness is large. But large stiffness is required at low frequencies and small stiffness is required at high frequencies.

This problem motivated Gee-Clough and Waller in 1968 [28] to use an inertia block supported by an auxiliary pneumatic cylinder. The auxiliary pneumatic cylinder is connected to the main cylinder through a capillary tube (Figure 2.13). The weight of the inertia block is supported by the auxiliary pneumatic cylinder and the weight of the main body is supported by two pneumatic isolators in series. At low frequencies, the pressure change in the auxiliary isolator is transmitted to the main isolator through the capillary tube. Therefore, any applied force on the inertia block produces an opposite force from the main pneumatic isolator. In other words, the two isolators are working in series and the whole system behaves as a system with one degree of freedom. At high frequencies, the pressure change cannot be transmitted to the main isolator; therefore, the whole system behaves as a two degree of freedom suspension.

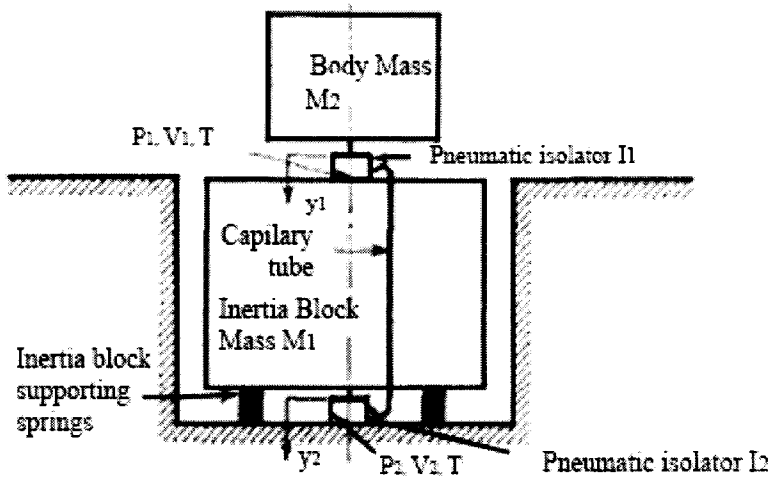

Figure 2.13: Pneumatic suspension with inertia block [28]

The optimum ratio between the masses of the body and inertia block is 0.1 and the optimum ratio between the volumes of two pneumatic isolators is 1.0. The transmissibility curves for these two ratios are reproduced in Figure 2.14 using the formula presented in [28]. The figure illustrates a considerable improvement in the performance of the pneumatic isolator compared to the conventional suspension. The curve corresponding to $\xi = 0.6$ is the most interesting one when it is compared to the conventional spring damper isolator system with $\xi = 0.3$. The transmissibility around the natural frequency is almost the same, but at high frequencies it is 35 times lower than conventional suspension.

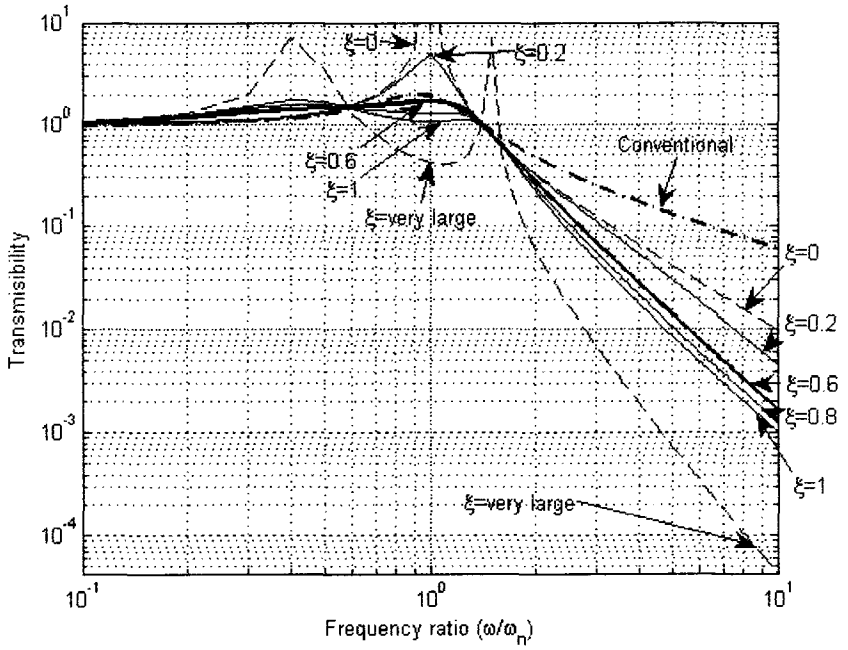

Figure 2.14: Transmissibility curves for pneumatic suspension with inertia block

This setup cannot be easily implemented in vehicle suspension, because adding an inertia block is not practical, but it can be used in machinery and structural vibration isolator. Esmailzadeh in 1980 [29] showed that Gee-Clough and Waller's [28] configuration can be implemented in vehicle suspension as well. He also validated the model experimentally.

Hundal in 1982 [30] used a pneumatic isolator in parallel to a linear spring (Figure 2.15) to analyze the behaviour of pneumatic isolators and introduces a design method using dimensional analysis.

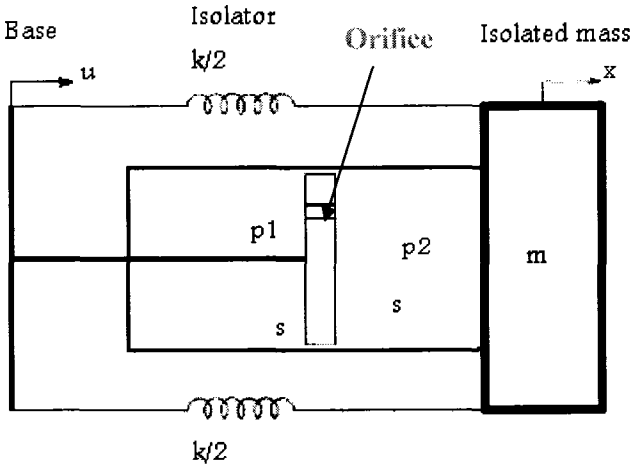

Figure 2.15: Pneumatic isolator in parallel with linear springs

Assuming an adiabatic process, the equations explaining the mass derivative on both sides of the piston were obtained. The mass flow through the orifice was also calculated. The maximum acceleration versus the ratio of the orifice area to piston area was plotted for different dimensionless mass and stiffness. It was shown that the minimum value of the acceleration $\ddot{x}_{min}$ occurs when the dimensionless stiffness k is minimum. Obtained curves for different dimensionless stiffness are shown in Figure 2.16. At the end of the manuscript, a method for designing of this special isolator was recommended.

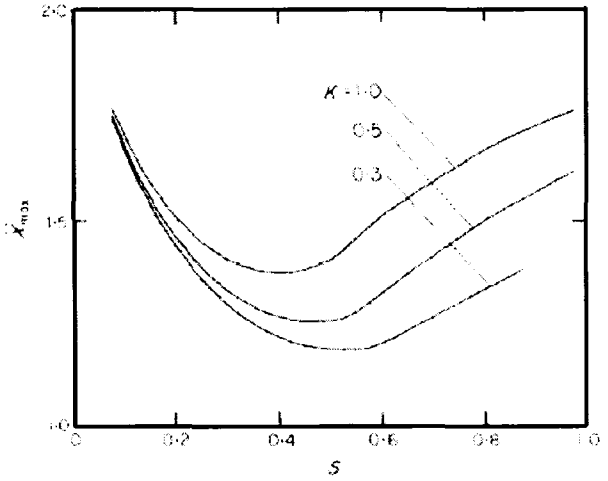

Figure 2.16: Maximum mass acceleration versus dimensionless area

B.I.Bachrach and E.Rivin [31] in 1982 combined Hundal's [30] and Soleiman and Tajer-Ardabili's [27] works. Their research is composed of two parts. In the first, they used a pneumatic spring connected to the surge tank through capillary (Figure 2.17) to analyze the effects of different parameters on the pneumatic stiffness and damping.

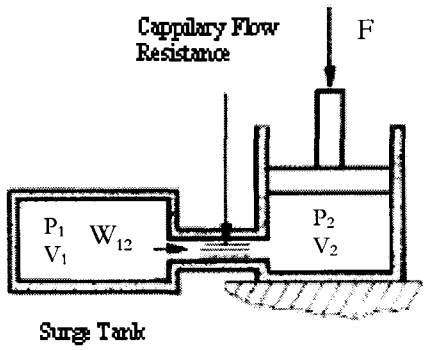

Figure 2.17: Bacherach and Revin's self damped pneumatic spring [31]

The equation of the pneumatic stiffness was obtained by writing the weight flow equations for the surge tank, capillary and pneumatic spring. The obtained stiffness is half of the result obtained by Cavanaugh [25] for a double sided air spring. The sinusoidal pneumatic stiffness was expressed in terms of the volume ratio, frequency ratio and capillary coefficient. The equation of complex stiffness was written in term of the loss factor and the real stiffness. The frequency corresponding to the maximum loss factor was obtained. It was shown that the maximum loss factor is a function of volume ratio only, but the frequency corresponding to this maximum value is also a function of capillary coefficient. Therefore, the capillary dimensions only affect the frequency at which maximum damping occurs. It does not affect the maximum damping value. In other words, the maximum damping value is related only to the volume ratio.

The second part of the research is focused on a damped pneumatic spring in parallel to a linear spring

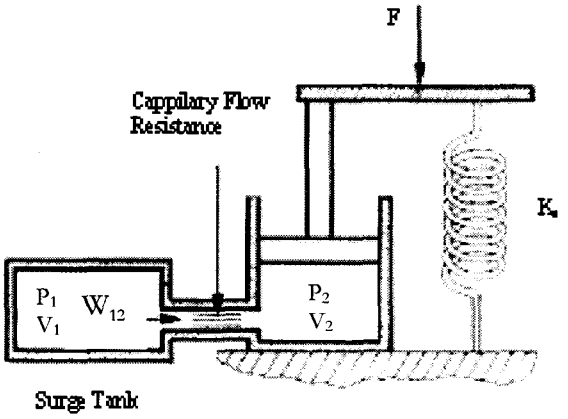

Figure 2.18: Damped pneumatic spring on parallel to linear spring

Figure 2.18 shows the setup used in this part. If the stiffness of the linear spring is much greater than the stiffness of the air spring alone, the behaviour of the compound pneumatic spring shown in Figure 2.18 is completely different from the one shown in Figure 2.17. In this case, the frequency at which the maximum loss factor occurs is not related to the volume ratio, especially when volume ratio is bigger than 2. B.I.Bachrach and E.Rivin [31] concluded that when the damped pneumatic spring is used in parallel

2.7 Modeling of Air Springs

Toyofuku et al in 1999 [32] introduced a new approach to optimize air spring characteristics. This analysis was already employed successfully on a heavy duty bus in 1997. The employed air suspension system consists of an air spring connected to an auxiliary chamber by a pipe line and an on-off electro-magnetic valve which controls the air spring volume.

The equations of continuity, energy and gas state were obtained for the air spring, auxiliary chamber and pipe line. The boundary condition was also considered at the connection point of the pipe to the air spring and the auxiliary chamber.

A pneumatic cylinder with a constant effective area (1.1×10^{-3} m^2) was used as an air spring to study the effect of the pipe. The cylinder rod was connected to a vibration exciter, producing sinusoidal vibration with different frequencies. Pressure was measured in seven different positions along the pipe space at 1.5m intervals, starting from the pneumatic cylinder and ending at the auxiliary chamber. The air spring displacement was also measured by a potentiometer on the vibrator. The pneumatic cylinder reaction force was calculated by multiplying the air spring pressure and the cylinder cross section. Bode diagrams were plotted for the ratio of the force change to the displacement change for two different pneumatic cylinder amplitudes (1mm and 5mm). The same experiment was performed without an auxiliary chamber. The simulated frequency responses were obtained with and without an auxiliary chamber and were superimposed. It was shown that the experimental result agrees with the simulated result, when there is no auxiliary chamber. At low frequencies, the experimental result agrees with the simulated result for a pneumatic cylinder with auxiliary chamber. At high frequencies the experimental result agrees with the result obtained without the auxiliary chamber. The experimental Bode diagram has a minimum at 5 Hz and a maximum at 11 Hz. In order to investigate the reason behind this phenomenon, the pipe was substituted by an orifice with the same resistance as the pipe, but the result was completely different. This shows that the friction of the pipe does not cause this phenomenon.

The pressure along the pipe, measured by pressure transducers, was plotted for 4 different frequencies (1, 5, 11, 20 Hz). At 1 Hz, the pressure of the air spring and the chamber are in phase. At 5 Hz, low pressure at the air spring and the high pressure at the auxiliary chamber imply that the pipe resonates with the auxiliary chamber. At 11 Hz both air cylinder and chamber pressure amplitudes are large showing that the whole system resonates. The constant pressure of the auxiliary chamber, at 20 Hz, shows that the pressure is not transmitted at high frequencies. Using the developed mathematical model, the entire system including the pipe line was simulated and the results were compared with the experimental ones. The simulation results agree well with the experimental results.

Quaglia and Sorli in 2000 [33] performed some experiments to characterise the air spring parameters. It was shown that the pressure has a small influence on the air spring effective area. The air spring volume was measured for different assembly heights. It was also shown that the air spring volume is very much independent of the air spring pressure. Some experiments were performed with constant air mass. While the air mass inside the air spring was kept constant, the air spring pressure and the applied force were measured as the air spring height varies. The pressure-height and force-height curve shows a hysteresis between the expansion and compression processes. The overall stiffness of the spring was formulated as a summation of two factors which are related to the volume derivative and the effective area derivative. These two factors were plotted vs. height for different initial pressures and two different processes: isothermal and adiabatic. The stiffness was also calculated by obtaining the slope of the experimental force curve. The experimental stiffness was compared with the simulated one in a single graph. The experimental stiffness lies between the adiabatic and isothermal curves.

A set of experiments was also performed to analyse the transmission of the exerted force by the air spring and the transmission of vibrations to the sprung mass. These experiments were repeated for different orifice diameters. The effects of resistance, initial pressure and imposed displacement were investigated. The ratio of the force to the height and the phase shift between them were plotted vs. different frequencies. It was shown that the transmissibility at low frequencies and high frequencies are independent of the valve resistance. At low frequencies, the air spring and reservoir

behave as a single volume without any resistance in between. At high frequency, air cannot flow through the orifice and the system behaves as an air spring with constant air mass without the reservoir. The stiffness and natural frequency of the system at low and high frequencies were calculated. The natural frequencies were compared with two peaks which appeared in the frequency response of the system with different resistances. The lowest frequency was the same as the frequency corresponding to zero resistance and the higher one was the same as the frequency corresponding to the high resistance.

Quaglia and Sorli in 2001 [34] presented a dimensionless linear model to simplify the selection of an air spring for different applications. The dimensionless linear model makes it possible to understand the effect of different parameters on suspension properties. The behaviour of the nonlinear mathematical model was used as a criterion to verify the obtained linear model. The nonlinear mathematical model was obtained using an ISO 6358 expression for the flow rate. The volume and effective area were assumed to be a function of the air spring height only and independent from the air spring pressure. The frequency response of the nonlinear model was obtained for different orifice diameters. It was shown that as the orifice resistance changes, all the magnitude curves pass through a common point. The curve whose peak occurs at this point corresponds to the optimum orifice resistance for different combinations of spring and reservoir. The step response of the nonlinear model was obtained for different orifice resistances. It was shown that the step response specifications are related to the excitation amplitude. The smallest resistance is the best for small oscillation and the largest one is the best for the large oscillation. For example, the smallest resistance gives the greatest maximum overshoot and smallest settling time for the large amplitude.

The obtained nonlinear model is linearized around an equilibrium point using Taylor series expansion. The first term of the Taylor series was considered. The transfer function of the sprung mass displacement to the road roughness was derived and found to be of order three. It was shown that when the reservoir is blocked the transfer function of the air spring reduces to order two. This is also true for low frequencies when the system behaves as a spring with a volume equal to summation of the air

spring and reservoir volumes. The frequency response of the linearized mathematical model was validated by comparison to the frequency response of the nonlinear model.

The obtained linearized model was made dimensionless using the frequency ratio factor. The frequency ratio factor is defined as the ratio of the natural frequency of the air spring alone to that of the air spring plus reservoir with zero resistance. The dissipation factor, which appeared in the linearized equations, was introduced. The frequency ratio factor and dissipation factor were written in terms of the air spring physical parameters. The frequency responses of the dimensionless mathematical model were obtained for a frequency ratio factor equal to 2 and different dissipation factors. The coordinates of the optimal point was derived analytically. The dissipation factor corresponding to the optimal point was expressed in terms of the frequency ratio factor. At the end of the paper some suggestions for choosing the parameters of an air spring with a reservoir are given.

2.8 Active Suspension Using Air Spring

Takagami and Jimbo [35] improved the vibration of a payload on a table supported by an air spring. They controlled the pressure in the air spring to minimize the vibration of the payload. The air spring is connected to a reservoir on one side by a throttle valve and is connected to a cylinder piston servo-system on the other side. When the payload moves upward the piston moves to the right to allow the air to flow out of the air spring and reduce the pressure inside it. When the payload moves downward the piston moves toward the air spring to allow air to flow into the air spring and increase the air pressure inside it. The volume of the reservoir is twice the air spring volume. The optimum value of the throttle opening area was calculated and verified experimentally. Two sensors measure the displacement of the payload and the floor. The velocities of the payload and the floor displacements are also calculated. The measured signals are fed to an electrical network which produces a control command to move the piston. In fact, each measured signal is multiplied by a gain and their sum is used to move the piston. The best combination of gains was obtained by trial and error. The designed controller was tested under a random vibration. The power spectra of the payload displacement

without control and with control were compared. The result shows a considerable improvement in the vibration isolation.

Winfred et al [36] in 2002 published the work which was completed gradually by a group of students over about 10 years. They designed and built a prototype quarter car model which consists of two coil springs, a damper, and an air spring. A three-phase alternating current gear motor which drives a cam was used to simulate the road profile. Assuming a constant damping and stiffness for the air spring, the transfer function between the sprung mass and the road profile was obtained. The fourth order transfer function was reduced to a second order transfer function assuming very large stiffness for the wheel. The mathematical model was validated by a step response. A state variable feedback plus integral was designed and was implemented. A microprocessor was used to produce the control command which controls the airflow to the air spring based on the sensor signals.

Xiao and Kulakowski [37] tried to design a robust controller which can handle the payload variation and model nonlinearity in a pneumatic suspension. A half car model with pneumatic suspension was used. The force of each air spring was modeled as a fourth order polynomial function of the air spring deflection. The coefficients of this polynomial are first order polynomial functions of the static loads. The coefficients of these first order polynomials are obtained by performing curve fitting on the experimental data for different loading conditions. The force-deflection curves of the derived model were compared with the experimental force-deflection curves. The two curves for different payloads are very close to each other. Considering two actuators at the front and rear axles, a sliding mode control was designed to track a reference input by changing the actuator forces. The response of the designed sliding mode controller was compared with the passive nonlinear model and the reference model for a fully loaded vehicle and a vehicle without passengers. Comparisons show that the sliding mode controller can follow the reference model. The effect of the control gain on the system response was investigated. As the gain increases, the chattering increases and the ability of the controller to track a reference input in the presence of large uncertainty increase.

Chapter 3

Similitude Model of the Honda Civic (Sedan)

3.1 Introduction

Throughout history, scientists have found that performing experiments is a useful approach not only for verifying their hypothesis, but also for designing and manufacturing. Galileo brought up the essence of performing experiments to prove a hypothesis in his book, "Two New Sciences." He defends his "falling bodies hypothesis" against Aristotelianism with the following sentence: "I greatly doubt that Aristotle ever tested by experiment whether it be true that two stones, one weighing ten times as much as the other, if allowed to fall, at the same instant, from a height of, say, 100 cubits, would so differ in speed that when the heavier had reached the ground, the other would not have fallen more than 10 cubits"[38]. This sentence shows how Galileo valued experiments to prove hypotheses. It is said that he had carried out this special experiment on the top of the Pisa tower.

Experimentation is not only useful for proving a hypothesis but is also useful in analyzing physical phenomena and predicting their behaviour. The necessity of doing experiments even for complex and expensive systems, leads scientists and engineers to the idea of building models. They started to predict the behaviour of physical phenomena by building either a mathematical model or an experimental scaled model. Even though engineers nowadays have a tendency to rely more and more on mathematical models over physical ones, experiments on physical models are unavoidable and more reliable in most cases [39]. For example, with the exception of simple system, building an accurate mathematical system model cannot be performed without experimental validation and system identification. The necessity of using scaled physical model become obvious when dealing with very expensive, very slow, very complicated or unmanageable systems. For example, carrying out experiments on aircraft to study far-field effects of sonic booms is impractical without making a scaled model.

The similitude theory deals with the problem of the design of scaled models to represent the behaviour of full scale real systems. It ensures that the experimental results obtained from the scaled model are a good proxy of those that would be obtained for a full scale model, and are reliable enough to be used for the behavioural study of the design of the real system. The basis of the similitude theory is dimensional analysis. For a scaled model to be a similitude model and maintain the similarity, it should be scaled so that the geometrical, kinematical and dynamical similarities are retained. In 1914, Buckingham introduced the π-theorem which is the basis of dimentional analysis and consequently the similiude theory. Bridgmann used the term "dimentional analysis" for the first time in his book, "Dimentional Analysis" in 1922 [40].

The ultimate goal of the present research work is the application of nonlinear control theory to pneumatic suspension system. Considering the fact that experimental verification of the controller on a real car is very expensive and difficult, building a scaled model of the car seems to be unavoidable. In order to build a scaled model, a suitable type of car should be chosen. Many different types of automobiles have been studied. Two criteria have been considered for choosing the appropriate car: a) the availability of car specifications b) the sufficient suspension stiffness to be replaced by an air spring. Among the different studied automotive types the Honda Civic satisfies these conditions.

In the present chapter, the process of designing the scaled half car model of the Honda Civic based on the similitude theory is explained. The equations of motion for the half car model are obtained, and dimensional and equational analyses are performed on the mathematical model. Dimensionless variables and equations are derived, the criteria for similitude model are explained, and based on these criteria, the scaled half car model of the Honda Civic is designed. All the information about similitude theory and dimensional analysis has been extracted from the references [39], [40] , [41] and [42].

3.2 Mathematical Model of a Half Car Model

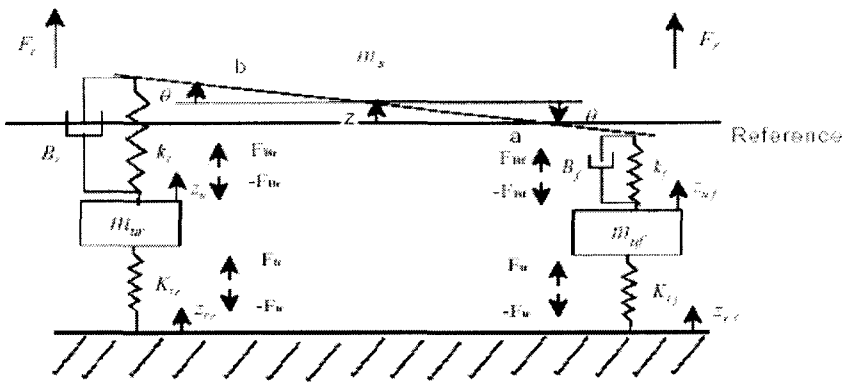

Figure 3.1 A typical half car model

Figure 3.1 shows a typical half car model. As was discussed in Section 2.4, the half car model contains a sprung mass (representing the car body, passengers and the payload) connected to two unsprung masses (representing the axles and the other parts which are mounted on the axles such as the engine and the gearbox) through two massless spring damper suspensions. The details of the half car model and assumptions made to reduce a full car model into a half car model have been explained in Section 2.4. The car body is considered to be a beam with a moment of inertia equal to "J" and a mass equal to m_s. Lengths "a" and "b" are the distances from the centre of mass to the front and the rear axle, respectively. m_{ur}, K_r, B_r and K_{tr} are, respectively, the unsprung mass, the spring stiffness, the damping coefficient and the tire stiffness of the rear axle, and m_{uf}, K_f, B_f and K_{tf} are the parameters of the front axle. Applying Newton's second law to the sprung and unsprung masses, the equations of motion for the half car model are as follows:

$$m_{ur}\ddot{Z}_{ur} = F_{Br} - F_{tr} = B_r\dot{Z}_s - bB_r\dot{\theta} - B_r\dot{Z}_{ur} + K_rZ_s - bK_r\theta - (K_r + K_{tr})Z_{ur} + K_{tr}Z_{rr} + F_r \quad 3.1$$

$$m_{uf}\ddot{Z}_{uf} = F_{Bf} - F_{tf} = B_f\dot{Z}_s + aB_f\dot{\theta} - B_f\dot{Z}_{uf} + K_fZ_s + aK_f\theta - (K_f + K_{tf})Z_{uf} + K_{tf}Z_{rf} + F_f \quad 3.2$$

$$m_s\ddot{Z}_s = F_{dr} + F_{df} - F_{Bf} - F_{Br} = K_rZ_{ur} + B_r\dot{Z}_{ur} + K_fZ_{uf} - (K_r + K_f)Z_s + B_f\dot{Z}_{uf} - (B_r + B_f)\dot{Z}_s + (bK_r - aK_f)\theta + (bB_r - aB_f)\dot{\theta} - (F_f + F_r) \quad 3.3$$

$$J\ddot{\theta} = b\cos(\theta)F_{Br} - a\cos(\theta)F_{Bf} = -bK_r Z_{ur} - bB_r \dot{Z}_{ur} + aK_f Z_{uf} + (bK_r - aK_f)Z_s$$
$$+ aB_f \dot{Z}_{uf} + (bB_r - aB_f)\dot{Z}_s - (b^2 K_r + a^2 K_f)\theta - (b^2 B_r + a^2 B_f)\dot{\theta}$$
$$+ bF_r - aF_f \qquad 3.4$$

where Z_{rf} and Z_{rr} are the road unevenness exciting the front and rear axle; z and θ represent the heave and the pitch angle of the car body, respectively. Equations 3.1 to 3.4 are the half car model equations of motion, and from these equations the parameters explaining the system behavior can be obtained.

3.3 Dimensional Analyses

For proper comprehension of the following dimensional analysis, the terms basic units and primary quantities need to be defined.

Basic units: the smallest group of units from which all other units can be derived.

Primary quantities: the minimum group of quantities, usually the same number as basic units, whose dimensions include all basic units.

Obtaining the scale factors of the basic units is the ultimate goal of the dimensional analysis. These scale factors are then used to obtain all the scale factors of the other parameters. The first step in dimensional analysis is to choose the basic units. The units of length, time, mass or force, temperature and electric current are the five basic units which are frequently used. In fact, all other units can be written in terms of these base units.

The dimensionless numbers, also referred to as "Pi-numbers", play a key role in dimensional analysis. The procedure for finding Pi-numbers consists of two parts: a) establishing the dimensional table for the system quantities b) solving the equations derived from that table to obtain the Pi-numbers. The dimensionless mathematical model can be derived by reshaping the equations of motion of the system using Pi-numbers and dimensionless variables.

3.3.1 Obtaining Pi-Numbers

The chosen basic units for the suspension system are the dimensions of length (L), mass (M) and time (T). The dimensions of other quantities such as pressure and force can be stated as power product of the basic units. The only condition for choosing the primary quantities is that the dimensions of these quantities must contain all the basic units; for example, if the dimension of the first quantity contains time, the dimension of the second quantity should includes length or mass in addition to time, and the third quantity should contain the basic unit which is not included in the two first quantities.

Table 3.1: Dimensional table of the half car model

	$Z_1 = \ln(U_L)$	$Z_2 = \ln(U_M)$	$Z_3 = \ln(U_T)$
$Y_1 = \ln(U_{Z_{cm}})$	1	0	0
$Y_2 = \ln(U_{M_s})$	0	1	0
$Y_3 = \ln(U_{w_0})$	0	0	-1
$Y_4 = \ln(U_{K_r})$	0	1	-2
$Y_5 = \ln(U_{B_r})$	0	1	-1
$Y_6 = \ln(U_{K_{tr}})$	0	1	-2
$Y_7 = \ln(U_{B_f})$	0	1	-1
$Y_8 = \ln(U_{M_u})$	0	1	0
$Y_2 = \ln(U_a)$	1	0	0
$Y_2 = \ln(U_b)$	1	0	0
$Y_2 = \ln(U_l)$	1	0	0
$Y_2 = \ln(U_J)$	2	1	0
$Y_2 = \ln(U_{K_f})$	0	1	-2
$Y_2 = \ln(U_{K_{tf}})$	0	1	-2
$Y_2 = \ln(U_{F_r})$	1	1	-2
$Y_2 = \ln(U_{F_f})$	1	1	-2

The height of the center of mass (Z_{cm}), the sprung mass (M_s) and the front wheel natural frequency (w_0) are chosen as primary quantities for the suspension system. The first column of the dimensional table contains logarithm of the quantity units and the first row contains the basic units. Each cell of the table is identified by the power of the corresponding basic unit in the corresponding quantity dimension. For example if the ith row corresponds to K_f which has a dimension of MT^{-2}, and jth column corresponds to T, the cell corresponding to the ith row and the jth column will have a value of -2. The primary quantities are the first group of quantities whose units are listed in the table, followed by the rest of the quantities. Table 3.1 is the dimensional table of the half car model.

The basic units are assumed to be variables in order to apply the logarithm function to the parameter dimensions. The use of the logarithm function of units approach simplifies and automates the procedure. While it may seem too complicated within the current context or the current moderate complexity problem, it ensures that no errors creep up in the dimensional analysis. This can be exemplified as follows: Assuming p_i as the dimension of the ith parameter, p_i can be stated as the power product of the basic units as follows:

$$p_i = (U_L)^a (U_M)^b (U_T)^c \tag{3.5}$$

Taking the logarithm of Equation 3.5 gives:

$$\ln(p_i) = a\ln(U_L) + b\ln(U_M) + c\ln(U_T) \tag{3.6}$$

Denoting the logarithm of p_i by Y_i and the logarithm of the basic units U_L, U_M, and U_T by Z_1, Z_2, Z_3, respectively, Equation 3.6 becomes:

$$Y_i = aZ_1 + bZ_2 + cZ_3 \tag{3.7}$$

Since a, b, c are the same number which occupy the corresponding cell in the dimensional table, Equation 3.7 can be written for each quantity using the corresponding row of dimensional table.

Using the dimensional table, the dimensionless number can be determined as follows: Applying Equation 3.7 to the primary quantities, the first 3 quantities in Table 3.1, gives:

$$Y_1 = Z_1 \tag{3.8}$$

$$Y_2 = Z_2 \tag{3.9}$$

$$Y_3 = -Z_3 \tag{3.10}$$

The logarithms of all other quantities are then stated in terms of the logarithms of the primary quantities. Applying Equation 3.7 to the fourth quantity, K_r, gives:

$$Y_4 = Z_2 - 2 * Z_3 \tag{3.11}$$

Substituting Z_2 and Z_3 from Equation 3.9 and 3.10 into Equation 3.11gives:

$$Y_4 = Y_2 + 2 * Y_3 \tag{3.12}$$

Substituting for Y_i's by their logarithmic definition and rearranging gives:

$$\ln(U_{K_r}) - \ln(U_{M_s}) - 2\ln(U_{w_0}) = \ln(1) \tag{3.13}$$

Since the dimension of a Pi-number is unity, the unity on the left hand side of Equation 3.13 can be replaced by the dimension of a Pi-number. Rearranging Equation 3.13 results in:

$$\ln\left(U_{\left(\frac{K_r}{M_s w_o{}^2}\right)}\right) = \ln\left(U_{\pi_1}\right) \tag{3.14}$$

where π_1 denotes the first Pi-number.

Taking the antilogarithm of Equation 3.14 gives:

$$\pi_1 = \frac{K_r}{M_s w_o{}^2} \tag{3.15}$$

The other dimensionless numbers are obtained with the same procedure , and are listed bellow:

$$\pi_2 = \frac{Br}{M_s w_o} \tag{3.16}$$

$$\pi_4 = \frac{B_f}{M_s w_o} \quad 3.18$$

$$\pi_5 = \frac{M_u}{M_s} \quad 3.19$$

$$\pi_6 = \frac{a}{Z_{cm}} \quad 3.20$$

$$\pi_7 = \frac{b}{Z_{cm}} \quad 3.21$$

$$\pi_8 = \frac{l}{Z_{cm}} \quad 3.22$$

$$\pi_9 = \frac{J}{Z_{cm}^{\ 2} * M_s} \quad 3.23$$

$$\pi_{10} = \frac{Z_s}{Z_{cm}} \quad 3.24$$

$$\pi_{11} = \frac{Z_{uf}}{Z_{cm}} \quad 3.25$$

$$\pi_{12} = \frac{Z_{ur}}{Z_{cm}} \quad 3.26$$

$$\pi_{13} = \frac{K_f}{M_s w_o^{\ 2}} \quad 3.27$$

$$\pi_{14} = \frac{K_{tf}}{M_s w_o^{\ 2}} \quad 3.28$$

$$\pi_{15} = \frac{F_r}{M_s w_o^{\ 2} Z_{cm}} \quad 3.29$$

$$\pi_{16} = \frac{F_f}{M_s w_o^{\ 2} Z_{cm}} \quad 3.30$$

These Pi-numbers are not the only independent set of Pi-numbers for this system. Iin fact, choosing different primary quantities results in a different dimensional table, and consequently a different set of independent Pi-numbers. A Pi-number of an independent set can be stated as the power product of the Pi-numbers of the other independent sets, and is not independent from them.

Even though all obtained Pi-numbers are required in order to derive the dimensionless equations, just the representative Pi-numbers are enough to obtain the scale factors. In order to obtain the representative pi-numbers, the dimensional table is established using

the representative quantities. A representative quantity is used to represent all the quantities with the same unit. The representative quantities of the half car model are k, b, F, m, w, J and l which represent stiffness, damping coefficient, force, mass, frequency, moment of inertia, and length, respectively. The four representative pi-numbers of the half car model are as follows:

$$\begin{cases} \Pi_1 = \dfrac{k}{m * w^2} & Stiffness \quad Pi\_number & 3.31 \\ \Pi_2 = \dfrac{b}{m * w} & Damping \quad Pi\_number & 3.32 \\ \Pi_3 = \dfrac{F}{m * w^2 * l} & Force \quad Pi\_number & 3.33 \\ \Pi_4 = \dfrac{J}{m * l^2} & Inertia \quad Pi\_number & 3.34 \end{cases}$$

In order to have a similitude model, these pi-numbers should remain the same for the full scale and the scaled model.

3.3.2 Dimensionless Mathematical Model

Before transforming the equations of motion to the dimensionless space, in addition to pi-numbers, the dimensionless variables should be determined. The variables or states of the half car model are the sprung mass and unsprung masses, the vertical displacements, the velocities and accelerations, the sprung mass pitch angle, and its angular velocity and acceleration. The displacements can be made dimensionless by dividing by a representative length such as the height of the centre of mass. The velocities and accelerations can be transformed by dividing by a representative velocity and acceleration respectively such as $Z_{cm}w_0$ and $Z_{cm}w_0{}^2$. The angular velocities and accelerations can be made dimensionless by dividing by a representative angular velocity and acceleration such as w_0 and $w_0{}^2$. Table 3.2 shows the dimensionless variables.

Table 3.2: Dimensionless variables of the half car model

Displacement	Velocity	Acceleration	Angular Velocity	Angular Acceleration
$\overline{Z_{ur}} = \frac{Z_{ur}}{Z_{cm}}$	$\dot{\overline{Z}}_{ur} = \frac{\dot{Z}_{ur}}{Z_{cm} w_0}$	$\ddot{\overline{Z}}_{ur} = \frac{\ddot{Z}_{ur}}{Z_{cm} w_0^2}$	$\dot{\overline{\theta}} = \frac{\dot{\theta}}{w_o}$	$\ddot{\overline{\theta}} = \frac{\ddot{\theta}}{w_o^2}$
$\overline{Z_{uf}} = \frac{Z_{uf}}{Z_{cm}}$	$\dot{\overline{Z}}_{uf} = \frac{\dot{Z}_{uf}}{Z_{cm} w_0}$	$\ddot{\overline{Z}}_{uf} = \frac{Z_{uf}}{Z_{cm} w_0^2}$		
$\overline{Z_s} = \frac{Z_s}{Z_{cm}}$	$\dot{\overline{Z}}_s = \frac{\dot{Z}_s}{Z_{cm} w_0}$	$\ddot{\overline{Z}}_s = \frac{\ddot{Z}_s}{Z_{cm} w_0^2}$		

Since Equations 3.1- 3.3 are the equations of forces, they can be made dimensionless by dividing both sides by representative forces such as $m_s w_o^{\,2} Z_{cm}$, $m_{uf} w_o^{\,2} Z_{cm}$, or $m_{ur} w_o^{\,2} Z_{cm}$. Equation 3.4, which is an equation of torque, is made dimensionless by dividing both sides by a representative torque such as $J w_o^{\,2}$. The resulting dimensionless equations are as follows:

$$\ddot{\overline{Z}}_{ur} = -\frac{(K_r + K_{tr})}{M_{ur} w_0^{\,2}} \overline{Z_{ur}} - \frac{B_r}{M_{ur} w_0} \dot{\overline{Z}}_{ur} + \frac{K_r}{M_{ur} w_0^{\,2}} \overline{Z_s} + \frac{B_r}{M_{ur} w_0} \dot{\overline{Z}}_s - \frac{K_r}{M_{ur} w_0^{\,2}} \frac{b}{Z_{cm}} \theta - \frac{B_r}{M_{ur} w_0} \frac{b}{Z_{cm}} \dot{\theta} + \frac{K_{tr}}{M_{ur} w_0^{\,2}} \overline{Z_{rr}} + \frac{1}{M_{ur} Z_{cm} w_0^{\,2}} F_r \qquad 3.35$$

$$\ddot{\overline{Z}}_{uf} = -\frac{(K_f + K_{tf})}{M_{uf} w_0^{\,2}} \overline{Z_{uf}} - \frac{B_f}{M_{uf} w_0} \dot{\overline{Z}}_{uf} + \frac{K_f}{M_{uf} w_0^{\,2}} \overline{Z_s} + \frac{B_f}{M_{uf} w_0} \dot{\overline{Z}}_s + \frac{K_f}{M_{uf} w_0^{\,2}} \frac{a}{Z_{cm}} \theta + \frac{B_f}{M_{uf} w_0} \frac{a}{Z_{cm}} \dot{\theta} + \frac{K_{tf}}{M_{uf} w_0^{\,2}} \overline{Z_{rf}} + \frac{1}{M_{uf} Z_{cm} w_0^{\,2}} F_f \qquad 3.36$$

$$\ddot{\bar{Z}}_s = \frac{K_r}{M_s w_0^{\,2}}\overline{Z_{ur}} + \frac{B_r}{M_s w_0}\dot{\bar{Z}}_{ur} + \frac{K_f}{M_s w_0^{\,2}}\overline{Z_{uf}} + \frac{B_f}{M_s w_0}\dot{\bar{Z}}_{uf} - \frac{(K_r+K_f)}{M_s w_0^{\,2}}\overline{Z_s}$$
$$- \frac{(B_r+B_f)}{M_s w_0}\dot{\bar{Z}}_s + \left(\frac{b}{Z_{cm}}\frac{K_r}{M_s w_0^{\,2}} - \frac{K_f}{M_s w_0^{\,2}}\frac{a}{Z_{cm}}\right)\theta + \left(\frac{b}{Z_{cm}}\frac{B_r}{M_s w_0} - \frac{B_f}{M_s w_0}\frac{a}{Z_{cm}}\right)\dot{\theta}$$
$$- \frac{F_r}{M_s w_0^{\,2} Z_{cg}} - \frac{F_f}{M_s w_0^{\,2} Z_{cg}} \qquad 3.37$$

$$\ddot{\bar{\theta}} = -\frac{\frac{b}{Z_{cm}}\frac{K_r}{M_s w_0^{\,2}}}{\frac{J}{Z_{cm}^{\,2} M_s}}\bar{Z}_{ur} - \frac{\frac{b}{Z_{cm}}\frac{B_r}{M_s w_0}}{\frac{J}{Z_{cm}^{\,2} M_s}}\dot{\bar{Z}}_{ur} + \frac{\frac{a}{Z_{cm}}\frac{K_f}{M_s w_0^{\,2}}}{\frac{J}{Z_{cm}^{\,2} M_s}}Z_{uf}$$
$$+ \left(\frac{\frac{b}{Z_{cm}}\frac{K_r}{M_s w_0^{\,2}}}{\frac{J}{Z_{cm}^{\,2} M_s}} - \frac{\frac{a}{Z_{cm}}\frac{K_f}{M_s w_0^{\,2}}}{\frac{J}{Z_{cm}^{\,2} M_s}}\right)\bar{Z}_s + \frac{\frac{a}{Z_{cm}}\frac{B_f}{M_s w_0}}{\frac{J}{Z_{cm}^{\,2} M_s}}\dot{\bar{Z}}_{uf} +$$
$$\left(\frac{\frac{b}{Z_{cm}}\frac{B_r}{Z_{cm} M_s w_0}}{\frac{J}{Z_{cm}^{\,2} M_s}} - \frac{\frac{a}{Z_{cm}}\frac{B_f}{Z_{cm} M_s w_0}}{\frac{J}{Z_{cm}^{\,2} M_s}}\right)\dot{\bar{Z}}_s - \left(\frac{\frac{(\frac{b}{Z_{cm}})^2\frac{K_r}{M_s w_0^{\,2}}}{\frac{J}{Z_{cm}^{\,2} M_s}}}{} + \frac{\frac{(\frac{a}{Z_{cm}})^2\frac{K_f}{M_s w_0^{\,2}}}{\frac{J}{Z_{cm}^{\,2} M_s}}}{}\right)\theta - \left(\frac{\frac{(\frac{b}{Z_{cm}})^2\frac{B_r}{Z_{cm} M_s w_0}}{\frac{J}{Z_{cm}^{\,2} M_s}} + \frac{\frac{(\frac{a}{Z_{cm}})^2\frac{B_f}{Z_{cm} M_s w_0}}{\frac{J}{Z_{cm}^{\,2} M_s}}}{}\right)\dot{\bar{\theta}}$$
$$+ \frac{\frac{b}{Z_{cm}}\frac{F_r}{M_s Z_{cm} w_0^{\,2}}}{\frac{J}{Z_{cm}^{\,2} M_s}} - \frac{\frac{a}{Z_{cm}}\frac{F_f}{M_s Z_{cm} w_0^{\,2}}}{\frac{J}{Z_{cm}^{\,2} M_s}} \qquad 3.38$$

Substituting the Pi-numbers from Equations 3.15-3.30 into Equations 3.35-3.38 gives.

$$\ddot{\bar{Z}}_{ur} = -\frac{(\pi_1+\pi_3)}{\pi_5}\overline{Z_{ur}} - \frac{\pi_2}{\pi_5}\dot{\bar{Z}}_{ur} + \frac{\pi_1}{\pi_5}\overline{Z_s} + \frac{\pi_1}{\pi_5}\dot{\bar{Z}}_s - \frac{\pi_1\pi_7}{\mu_5}\theta - \frac{\pi_2\pi_7}{\pi_5}\dot{\bar{\theta}}$$
$$+ \frac{\pi_3}{\pi_5}\overline{Z_{rr}} + \frac{\pi_{15}}{\pi_5} \qquad 3.39$$

$$\ddot{\overline{Z}}_{uf} = -\frac{(\pi_{13}+\pi_{14})}{\pi_5}\overline{Z_{uf}} - \frac{\pi_4}{\pi_5}\dot{\overline{Z}}_{uf} + \frac{\pi_{13}}{\pi_5}\overline{Z_s} + \frac{\pi_{14}}{\pi_5}\dot{\overline{Z}}_s + \frac{\pi_{13}\pi_6}{\pi_5}\theta + \frac{\pi_4\pi_6}{\pi_5}\dot{\theta} + \frac{\pi_{14}}{\pi_5}\overline{Z_{rr}} + \frac{\pi_{15}}{\pi_5} \quad 3.40$$

$$\ddot{\overline{Z}}_s = \pi_1\overline{Z_{ur}} + \pi_2\dot{\overline{Z}}_{ur} + \pi_{13}\overline{Z_{uf}} + \pi_4\dot{\overline{Z}}_{uf} - (\pi_1+\pi_{13})\overline{Z_s} - (\pi_2+\pi_4)\dot{\overline{Z}}_s + (\pi_1\pi_7+\pi_6\pi_{13})\theta + (\pi_2\pi_7+\pi_4\pi_6)\dot{\theta} - \pi_{15} + \pi_{16} \quad 3.41$$

$$\ddot{\theta} = -\frac{\pi_1\pi_7}{\pi_9}\overline{Z_{ur}} - \frac{\pi_2\pi_7}{\pi_9}\dot{\overline{Z}}_{ur} + \frac{\pi_6\pi_{13}}{\pi_9}\overline{Z_{uf}} + \frac{\pi_6\pi_4}{\pi_9}\dot{\overline{Z}}_{uf} + \left(\frac{\pi_1\pi_7-\pi_6\pi_{13}}{\pi_9}\right)\overline{Z_s} + \left(\frac{\pi_2\pi_7-\pi_6\pi_4}{\pi_9}\right)\dot{\overline{Z}}_s - \left(\frac{{\pi_7}^2\pi_1}{\pi_9} + \frac{{\pi_6}^2\pi_{13}}{\pi_9}\right)\theta - \left(\frac{{\pi_7}^2\pi_2}{\pi_9} + \frac{{\pi_6}^2\pi_4}{\pi_9}\right)\dot{\theta} + \frac{\pi_7\pi_{15}}{\pi_9} - \frac{\pi_6\pi_{16}}{\pi_9} \quad 3.42$$

Equations 3.39 to 3.42 are the dimensionless equations of motion of a half car model in terms of Pi-numbers. The derived dimensionless mathematical model is applicable to all half car models which have the same pi-numbers.

3.4 Scale Model of Honda Civic (Sedan)

According to the similitude theorem, the necessary and sufficient condition to have two similitude models is that the two systems have the same dimensionless mathematical model [40]. The dimensionless equations of motion ensure that if two systems have the same Pi-numbers, they have the same dimensionless mathematical model. On the other hand, having the same representative Pi-numbers guarantees that all Pi-numbers of two systems are the same. While the Pi-numbers for the two systems have to be the same, the scale factors of the different system parameters generally vary to satisfy equality of the Pi-numbers. Let C_T, C_L, C_m, C_K, C_B and C_F be respectively, the scale factors corresponding to time, length, mass, damping, stiffness and force. k, m, l, w, b and F are assumed to be the representative parameters of the scaled model, and k', m'

$, l', w'$, b' and F' to be the representative parameters of the real full scale model. The stiffness Pi-number for the real full scale model can be expressed as follows:

$$\Pi_1' = \frac{k'}{m'w'^2}$$

Writing the full scale parameters in terms of their corresponding scaled parameters and their scale factors gives:

$$\Pi_1' = \frac{C_K C_T^{\,2}}{C_m}\frac{k}{mw^2}$$

Considering Equation 3.31, the two Pi-numbers are related to each other by:

$$\Pi_1' = \frac{C_K C_T^{\,2}}{C_m}\Pi_1 \qquad 3.43$$

For Π_1' and Π_1 to be equal, the following condition must be satisfied:

$$\frac{C_k C_T^{\,2}}{C_m} = 1 \qquad 3.44$$

Using the same approach for the damping and force Pi-numbers, the following results are obtained:

$$\frac{C_B * C_T}{C_m} = 1 \qquad 3.45$$

$$\frac{C_F * C_T^{\,2}}{C_m * C_L} = 1 \qquad 3.46$$

Since the system is fast enough, there is no need to speed down or up the scaled model response. Therefore, it is reasonable to choose

$$C_T = 1 \qquad 3.47$$

Taking account Equations 3.44 and 3.47, one of the scaling laws is obtained as follows:

$$\frac{C_k}{C_m} = 1 \qquad 3.48$$

The force scale factor can be stated in terms of the stiffness and length scale factors as Equation 3.49.

$$C_F = C_k C_L \qquad 3.49$$

The above analyzing shows that the scale factors of mass, stiffness and damping coefficient must be chosen to have the same value, regardless of the scale factor chosen for the length.

Amber of factors should be considered when choosing the scale factor. These are: a) the scaled model should be manageable b) the available testing facilities can be used to carry out the experiments on the scaled model c) a suitable air spring with the desired scaled stiffness is available. The chosen scale factors are as follows:

$$C_k = 12 \tag{3.51}$$

$$C_B = 12 \tag{3.52}$$

$$C_m = 12 \tag{3.53}$$

$$C_L = 5 \tag{3.54}$$

Table 3.3: The specifications of the Honda Civic Sedan [43]

	Specifications
Curb weight	2663 lbs=1207.9 kg
Wheel base length	103.1 in=2618.74 mm
Width	67.5 in 1715 mm
Height of the car	55.6 mm = 1412.24 mm
Weight distribution	F/R: 60/40
Front spring stiffness	671 lbs/in= 117.51 N/mm
Rear spring stiffness	783 lbs/in= 137.124 N/mm
Tire type	P 185/70 R14 87 S
Overall tire width	7.4 in=187.96 mm
Overall tire diameter	24.23 in=615.442 mm

The specifications of the Honda Civic (Sedan) are shown in Table 3.3. Considering the scale factors expressed the parameters of the half car model corresponding to that which shown in Table 3.4.

In order to substitute the conventional spring damper suspension by a pneumatic suspension, a suitable air spring is chosen based on the stiffness of the scaled model. The scaled stiffness is around 70 lbs/in. Among all Firestone and Goodyear air springs, Firestone Model 2M2A Airmount manufactured by Firestone Industrial Products is found to be the most suitable one for the undergoing research [44]. When the pressure is equal to 10 psig and the design height is assumed to be 1.7 inches, the calculated air spring stiffness is around 80 lbs/in.

Table 3.4: The parameters of the half car model

	Specifications
M_s (sprung mass weight)	111 lbs =50.33 kg
M_{us} (unsprung mass weight)	10 lbs= 4.54 kg
L (wheel base length)	20 in=508 mm
a (distance from Center of mass to front axis)	12.37 in=314.2 mm
b (distance from Center of mass to rear axis)	7.63 in=193.8 mm
J (sprung mass moment of inertia)	25.65 lb.in^2=7513 kg.mm^2
W (width)	13.5 in=342.9 mm
Front Suspension	2M2A firestone actuator
Rear suspension	2M2A firestone actuator
K_{tf} (Stiffness of front tire)	80 lbs/in=14kN/m
K_{tr} (Stiffness of rear tire)	80 lbs/in=14 kN/m

3.5 Designing and Building the Similitude Half Car Model

Using the parameters in Table 3.4, a half car model has been designed. Two DC motors are assumed to excite the system. The rotary movements of the DC motors are transformed into the linear vertical displacements, which excite the front and the rear wheel, using two linkages. The mechanism of the designed exciting system is analysed and the required power is calculated. The required power and the maximum torque are, respectively, 0.75 hp and 3.5 N.m. The Pittman Gear Motor model GM14X02 with the gear ratio equal to 19.7:1 is chosen based on these requirements.

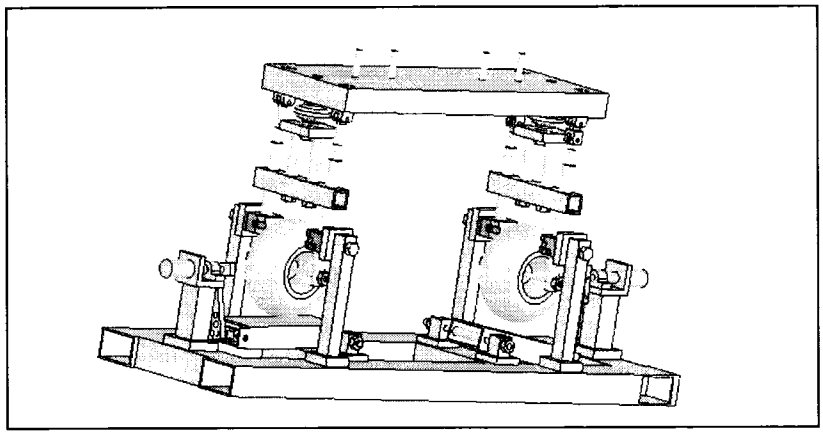

Figure 3.2: The 3D view of the designed scaled half car model

The sprung mass is designed to represent different car bodies with different weights and moments of inertia. As Figure 3.2 shows, four different weights can be mounted at four different positions to achieve different weight distributions and inertias. The engineering drawings of the test rig are shown in Appendix A. The physical model is shown in Figure 3.2.

Chapter 4

Nonlinear Mathematical Model of Pneumatic Suspensions

4.1 Introduction

Mathematical models are useful tools for analysing system behaviours and designing controllers. The more accurate a mathematical model is, the more reliable the analysis and design are. In many cases assumptions must be made in order to obtain a mathematical model that can be dealt with. A good understanding of the physical system is necessary in order to decide on realistic assumptions and simplifications, and consequently design a more reliable and robust controller. In the first part of the present chapter, the detailed mathematical model of an air spring is investigated in detail to identify the possible sources of uncertainties introduced by simplifying assumptions. The dimensionless mathematical model of an air spring is also derived. In the second part, the mathematical models of a quarter car and a half car with a pneumatic suspension are derived and their dimensionless mathematical models presented.

4.2 The Mathematical Model of an Air spring

As was discussed in Chapter 2, when pneumatic cylinders are used as vibration isolator, they offer many advantages over conventional spring/damper suspension systems. The new breed of air springs; on the other hand, have been shown to be superior to traditional pneumatic cylinder isolators. They are durable, operate well in corrosive and abrasive industrial environments. They do not need lubrication, because there is no sliding motion between their components. They tolerate well misalignment, and they have a high ratio of stroke to collapsed height [45]. Figure 4.1 shows an illustration of an air spring with all its components. Unlike a pneumatic cylinder, an air spring does not contain a piston and a cylinder; it has a flexible wall connecting the upper bead plate to a piston which is typically connected to the vibration source.

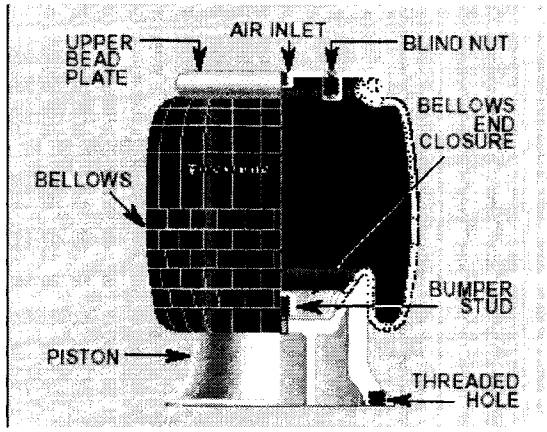

Figure 4.1: Firestone Air Spring

Based on the manufacturer literature, when an air spring is used as an isolator, two different configurations can be used. The difference between the two configurations lie in the way the rubber bellows is supported during operation. In configuration (a) the bellows is allowed to roll over the bead plate and the piston, while in configuration (b) the bellows is restricted from rolling and is faced to balloon. In this work configuration (b) is used. It should be noted, however, that the Firestone catalogue data are based on configuration (a) for the 2M2A air spring used in this research.

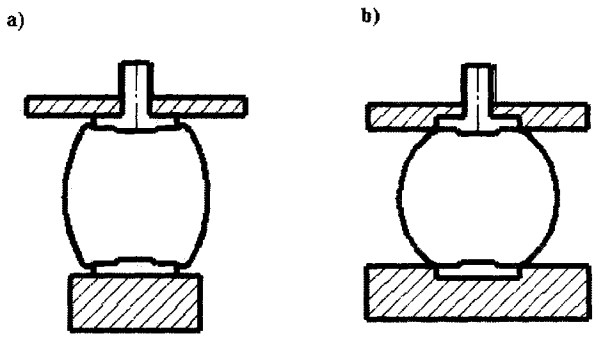

Figure 4.2: Illustration of the two possible configurations for using the Firestone air springs

An air spring has inlet and outlet orifices which control the air spring pressure and volume, and consequently the assembly stroke. The air spring is usually used in conjunction with an air supply.

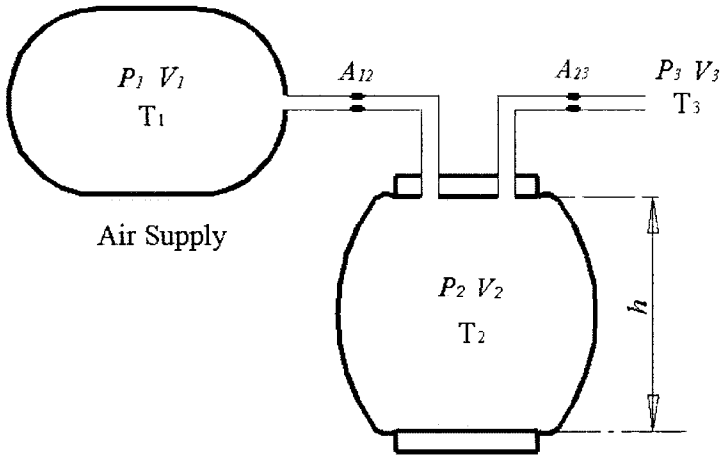

Figure 4.3: Air Spring pneumatic system

Figure 4.3 shows a schematic diagram of an air spring pneumatic system. Air flows from an air supply into the air spring through the inlet orifice A_{12} and flows out into the atmosphere through the outlet orifice A_{23}. The upstream and downstream states of the inlet orifice are assumed to be the same as the supply and air spring states respectively. The upstream and downstream states of the outlet orifice are also the same as the air spring and atmosphere states respectively. P, T, h, W and V denote pressure, temperature, height, mass flow rate and volume, respectively. The states of the supply, air spring and atmosphere are denoted by indices 1, 2 and 3 respectively. The parameters of the inlet and the outlet orifices are denoted by subscripts "12" and "23" respectively.

The mass flow rate W_{12} through the inlet orifice is given by:

$$W_{12} = \rho_2 A_{12} u_2 \qquad 4.1$$

where ρ_2 is the density of air at this cross section. The density ρ_2 and the velocity u_2 can be stated in terms of the supply and the air spring pressures by considering air as an ideal gas and assuming the process to be polytropic. Assuming that the air velocity at the supply is zero i.e. stagnation pressure, the relationship between that pressure and the air spring pressure is given by:

$$P_1 = P_2\left(1+\frac{n-1}{2gnRT_1}u_2^{\,2}\right)^{\frac{-n}{n-1}} \qquad 4.2$$

where P_1, P_2, u_2, T_1 and n are the stagnation pressure (total pressure), the air spring static pressure, the average velocity at the orifice cross section, the total temperature and the polytropic process coefficient, respectively[46]. The detail derivation of Equation 4.2 is given in Appendix B. The value of n depends on the construction of the air spring and the operating condition. For well insulated and rapid oscillation n is close to 1.4, while for uninsulated and slow oscillation n is close to 1. Solving Equation 4.2 for u_2 yields:

$$u_2 = \left\{ \frac{2gRT_1 n}{n-1} \left[1 - \left(\frac{P_2}{P_1} \right)^{\frac{n-1}{n}} \right] \right\}^{\frac{1}{2}} \tag{4.3}$$

It should be noted that while Equation 4.3 is valid for the theoretical limits of 1.4 and 1, in the case of isothermal process where n=1 yields $P_1 = P_2$ and $u_2 = 0$. Hence Equation 4.3 is meaningful if the process is assumed isothermal. The polytropic relationship between the air spring states and the supply states can be expressed as follows:

$$\frac{\rho_2}{\rho_1} = \left(\frac{P_2}{P_1} \right)^{\frac{1}{n}} \tag{4.4}$$

The equation of the state of an ideal gas expresses the relationship between the supply states as follows:

$$P_1 = \rho_1 R T_1 \tag{4.5}$$

where R is the gas constant. Substituting for P_1 in Equation 4.4 and rearranging gives:

$$\rho_2 = \frac{P_1}{RT_1} \left(\frac{P_2}{P_1} \right)^{\frac{1}{n}} \tag{4.6}$$

Substituting Equations 4.3 and 4.6 into Equation 4.1 yields:

$$W_{12} = \frac{A_{12} P_1}{\sqrt{T_1}} \left\{ \frac{2gn}{(n-1)R} \left[\left(\frac{P_2}{P_1} \right)^{\frac{2}{n}} - \left(\frac{P_2}{P_1} \right)^{\frac{n+1}{n}} \right] \right\}^{\frac{1}{2}} \tag{4.7}$$

Equation 4.7 states the mass flow rate in terms of the ratio of the air spring pressure to the supply pressure. When the ratio of pressure $\frac{P_2}{P_1}$ is such that sonic conditions exist at the inlet orifice, W_{12} reaches its maximum value and the flow is termed critical, W_{cr}. The ratio of the mass flow rate to that at critical is designated N_{12} and is given by:

$$N_{12} = \frac{W_{12}}{W_{cr}} = \left\{ \frac{\left[\left(\frac{P_2}{P_1} \right)^{\frac{2}{n}} - \left(\frac{P_2}{P_1} \right)^{\frac{n+1}{n}} \right]}{\frac{(n-1)}{2} \left(\frac{2}{n+1} \right)^{\frac{n+1}{n-1}}} \right\}^{\frac{1}{2}} \qquad 4.8$$

Defining a constant K as follows:

$$K = \left[\frac{ng}{R} \left(\frac{2}{n+1} \right)^{\left(\frac{n+1}{n-1}\right)} \right]^{\frac{1}{2}} \qquad 4.9$$

and substituting for N_{12} and K into Equation 4.7 gives:

$$W_{12} = \frac{KP_1 A_{12} N_{12}}{\sqrt{T_1}} \qquad 4.10$$

Similarly the mass flow rate through the outlet orifice is given by:

$$W_{23} = \frac{KP_2 A_{23} N_{23}}{\sqrt{T_2}} \qquad 4.11$$

where,

$$N_{23} = \frac{W_{23}}{W_{cr}} = \left\{ \frac{\left[\left(\frac{P_3}{P_2} \right)^{\frac{2}{n}} - \left(\frac{P_3}{P_2} \right)^{\frac{n+1}{n}} \right]}{\frac{(n-1)}{2} \left(\frac{2}{n+1} \right)^{\frac{n+1}{n-1}}} \right\}^{\frac{1}{2}} \qquad 4.12$$

As air flows into the air spring and out to the atmosphere, the air spring pressure changes. The change in the pressure results from the change in the air mass inside the air spring, the change in temperature and the air spring volume. The ideal gas equation expressing the air mass inside the air spring in terms of the other states is given by:

$$M_2 = \frac{P_2 V_2}{R T_2} \qquad 4.13$$

Differentiating Equation 4.13 and rearranging gives the overall changes of the air spring pressure due to change in the state as follows:

$$dP_2 = \frac{\partial P_2}{\partial T_2} dT_2 + \frac{\partial P_2}{\partial M_2} dM_2 - \frac{\partial P_2}{\partial V_2} dV_2 \qquad 4.14$$

The partial derivatives of the air spring pressure with respect to individual changes in air mass, volume, and temperature are given by:

$$\begin{cases} \dfrac{\partial P_2}{\partial V_2} = -\dfrac{RM_2T_2}{V_2^{\,2}} = \dfrac{P_2}{V_2} \\ \dfrac{\partial P_2}{\partial M_2} = \dfrac{RT_2}{V_2} = \dfrac{P_2}{M_2} \\ \dfrac{\partial P_2}{\partial T_2} = \dfrac{RM_2}{V_2} = \dfrac{P_2}{T_2} \end{cases} \tag{4.15}$$

Substituting these derivatives into Equation 4.14 and rearranging gives:

$$\frac{dP_2}{P_2} = \frac{dT_2}{T_2} + \frac{dM_2}{M_2} - \frac{dV_2}{V_2} \tag{4.16}$$

It should be noted however, that the temperature and the pressure of the air spring are not independent. Assuming a polytropic process, the relationship between the temperature and pressure changes is given by:

$$\frac{dT_2}{T_2} = \frac{n-1}{n}\frac{dP_2}{P_2} \tag{4.17}$$

Substituting M_2 from Equation 4.13 and $\dfrac{\partial T_2}{T_2}$ from Equation 4.17 into Equation 4.16 and rearranging gives:

$$dP_2 = -\frac{nP_2}{V_2}dV_2 + \frac{nRT_2}{V_2}dM_2 \tag{4.18}$$

Dividing both sides of Equation 4.18 by *dt*, the time derivative of the air spring pressure is expressed in terms of the time derivative of the air spring volume and the time derivative of the air mass as follows:

$$\frac{dP_2}{dt} = -\frac{nP_2}{V_2}\frac{dV_2}{dt} + \frac{nRT_2}{V_2}\frac{dM_2}{dt} \tag{4.19}$$

Equation 4.19 implies that the air spring pressure change is caused by two factors, the change in the air spring volume and the change in the air mass inside that volume. The derivative of the air mass inside the air spring can be expressed in terms of the inlet and the outlet mass flow rate as follows:

$$\frac{dM_2}{dt} = W_{12} - W_{23} \tag{4.20}$$

Substituting Equation 4.10 and Equation 4.11 into Equation 4.20, the time derivative of the air mass inside the air spring is expressed in terms of the supply and atmospheric pressures and temperatures as follows:

$$\frac{dM2}{dt} = \frac{KP_1 A_{12} N_{12}}{\sqrt{T_1}} - \frac{KP_2 A_{23} N_{23}}{\sqrt{T_2}} \qquad 4.21$$

Substituting Equation 4.21 into Equation 4.19, the time derivative of the pressure is given by:

$$\frac{dP_2}{dt} = -\frac{nP_2}{V_2}\frac{dV_2}{dt} + \frac{nKRP_2\sqrt{T_1}}{V_2}\left[\frac{T_2}{T_1}\left(N_{12}\frac{P_1}{P_2}\right)A_{12} - \left(\frac{T_2}{T_1}\right)^{\frac{1}{2}} A_{23}N_{23}\right] \qquad 4.22$$

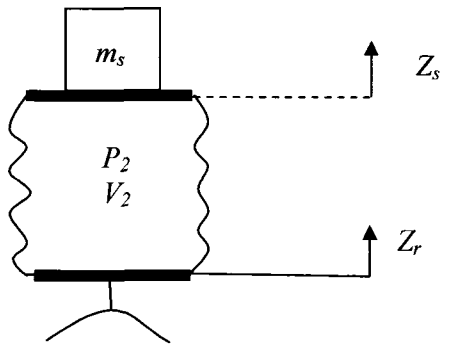

Figure 4.4: An air spring supporting a payload

Assuming that the air spring supports a mass m_s which has a vertical position Z_s as shown in Figure 4.4, the balance of forces on the air spring is given by :

$$m_s \ddot{Z}_s = P_2 A - m_s g \qquad 4.23$$

where A is the air spring effective area.

All the parameters of the air spring model derived above can be determined or directly measured with the exception of the air spring volume, the volume derivative and the effective area. The effective area and the volume of the air spring cannot be measured directly by sensors; therefore, a method should be adopted to obtain these parameters. For a pneumatic cylinder, the effective area and the cross section area are the same, but for an air spring with a flexible wall, the effective area is not the same as its cross section area or any other physical or measurable properties. In fact, it is an imaginary area for defining the air spring developed force. The effective area is a function of the

air spring pressure and its assembly height. The effective area can be inferred directly from experimental measurement as will be shown later.

Assuming a polytropic process, the pressure and volume of the air spring at a specific air spring height can be related to the volume and pressure at 60 psig at the same height by the following equation:

$$P_{@60}V_{@60}{}^{n} = P_2V_2{}^{n} \tag{4.24}$$

The volume of the air spring for different air spring heights at 60 psig is provided in the force table, Table 4.1, of the Firestone engineering manual and design guide [44]

Table 4.1: The force table of the Firestone 2M2A air spring taken from [44]

Force Table (Use for Airstroke™ actuator design)						
Assembly Height (in.)	Volume @ 60 PSIG (in^3)	Pounds Force				
		@20 PSIG	@40 PSIG	@60 PSIG	@80 PSIG	@100 PSIG
2.2	5.37	40	76	110	140	160
2.0	4.88	44	88	127	167	205
1.8	4.39	52	95	140	184	228
1.6	3.90	52	97	144	192	240
1.4	3.42	52	99	148	196	242
1.2	2.93	52	98	148	196	242

The air spring height h is given by:

$$h = Z_s - Z_r \tag{4.25}$$

The mean cross section area A_{mean} can be calculated by dividing the air spring volume by the air spring height as follows:

$$A_{mean} = \frac{V_2}{h} \tag{4.26}$$

The time derivative of the air spring height can be calculated by differentiating the air spring height, or directly by sensors. The time derivative of the volume is obtained as:

$$\frac{dV_2}{dt} = A_{mean}\frac{dh}{dt} \tag{4.27}$$

Equations 4.22 to 4.27 comprise the mathematical model of an air spring connected to a supply and a sink through inlet and outlet orifices.

4.3 The similitude Model of an Air Spring

As was shown in Chapter 3, if the mathematical models of two systems can be mapped to a unique dimensionless equation, those are similitude systems. In this section a similitude model of an air spring is derived.

The dimensions of length (L), mass (M), time (T) and temperature (Te) are chosen as the basic units of this system. The air spring volume $\mathbf{V_2}$, effective area $\mathbf{A_{eff}}$, and natural frequency **w** at 100 psig and the recommended design height in addition to the maximum area of the orifice **A**, maximum assembly height of the air spring **h** and the supported mass m_s are considered as the primary quantities. These quantities are denoted by non-italic bold letters and their values are available on the air spring engineering manual [44] and the pneumatic valve catalogue.

Table 4.2: The table of dynamic characteristics at recommended design height for 2M2A Firestone air spring taken from [44]

Dynamic Characteristics at 1.8 in. Design Height (Required for Airmount isolator design only)				
Volume @ 100 PSIG = 4.39 in³			Natural Frequency	
Gage Pressure (PSIG)	Load (lbs.)	Spring Rate (lbs./in.)	CPM	HZ
40	95	122	213	3.55
60	140	175	210	3.51
80	184	230	210	3.51
100	228	289	211	3.53

For example, **w** , $\mathbf{V_2}$ and **h** for 2M2A Firestone air spring can be obtained directly from Table 4.2 and Table 4.1. $\mathbf{A_{eff}}$ can be calculated by dividing the load at the maximum assembly height and 100 psig , determined in Table 4.2, by 100 psig.

Following the same procedure presented in Chapter 3 and establishing the dimensional table for the quantities of this system, the following Pi-numbers are obtained:

$$\Pi_{12} = \frac{nKR\sqrt{T_1}\mathbf{A}}{\mathbf{wV_2}} \tag{4.28}$$

$$\Pi_P = \frac{P_1\mathbf{A_{eff}}}{m_s\mathbf{hw}^2} \tag{4.29}$$

Considering the mathematical model of the air spring, Equation 4.22, N_{12} and N_{23} are dimensionless variables. Additional system variables are cast in nondimensional form as follows:

$$C_{12} = N_{12}\frac{P_1}{P_2} \tag{4.30}$$

$$\overline{A}_{23} = \frac{A_{23}}{\mathbf{A}} \tag{4.31}$$

$$\overline{A}_{12} = \frac{A_{12}}{\mathbf{A}} \tag{4.32}$$

$$\overline{T}_{12} = \frac{T_2}{T_1} \tag{4.33}$$

$$\overline{P}_{21} = \frac{P_2}{P_1} \tag{4.34}$$

$$\overline{P}_{32} = \frac{P_3}{P_2} \tag{4.35}$$

$$\overline{Z_s} = \frac{Z_s}{\mathbf{h}} \tag{4.36}$$

$$\ddot{\overline{Z}}_s = \frac{\ddot{Z}_s + g}{\mathbf{hw}^2} \tag{4.37}$$

$$\dot{\overline{P}}_{21} = \frac{\dot{P}_2}{\mathbf{w}P_1} \tag{4.38}$$

$$\dot{\overline{V}}_2 = \frac{\dot{V}_2}{\mathbf{wV_2}} \tag{4.39}$$

$$\overline{V}_2 = \frac{V_2}{\mathbf{V_2}} \tag{4.40}$$

$$\overline{A}_{eff} = \frac{A}{\mathbf{A_{eff}}} \tag{4.41}$$

Dividing both sides of Equations 4.22 and 4.23 by $P_1\mathbf{w}$ and $m_s\mathbf{hw}^2$, respectively, these equations are made dimensionless. Rearranging the obtained equations and substituting the Pi-numbers and dimensionless variables, the dimensionless equations of the system are obtained as follows:

$$\ddot{\bar{Z}}_s = \Pi_P \bar{A}_{eff} \bar{P}_{21}$$

$$\dot{\bar{P}}_{21} = -\frac{n\dot{\bar{V}}_2 \bar{P}_{21}}{\bar{V}_2} + \frac{\Pi_{12}\bar{P}_{21}}{\bar{V}_2}(\bar{T}_{12}C_{12}\bar{A}_{12} - (\bar{T}_{12})^{\frac{1}{2}} N_{23}\bar{A}_{23})$$

$$N_{12} = \frac{W_{12}}{W_{cr}} = \left\{ \frac{\left[(\bar{P}_{21})^{\frac{2}{n}} - (\bar{P}_{21})^{\frac{n+1}{n}} \right]}{\frac{(n-1)}{2}\left(\frac{2}{n+1}\right)^{\frac{n+1}{n-1}}} \right\}^{\frac{1}{2}} \qquad 4.42$$

$$N_{23} = \frac{W_{23}}{W_{cr}} = \left\{ \frac{\left[(\bar{P}_{32})^{\frac{2}{n}} - (\bar{P}_{32})^{\frac{n+1}{n}} \right]}{\frac{(n-1)}{2}\left(\frac{2}{n+1}\right)^{\frac{n+1}{n-1}}} \right\}^{\frac{1}{2}}$$

Equations 4.42 imply that the necessary and sufficient condition to have the similitude scaled air spring is that the obtained Pi-numbers have the same values for the scaled model and the full scale model. The scale factor of the orifice diameter can be chosen different from the scale factor of the length. The scale factors of pressure, length, time, temperature, mass and orifice diameter are denoted by C_P, C_L, C_T, C_{Te}, C_m and C_d, respectively. Assuming that the parameters with prime are those of the full scale model, Π_{12}' can be written as follows:

$$\Pi_{12}' = \frac{nKR\sqrt{T_1'}\mathbf{A}'}{\mathbf{w}'\mathbf{V}_2'}$$

It should be noted that K and R are dimensional constants whose values do not change by scaling. Writing the full scale quantities in terms of their corresponding scaled parameters and scale factors, the following equation is obtained:

$$\Pi_{12}' = \frac{(C_{Te})^{0.5} C_T (C_d)^2}{(C_L)^3}\Pi_{12} \qquad 4.43$$

To have Π_{12}' equal to Π_{12}, the following condition must be satisfied:

$$\frac{(C_{Te})^{0.5} C_T (C_d)^2}{(C_L)^3} = 1 \qquad 4.44$$

Assuming $C_{Te} = 1$ and $C_T = 1$, then substituting them into Equation 4.44 and rearranging gives:

$$C_d = C_L^{\frac{3}{2}} \qquad 4.45$$

Equation 4.45 is the first scaling law of the system.

Moreover, Π_P' can be written as follows:

$$\Pi_P' = \frac{P_1' \mathbf{A_{eff}}'}{m_s' \mathbf{h}' \mathbf{w}'^2}$$

Writing the full scale quantities in terms of their corresponding scaled quantities and scale factors, the following equation is obtained:

$$\Pi_P' = \frac{C_P C_L C_T^{\,2}}{C_m} \frac{P_1 \mathbf{A_{eff}}}{m_s \mathbf{h} \mathbf{w}^2}$$

$$= \frac{C_P C_L C_T^{\,2}}{C_m} \Pi_P \qquad 4.46$$

For Π_P' and Π_P to be equal, the following condition must be satisfied:

$$\frac{C_P C_L C_T^{\,2}}{C_m} = 1 \qquad 4.47$$

Further, using $C_T = 1$ Equation 4.47 reduces to:

$$C_P = \frac{C_m}{C_L} \qquad 4.48$$

Equation 4.48 is the second scaling law for pneumatic suspension. This equation implies that if the scale factors of length and mass are equal, the pressure behaviour of the two models are the same. Even if the scale factors of length and mass are not equal, as long as Equation 4.45 and 4.48 are satisfied, the two air springs are similitude.

In most of the technical catalogues the air spring stiffness is used as an important parameter. Even though this parameter does not appear in the air spring mathematical model, it would be helpful to obtain the scale factor of the stiffness in terms of the other

scale factors. The force applied from the full scale air spring to the payload can be expressed as:

$$P'A' = K'x' \tag{4.49}$$

Expressing the full scale parameters in terms of the scaled parameters and the scale factors:

$$(C_p C_L^{\ 2})(PA) = (C_K C_L K)(Kx) \tag{4.50}$$

Noting that $(PA) = (Kx)$, Equation 4.50 reduces to:

$$C_K = C_p C_L \tag{4.51}$$

Substituting C_p from Equation 4.48 into Equation 4.51 gives:

$$C_k = C_m \tag{4.52}$$

Equation 4.52 is the same relationship obtained in Chapter 3 for the similitude model of the conventional half car model. This implies that for similitude the air spring stiffness scale and that of the mass must be kept eqiual.

4.4 The Mathematical Model of a Quarter Car Model with Pneumatic Suspension

The quarter car model with pneumatic suspension is illustrated in Figure 4.5. A quarter of the car mass is represented by m_s, which is supported by the air spring. The axle and the wheel support the air spring, and are represented by the unsprung mass m_u. The air spring pressure and volume are respectively denoted by P_2 and V_2. The tire stiffness is represented by a linear massless spring. The road roughness Z_r acts as a disturbance and deviate the system from the equilibrium condition and propagates and causes the heave motion. It is assumed that in the absence of disturbances, the system is at the steady state and Z_r, Z_u, and Z_s are at the initial condition. When the car travels over an uneven road, the wheel moves vertically and Z_r undergoes a change dZ_r.

The system dynamic equations are obtained by applying Newton's second law to sprung and unsprung masses as follows:

$$m_s\ddot{Z}_s = P_2A - m_sg \tag{4.53}$$

$$m_u\ddot{Z}_u = -K_u(Z_u - Z_r) - P_2A - m_ug \tag{4.54}$$

where the air spring pressure P_2 is determined by Equation 4.22. Therefore, the entire mathematical model of a quarter car model with pneumatic suspension is as follows:

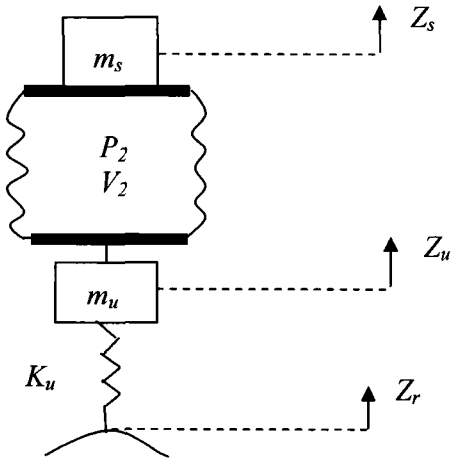

Figure 4.5: The quarter car model with pneumatic suspension

$$\left.\begin{aligned}
&m_s\ddot{Z}_s = P_2A - m_sg \\
&m_u\ddot{Z}_u = -K_u(Z_u - Z_r) - P_2A - m_ug \\
&\frac{dP_2}{dt} = -\frac{nP_2}{V_2}\frac{dV_2}{dt} + \frac{nKRP_2\sqrt{T_1}}{V_2}\left[\frac{T_2}{T_1}\left(N_{12}\frac{P_1}{P_2}\right)A_{12} - \left(\frac{T_2}{T_1}\right)^{\frac{1}{2}}A_{23}N_{23}\right] \\
&V_2 = \left(\frac{P_{@60}V_{@60}{}^n}{P_2}\right)^{\frac{1}{n}}, \quad A_{mean} = \frac{V_2}{Z_s - Z_u}, \quad \frac{dV_2}{dt} = A_{mean}\frac{dh}{dt} \\
&K = \left[\frac{ng}{R}\left(\frac{2}{n+1}\right)^{\left(\frac{n+1}{n-1}\right)}\right]^{\frac{1}{2}}, \quad N_{12} = \frac{W_{12}}{W_{cr}} = \left\{\frac{\left[\left(\frac{P_2}{P_1}\right)^{\frac{2}{n}} - \left(\frac{P_2}{P_1}\right)^{\frac{n+1}{n}}\right]}{\frac{(n-1)}{2}\left(\frac{2}{n+1}\right)^{\frac{n+1}{n-1}}}\right\}^{\frac{1}{2}} \\
&N_{23} = \frac{W_{23}}{W_{cr}} = \left\{\frac{\left[\left(\frac{P_3}{P_2}\right)^{\frac{2}{n}} - \left(\frac{P_3}{P_2}\right)^{\frac{n+1}{n}}\right]}{\frac{(n-1)}{2}\left(\frac{2}{n+1}\right)^{\frac{n+1}{n-1}}}\right\}^{\frac{1}{2}}
\end{aligned}\right\} \tag{4.55}$$

4.5 The Similitude Model of a Quarter Car Model with Pneumatic Suspension

The mathematical model of a quarter car model with pneumatic suspension is consists of the mathematical model of the air spring and the equation of the motion of the unsprung mass, Equation 4.54. The dimensionless mathematical model of an air spring was derived in Section 4.3. In order to obtain the dimensionless form of Equation 4.54, the same basic units and primary quantities as Section 4.3 are used except that unsprung mass m_u is used instead of sprung mass m_s. Applying the dimensional analysis on Equation 4.54, the following dimensionless number and variables are obtained:

$$\overline{Z_u} = \frac{Z_u}{\mathbf{h}} \tag{4.56}$$

$$\overline{Z_r} = \frac{Z_r}{\mathbf{h}} \tag{4.57}$$

$$\ddot{\overline{Z}}_u = \frac{\ddot{Z}_u - g}{\mathbf{hw}^2} \tag{4.58}$$

$$\Pi_{Pu} = \frac{P_1 \mathbf{A_{eff}}}{m_u \mathbf{hw}^2} \tag{4.59}$$

$$\Pi_{Ku} = \frac{K_u}{M_u w^2} \tag{4.60}$$

Dividing both sides of Equation 4.54 by a representative force such as $\mathbf{hw}^2 m_u$ and then substituting for the Pi-numbers and dimensionless variables from Equations 4.56 to 4.60 gives:

$$\ddot{\overline{Z}}_u = -\Pi_{Ku}(\overline{Z}_u - \overline{Z}_r) - \Pi_{Pu}\overline{P}_{21}\overline{A}_{eff} \tag{4.61}$$

Equations 4.42 and 4.61 comprise the dimensionless mathematical model of a quarter car model with pneumatic suspension. A full scale quarter car model and a scaled quarter car model are similitude if in addition to scaling laws obtained for the similitude air spring, the Pi-numbers in Equation 4.61 have the same value for the two models. Substituting full scale parameters in Equations 4.59 and 4.60 by their corresponding scaled parameters, the same scaling laws as Equations 4.48 and 4.52 are obtained. The scaling laws of similitude quarter car models with pneumatic suspension can be summarized as follows:

$$C_T = 1$$

$$C_{Te} = 1$$

$$C_P = \frac{C_m}{C_L} \qquad 4.62$$

$$C_k = C_m$$

$$C_d = (C_L)^{\frac{3}{2}}$$

4.6 The Mathematical Model of a Half Car Model with Pneumatic Suspension

Figure 4.6 illustrates a pneumatic half car model. The car body is modeled as a beam with 2 degrees of freedom; are the heave displacement Z_s and the pitch angle θ. The mass of the car body is equal to m_s and its moment of inertia is equal to J. The parameters of the front and rear axles are denoted by subscripts "*r*" and "*f*", respectively.

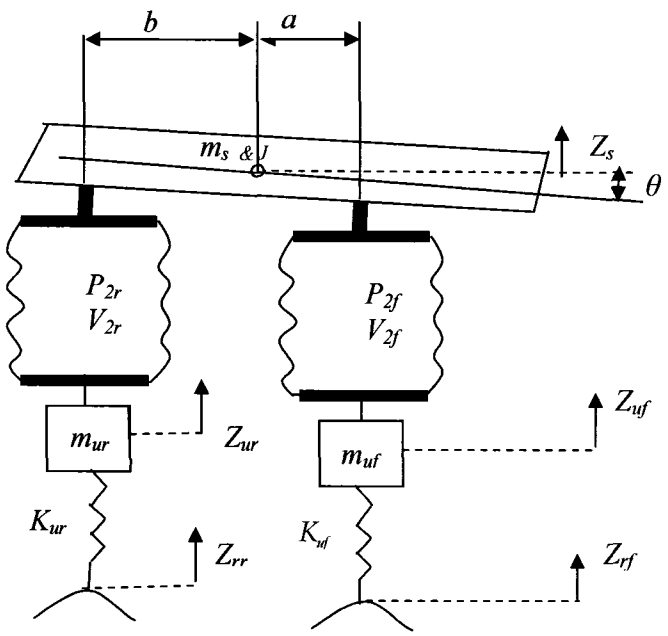

Figure 4.6: Half car model with pneumatic suspension

The front and rear axles are represented by two concentrated masses denoted m_{uf} and m_{ur}. Each unsprung mass has one degree of freedom. Therefore, the whole model has 4 degrees of freedom. Equation 4.22 describes the dynamics of the front and rear air springs. The mathematical model of the half car model is hence given by:

$$m_s \ddot{Z}_s = P_{2f} A_f + P_{2r} A_r - m_s g \tag{4.63}$$

$$J\ddot{\theta} = aP_{2f} A_f - bP_{2r} A_r \tag{4.64}$$

$$m_{uf} \ddot{Z}_{uf} = -K_{uf}(Z_{uf} - Z_{rf}) - P_{2f} A_f - m_{uf} g \tag{4.65}$$

$$m_{ur} \ddot{Z}_{ur} = -K_{ur}(Z_{ur} - Z_{ur}) - P_{2r} A_r - m_{ur} g \tag{4.66}$$

$$\frac{dP_{2f}}{dt} = -\frac{nP_{2f}}{V_{2f}}\frac{dV_{2f}}{dt} + \frac{nKRP_{2f}\sqrt{T_1}}{V_{2f}}\left[\frac{T_2}{T_1}\left(N_{12f}\frac{P_1}{P_{2f}}\right)A_{12f} - \left(\frac{T_2}{T_1}\right)^{\frac{1}{2}} A_{23f} N_{23f}\right] \tag{4.67}$$

$$\frac{dP_{2r}}{dt} = -\frac{nP_{2r}}{V_{2r}}\frac{dV_{2f}}{dt} + \frac{nKRP_{2r}\sqrt{T_1}}{V_{2r}}\left[\frac{T_2}{T_1}\left(N_{12r}\frac{P_1}{P_{2r}}\right)A_{12r} - \left(\frac{T_2}{T_1}\right)^{\frac{1}{2}} A_{23r} N_{23r}\right] \tag{4.68}$$

$$N_{12f} = \frac{W_{12f}}{W_{cr}} = \left\{\frac{\left[\left(\frac{P_{2f}}{P_1}\right)^{\frac{2}{k}} - \left(\frac{P_{2f}}{P_1}\right)^{\frac{k+1}{k}}\right]}{\frac{(k-1)}{2}\left(\frac{2}{k+1}\right)^{\frac{k+1}{k-1}}}\right\}^{\frac{1}{2}} \quad N_{12r} = \frac{W_{12r}}{W_{cr}} = \left\{\frac{\left[\left(\frac{P_{2r}}{P_1}\right)^{\frac{2}{k}} - \left(\frac{P_{2r}}{P_1}\right)^{\frac{k+1}{k}}\right]}{\frac{(k-1)}{2}\left(\frac{2}{k+1}\right)^{\frac{k+1}{k-1}}}\right\}^{\frac{1}{2}} \tag{4.69}$$

$$N_{23f} = \frac{W_{23f}}{W_{cr}} = \left\{\frac{\left[\left(\frac{P_3}{P_{2f}}\right)^{\frac{2}{k}} - \left(\frac{P_3}{P_{2f}}\right)^{\frac{k+1}{k}}\right]}{\frac{(k-1)}{2}\left(\frac{2}{k+1}\right)^{\frac{k+1}{k-1}}}\right\}^{\frac{1}{2}} \quad N_{23r} = \frac{W_{23r}}{W_{cr}} = \left\{\frac{\left[\left(\frac{P_3}{P_{2r}}\right)^{\frac{2}{k}} - \left(\frac{P_3}{P_{2r}}\right)^{\frac{k+1}{k}}\right]}{\frac{(k-1)}{2}\left(\frac{2}{k+1}\right)^{\frac{k+1}{k-1}}}\right\}^{\frac{1}{2}} \tag{4.70}$$

$$V_{2f} = \left(\frac{P_{@60} V_{@60}^{\ n}}{P_{2f}}\right)^{\frac{1}{n}}, \quad A_{meanf} = \frac{V_{2f}}{\underbrace{Z_s + a\theta - Z_{uf}}_{h_f}}, \quad \frac{dV_2}{dt} = A_{meanr}\frac{dh_f}{dt} \tag{4.71}$$

$$V_{2r} = \left(\frac{P_{@60} V_{@60}^{\ n}}{P_{2r}}\right)^{\frac{1}{n}}, \quad A_{meanr} = \frac{V_{2r}}{\underbrace{Z_s - b\theta - Z_{ur}}_{h_r}}, \quad \frac{dV_{2r}}{dt} = A_{meanr}\frac{dh_r}{dt} \tag{4.72}$$

4.7 The Similitude Model of a Half Car Model with Pneumatic Suspension

Equations 4.69 to 4.72 are in dimensionless form or include parameters with the same dimensions. The Pi-numbers and dimensionless variables used for the quarter car model with pneumatic suspension, derived in Sections 4.3, can be used here to obtain the dimensionless form of Equations 4.65 to 6.68 and Equation 4.63. The Pi-numbers and dimensionless variables are the same except that those of the front and the rear air spring are denoted by the subscript f and r, respectively. Thus;

$$\Pi_{Kuf} = \frac{K_{uf}}{M_{uf}\mathbf{w}^2} \tag{4.73}$$

Applying the dimensional analysis to Equations 4.64, the following Pi-numbers and dimensionless variables are derived:

$$\Pi_{PJf} = \frac{aP_{1f}A_{efff}}{J\mathbf{w}^2} \tag{4.74}$$

$$\Pi_{PJr} = \frac{bP_{1r}A_{effr}}{J\mathbf{w}^2} \tag{4.75}$$

$$\ddot{\bar{\theta}} = \frac{\ddot{\theta}}{\mathbf{w}^2}$$

These equations are used to map Equations 4.64 to the dimensionless form. Dividing Equations 4.63, 4.64, 4.65, 4.66, 4.67, 4.68 by $\mathbf{hw}^2 m_s$, $J\mathbf{w}^2$ $\mathbf{hw}^2 m_{uf}$, $\mathbf{hw}^2 m_{ur}$, $P_{1f}\mathbf{w}$ and $P_{2f}\mathbf{w}$,respectively, and substituting the Pi-numbers and dimensionless variables, gives:

$$\begin{cases}
\ddot{\bar{Z}}_s = \Pi_{Pf}\bar{A}_{efff}\bar{P}_{21f} + \Pi_{Pr}\bar{A}_{effr}\bar{P}_{21r} \\
\ddot{\bar{\theta}} = \Pi_{PJf}\bar{A}_{efff}\bar{P}_{21f} - \Pi_{PJr}\bar{A}_{effr}\bar{P}_{21r} \\
\ddot{\bar{Z}}_{uf} = -\Pi_{Kuf}(\bar{Z}_{uf} - \bar{Z}_{rf}) - \Pi_{Puf}\bar{A}_{efff}\bar{P}_{21f} \\
\ddot{\bar{Z}}_{ur} = -\Pi_{Kur}(\bar{Z}_{ur} - \bar{Z}_{rr}) - \Pi_{Pur}\bar{A}_{effr}\bar{P}_{21r} \\
\dot{\bar{P}}_{12f} = -\dfrac{n\dot{\bar{V}}_{2f}\bar{P}_{21f}}{\bar{V}_{2f}} + \dfrac{\Pi_{12f}}{\bar{V}_{20}}(\bar{T}_{12f}C_{12f}\bar{A}_{12f} - (\bar{T}_{12f})^{\frac{1}{2}}N_{23f}\bar{A}_{23f}) \\
\dot{\bar{P}}_{12r} = -\dfrac{n\dot{\bar{V}}_{2r}\bar{P}_{21r}}{\bar{V}_{2r}} + \dfrac{\Pi_{12r}}{\bar{V}_{20}}(\bar{T}_{12r}C_{12r}\bar{A}_{12r} - (\bar{T}_{12r})^{\frac{1}{2}}N_{23r}\bar{A}_{23r})
\end{cases} \tag{4.76}$$

$$\begin{cases} N_{12f} = \dfrac{W_{12f}}{W_{cr}} = \left\{ \dfrac{\left[(\overline{P}_{21f})^{\frac{2}{n}} - (\overline{P}_{21f})^{\frac{n+1}{n}} \right]}{\frac{(n-1)}{2} (\frac{2}{n+1})^{\frac{n+1}{n-1}}} \right\}^{\frac{1}{2}} \\ N_{12r} = \dfrac{W_{12r}}{W_{cr}} = \left\{ \dfrac{\left[(\overline{P}_{21r})^{\frac{2}{n}} - (\overline{P}_{21r})^{\frac{n+1}{n}} \right]}{\frac{(n-1)}{2} (\frac{2}{n+1})^{\frac{n+1}{n-1}}} \right\} \end{cases} \quad 4.77$$

$$\begin{cases} N_{23f} = \dfrac{W_{23f}}{W_{cr}} = \left\{ \dfrac{\left[(\overline{P}_{32f})^{\frac{2}{n}} - (\overline{P}_{32f})^{\frac{n+1}{n}} \right]}{\frac{(n-1)}{2} (\frac{2}{n+1})^{\frac{n+1}{n-1}}} \right\}^{\frac{1}{2}\frac{1}{2}} \\ N_{23r} = \dfrac{W_{23r}}{W_{cr}} = \left\{ \dfrac{\left[(\overline{P}_{32r})^{\frac{2}{n}} - (\overline{P}_{32r})^{\frac{n+1}{n}} \right]}{\frac{(n-1)}{2} (\frac{2}{n+1})^{\frac{n+1}{n-1}}} \right\} \end{cases} \quad 4.78$$

Equations 4.75 to 4.78 comprise the dimensionless mathematical model of the half car model with pneumatic suspension.

The same scaling laws as the quarter car model with pneumatic suspension guarantees the equal Pi-numbers for scaled model and full scale model. Therefore the scaling laws to build a similitude half car model with pneumatic suspension are as follows:

$$\begin{aligned} C_T &= 1 \\ C_{Te} &= 1 \\ C_P &= \frac{C_m}{C_L} \\ C_k &= C_m \\ C_d &= (C_L)^{\frac{3}{2}} \end{aligned} \quad 4.79$$

If the system includes dampers, the scaling law for the damping coefficient is added to these scaling laws. As was explained in Chapter 3 the scaling law of the damper coefficient is as follows:

$$C_B = C_m \tag{4.80}$$

CHAPTER 5
Air spring Parameter Identification

5.1 Introduction

The pneumatic system model of the air spring was developed in Chapter 4, and culminated with an expression of the pressure inside the bellows. In that derivation the force produced by that pressure was calculated based on a fictitious area, called the effective area. The physical system of an air spring is so complex that the area on which the pressure acts cannot be theoretically deduced. This chapter reports on the work carried out to infer the effective area and other salient parameters of the air spring from experimental data. Some fundamental questions are also dealt with in this chapter, these are: a) can a single linear mathematical model represent an air spring with an acceptable error? b) how precisely does the nonlinear mathematical model emulate the behaviour of an air spring? c) how sensitive is the system to model parameter uncertainties? The answers to these questions are necessary for designing a practical and efficient controller. To answer these questions, an experimental setup is designed to carry out some experiments. The effective area is obtained for different air spring pressures and assembly heights. The frequency responses of the real physical model for different pressures and payloads are recorded. The linear mathematical model is identified by using Matlab System Identification Toolbox. The frequency responses of the nonlinear mathematical model and the experimental model are compared, and finally the model sensitivity to the different uncertainties are examined.

5.2 The Experimental Setup

Figure 5.1 shows the designed experimental setup used to obtain the static properties and the frequency response of the air spring. A sine wave generator is used to excite the system. An amplifier with adjustable gain amplifies the excitation signal. The

amplified signals are fed to an electromagnetic vibration exciter (B&K Model #4809). A 2M2A Firestone air spring is mounted on the vibrator.

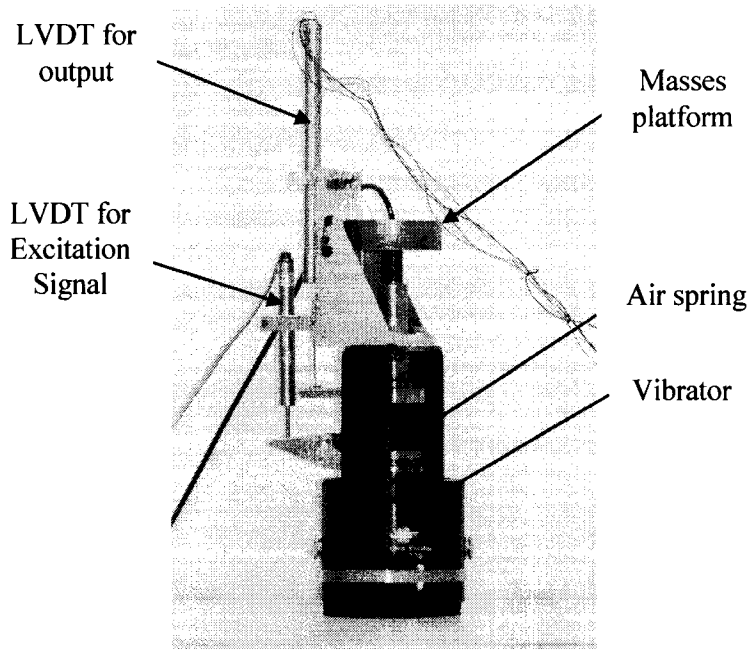

Figure 5.1: The experimental setup for frequency analysis of the air spring

Masses can be added to a platform mounted on the air spring and constrained by linear bushings to move only vertically.

Two LVDT's are used to measure simultaneously the displacement of the air spring piston, the system input, and the sprung mass displacement, the system output. The air spring height and the phase shift between the input and the output of the air spring can be calculated using the signals of the two LVDT's. In addition, the air spring pressure is measured using a pressure transducer. A computerized data acquisition system is used to record the sensory signals.

The calibration process and the equations for all the sensors used are given in Appendix C.

5.3 Static Characteristics of the Air Spring

The first series of experiments is performed to obtain the static properties of the air spring. The air spring assembly height is measured under different payloads and air spring pressures. Table 5.1 lists raw results obtained from that series.

Table 5.1: The assembly height in inches for different payloads and pressures

psig / lbs	5	10	15	20	25	30	35	40
0.816	2.092	2.125	2.153	2.162	2.187	2.195	2.202	2.207
2.13	2.039	2.073	2.107	2.125	2.141	2.149	2.157	2.166
4.13	2.026	2.068	2.095	2.119	2.132	2.162	2.173	2.189
6.13	1.998	2.049	2.075	2.099	2.120	2.145	2.153	2.174
8.13	1.966	2.024	2.057	2.080	2.101	2.130	2.138	2.163
10.13	1.924	1.994	2.032	2.063	2.088	2.116	2.121	2.150
12.13	1.883	1.971	2.009	2.046	2.071	2.100	2.108	2.141
17.13	1.756	1.888	1.954	1.995	2.026	2.061	2.074	2.107
22.13	1.595	1.800	1.908	1.955	1.981	2.022	2.042	2.078
27.13	1.566	1.684	1.858	1.892	1.940	1.987	1.993	2.040
32.13	1.463	1.571	1.772	1.831	1.889	1.937	1.961	2.002
37.13	1.222	1.291	1.659	1.763	1.843	1.898	1.919	1.962
42.13		1.196	1.547	1.684	1.791	1.854	1.872	1.939
47.13		1.144	1.318	1.588	1.739	1.831	1.829	1.896
52.13		1.080	1.262	1.504	1.671	1.822	1.805	1.855
57.13		1.138	1.205	1.305	1.582	1.642	1.717	1.811
62.13				1.253	1.477	1.574	1.663	1.756
67.13				1.218	1.375	1.497	1.604	1.695
72.13				1.164	1.274	1.434	1.550	1.628
77.13					1.202	1.322	1.480	1.587
82.19						1.259	1.419	1.537
84.38						1.193	1.269	1.455
92.51							1.192	1.309

Since the static force developed by the air spring can be viewed as the product of the internal force of pressure and the air spring effective area, then with respect to Table 5.1 the following relationship can be used to infer the effective area:

$$A = \frac{m_s g}{P} \qquad 5.1$$

The effective areas corresponding to different air spring heights and pressures are calculated and tabulated in Table 5.2. The mean cross section area A_{mean} is also approximated and provided in Table 5.2 for different pressures And payloads. The mean cross sectional area is calculated based on measurement of the air spring height and using Equation 4.26.

Table 5.2: The static effective area for different pressures and assembly heights

in	Psig	5	10	15	20	25	30	35	40
1.2	A	6.863	4.192	3.837	3.440	3.091	2.805	2.619	2.465
	A_{mean}		2.956		3.161		3.405		3.418
1.4	A	6.530	3.518	3.022	2.737	2.636	2.455	2.356	2.186
	A_{mean}		2.956		3.161		3.248		3.261
1.6	A	4.395	3.084	2.651	2.325	2.245	2.007	1.929	1.889
	A_{mean}		2.986		3.123		3.161		3.243
1.8	A	3.079	2.213	2.033	1.720	1.651	1.758	1.497	1.453
	A_{mean}		3.161		3.243		2.901		3.029
2	A	1.197	0.973	0.863	0.832	0.801	0.838	0.755	0.809
	A_{mean}								
2.1	A	0.103	0.164	0.220	0.301	0.331	0.404	0.380	0.458
	A_{mean}								
2.15	A	-0.272	0.0863	0.060	0.0621	0.075	0.185	0.187	0.253
	A_{mean}								
2.2	A	-0.649	-0.102	-0.026	-0.027	0.018	.022	0.023	0.053
	A_{mean}								

The negative effective area implies that a negative force is required to cause the air spring to reach that specific assembly height.

The data in Table 5.2 are plotted in Figures 5.2 and 5.3. Figure 5.3 shows anomalous behaviour of the system at pressures below 10 psig. This is primarily due to the dominance of the bellows material and structure compliance and the friction in the linear bushing over the force of pressure.

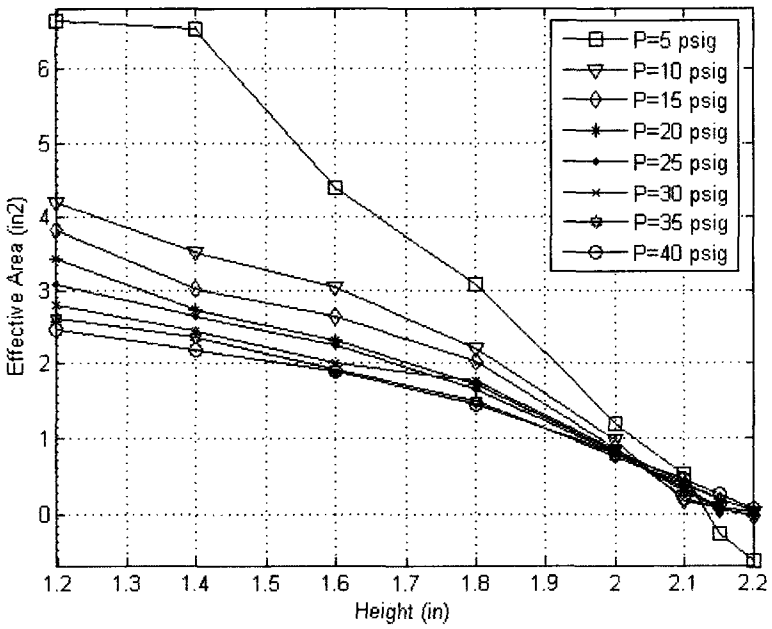

Figure 5.2: Air spring effective area vs. pressure and air spring height

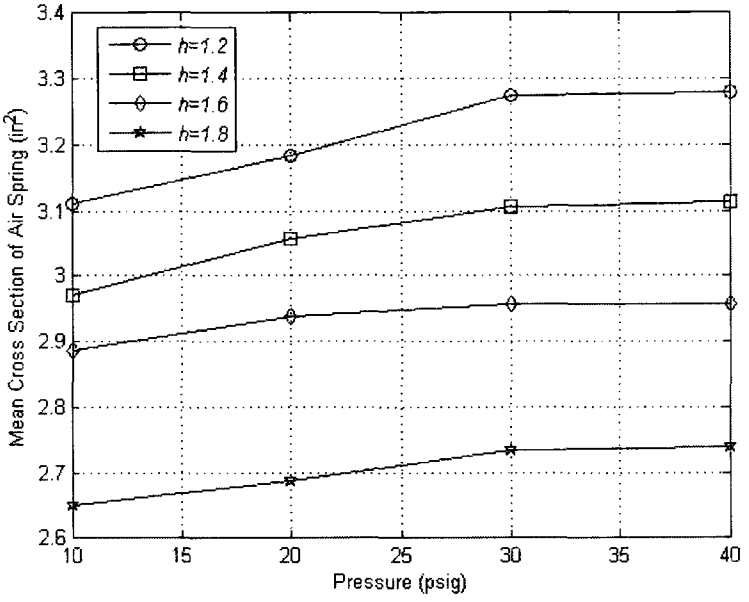

Figure 5.3: Air spring mean cross section area vs. pressure and height

Figures 5.2 and 5.3 also show that for a given height as the pressure increases the air spring bulges and its mean cross section area increases while the effective area decreases.

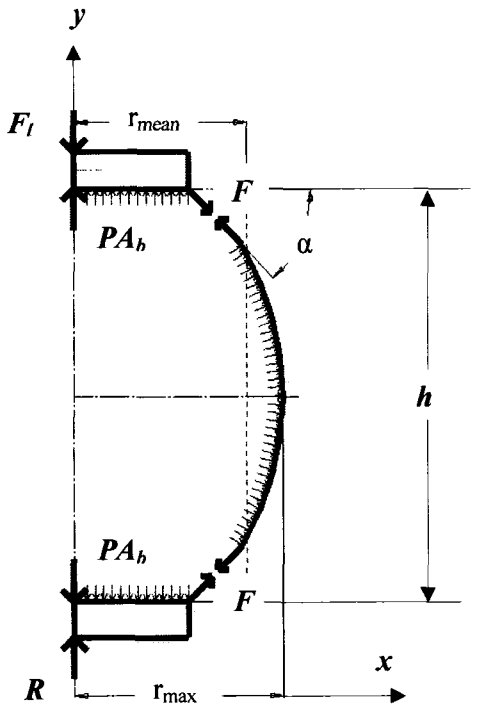

Figure 5.4: Pressure distribution on the bellows

Figure 5.4 shows a cross section of the bellows and the forces acting on it from the upper bead plates and the pressurized air inside the air spring. The force applied to the bellows by the upper bead plate is denoted by F which makes an angle α with the horizontal axes. The air spring area can be approximated by a cylinder with a radius equal to r_{mean}. Considering a strip of the bellows with a thickness of ds, the force balance on the strip in the x direction gives:

$$2dF\cos(\alpha) = Phds \tag{5.2}$$

Integrating both sides of Equation 5.2 on the surface of the bellows yields:

$$2F\cos(\alpha) = (2\pi r_{mean}h)P \tag{5.3}$$

The y-component of the force F is given by:

$$F_y = (\pi r_{mean}h)P\tan(\alpha) \tag{5.4}$$

A force equal to F_y but in the opposite direction is applied to the upper bead plate by the bellows. On the other hand, experiments show that at 0 psig, the bellows can support F_0=8 lbs. Therefore, the force balance on the bead in the y direction is as follows:

$$F_l = PA_p - F_y + F_0 \qquad 5.5$$

Substituting for F_y in Equation 5.5 and rearranging gives:

$$A = (A_p - \pi r_{mean} h \tan(\alpha) + \frac{F_0}{P}) \qquad 5.6$$

where A_p is the effective projected area on plane yz.

If the bellows material is rigid then A_p would be the full projection area on the yz plane. However since the bellows material is a bias-ply elastomeric composite, A_p is smaller that that of the case of rigid material. A good approximation of A_p in the current case is the mean cross section area. Substituting A_p by A_{mean} in Equation 5.6 gives the theoretical effective area as follows:

$$A = A_{mean} - \pi r_{mean} h \tan(\alpha) + \frac{F_b}{P} \qquad 5.7$$

As Figure 5.3 shows, for a constant height, the mean cross section area and consequently the mean radius increase slightly. Moreover, the effects of these two variables on Equation 5.7 compensate each other partially. Increasing the pressure increases α. Thus the second term in Equation 5.3 increases and the third element decreases, causing an overall decrease in the effective area and consequently a decrease in the load carrying capacity.

All the parameters of Equation 5.7 are known with the exception of angle α. Substituting for A_{mean} and A from Table 5.2 into Equation 5.3, α can be calculated. Table 5.3 shows α for different pressures and heights

Table 5.3: The angle α in degrees for different pressures and assembly heights

psig / in	10	20	30	40
1.2	0	3.5	7	13.5
1.4	3.5	9.5	12	14.5
1.6	7	12	14	14.5
1.8	13.5	14	14	15.5

It should be noted that the above discussion is an approximate explanation of the behaviour and parametric interplay of the air spring effective area. In reality the effective area of an air spring is far too complicated and beyond the scope of this work.

5.4 Frequency Analysis

Frequency response is used to identify linear mathematical models, and compare the behaviour of the air spring with the nonlinear mathematical model. The frequency response is chosen because of the depth of information that can be gleaned from a single experimental run response. A frequency response curve entails obtaining the system responses due to a wide range of sinusoidal inputs, hence the results obtained from such an analysis are more reliable than those obtained from the analysis of a single periodical or aperiodical signal.

The frequency response curves for the air spring/load system were obtained for different pressure/payload combinations. 24 sinusoidal signals with frequencies varying between 0.5 Hz and 18 Hz were used. The air spring input and output responses were measured via the LVDT's and are recorded by the data acquisition system. The experiments are repeated for five different pressures between 5 psig and 25 psig in increments of 5 psi, and for 4 different payloads between 4 lbs and 10 lbs in increments of 2 lbs. For each experiment, the input and the output frequency, amplitude, and phase shift information are extracted and the Bode diagrams plotted.

Figures 5.7 to 5.10 show these Bode diagrams. The magnitude curves at different pressures and loads have similar shapes. The curves have one major maximum that occurs at a frequency that changes with the payload and the air spring pressure. These peaks correspond to the natural frequency of the system at these conditions, and the curves show that as the air spring pressure increases, the natural frequency increases. The curves also show that the natural frequency decreases as the payload increases. A second peak with a smaller magnitude can be seen on some curves and seem to have a frequency that is independent of the payload and air spring pressure. This resonance

seems to be the result of the bellows composite material folding and unfolding behaviour.

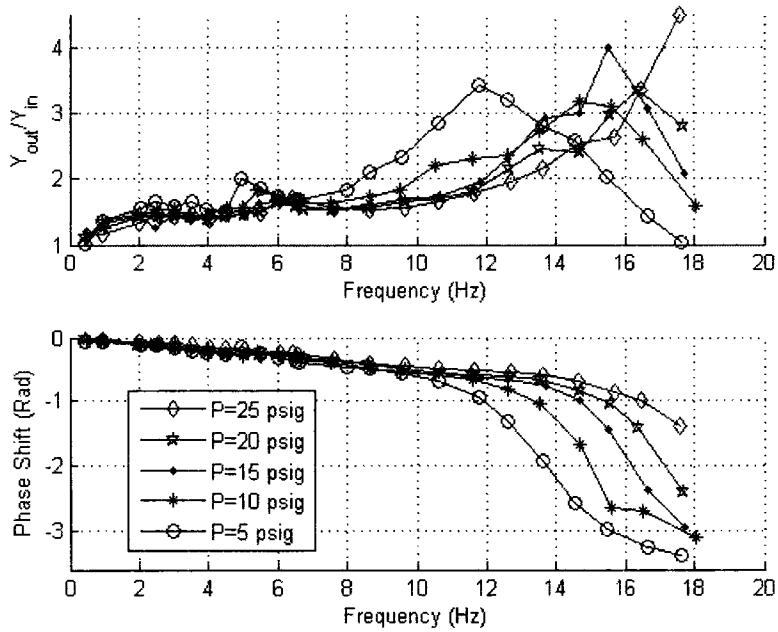

Figure 5.7: The frequency response of the air spring under a 4lb payload

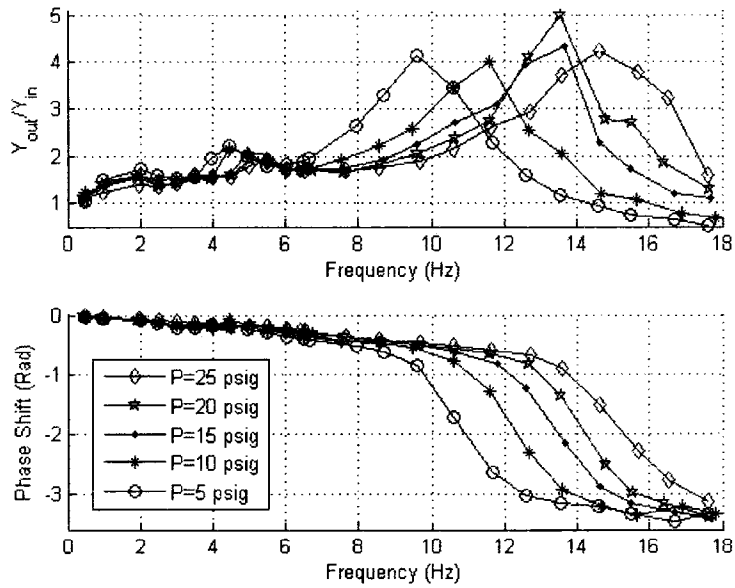

Figure 5.8: The frequency response of the air spring under a 6lb payload

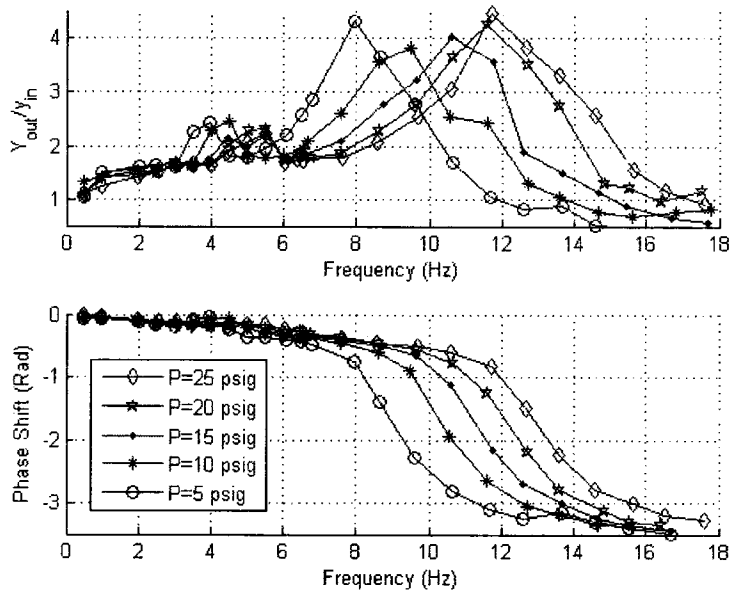

Figure 5.9: The frequency response of the air spring under 8lbs weight

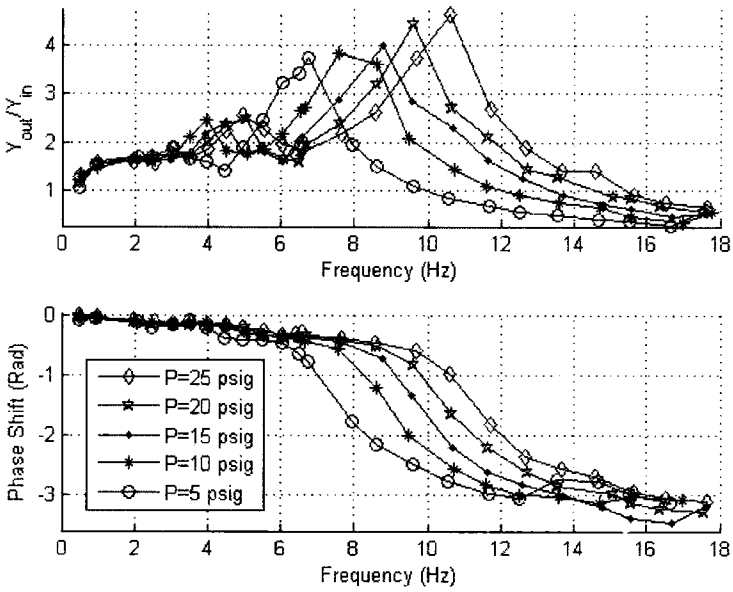

Figure 5.10: The frequency response of the air spring under a 10lb payload

The phase plots in Figures 5.7 to 5.10 show a remarkably similar trend. The curves seem to indicate that the behaviour of the system is that of a second order one with a zero phase shift at very small frequencies and a phase shift of π at very large ones.

5.5 System Identification

Quaglia and Sorli (2001) showed that the linearized transfer function of an air spring around an equilibrium point is of order two [34]. Figures 5.7 to 5.10 illustrate that the air spring behaviour around an equilibrium point is similar to a second order system, if the bellows second resonance peak can be ignored. The ultimate goal of this analysis is to derive a reliable mathematical model of the air spring. The second resonance peak produced by the bellows folding behaviour is independent of payload and the air spring pressure, and has a very small magnitude; therefore, will be ignored to simplify the analysis. In order to determine whether a unique second order transfer function can represent the air spring under different payloads and pressures with an acceptable error, the transfer function corresponding to each pair of payload and pressure is identified. Twenty transfer functions are obtained for the twenty pairs of payloads and pressures, then the natural frequency and damping ratio of each transfer function is calculated. Table 5.4 presents the natural frequencies for different pairs of load and pressure.

Table 5.4: The natural frequency (Hz) for different payloads and pressures

	W=4 lbs	**W=6 lbs**	**W=8 lbs**	**W=10lbs**
P=5 psig	13.50	10.44	8.62	7.28
P=10 psig	15.26	11.97	9.83	8.76
P=15 psig	16.33	13.40	11.27	9.62
P=20 psig	17.22	14.1226	12.05	10.20
P=25 psig	19.00	15.24	12.88	11.10

Figure 5.11 shows a plot of the information in Table 5.4. The plots show clearly that the natural frequency increases as the pressure increases. That is because a higher pressure results in a stiffer air spring, and consequently an increase in the natural frequency. As the pressure changes from 5 psig to 25 psig, the natural frequency shifts up 4 Hz at 10lbs payload and 6 Hz at 4lbs payload. However, for a specific pressure, the natural frequency decreases as the payload increases. These results correspond to what is expected from a second order system.

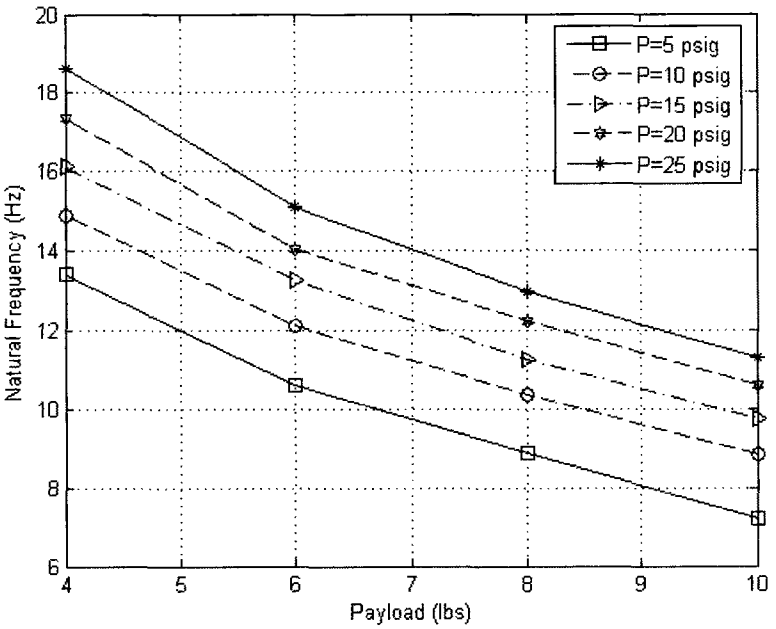

Figure 5.11 Natural frequency curves for different loads and pressures

The damping ratios for the pairs of loads and pressures are presented in Table 5.5.

Table 5.5 The damping ratios for different loads and pressures

	W=4 lbs	**W=6 lbs**	**W=8 lbs**	**W=10 lbs**
P=5 psig	0.137	0.124	0.141	0.134
P=10 psig	0.129	0.121	0.128	0.130
P=15 psig	0.104	0.108	0.119	0.123
P=20 psig	0.086	0.092	0.113	0.112
P=25 psig	0.063	0.089	0.100	0.102

Figure 5.12 shows the plot of the data in Table 5.5. The figure shows that as the pressure increases, the damping ratio decreases. This can be explained by the fact that a larger pressure results in a stiffer air spring. An increase in the air spring stiffness increases the critical damping and consequently decreases the damping ratio of the system. The damping ratio remains always in the range of 0.06 to 0.14.

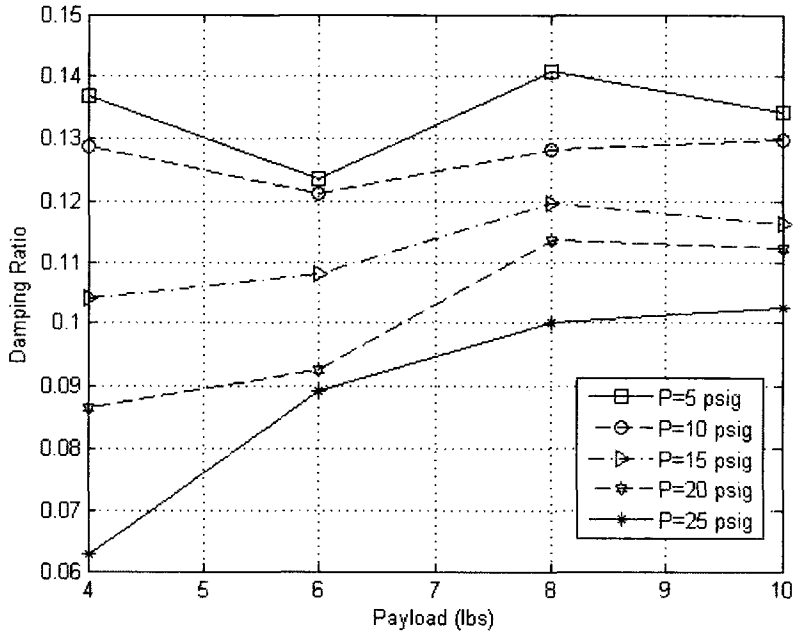

Figure 5.12 The damping ratio for different loads and pressures

The Firestone technical catalogue suggests a zero damping ratio for air springs [44]. The presence of a damping ratio here can be attributed to the friction introduced into the system by the linear bushing. Even though the change in damping ratio can be ignored, the change in the natural frequency cannot be ignored. The natural frequency curves show an 11 Hz change over the entire range of pressure and payload. Therefore, if a single second order transfer function is used to represent the air spring, a considerable error will be introduced. Moreover, a 4 to 6 Hz change in the natural frequency for a specific payload shows that even a quasilinear model cannot accurately represent the air spring. Thus, a nonlinear model seems to be necessary for such a system.

5.6 Comparison between Theoretical and Experimental Results

The mathematical model of the air spring derived in Section 4.2 is valid for this system; however, the linear bushing mechanism adds friction to the system and must be accounted for in the model. Denoting the overall damping coefficient of the system by "*c*", Equation 4.23 becomes:

$$m_s\ddot{Z}_s + m_s g + c^*(\dot{Z}_s - \dot{Z}_r) = P_2 A \qquad 5.8$$

Using this mathematical model, the frequency responses for different pressures and payloads were obtained. Table 5.2 is used as a lookup table to update the effective area based on the air spring pressure and height. These frequency responses are compared to those of the experimental runs.

Figures 5.13 to 5.16 compare the theoretical and experimental frequency responses. The thermodynamic process is assumed to be isentropic, n=1.4.

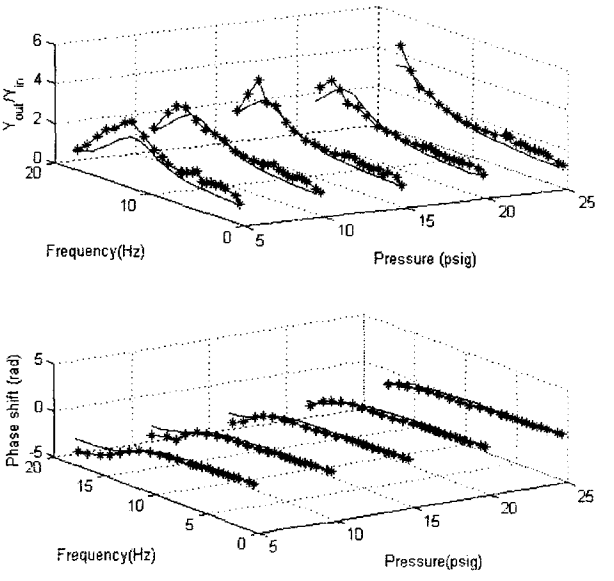

Figure 5.13: Theoretical and experimental frequency responses for a 4lb payload

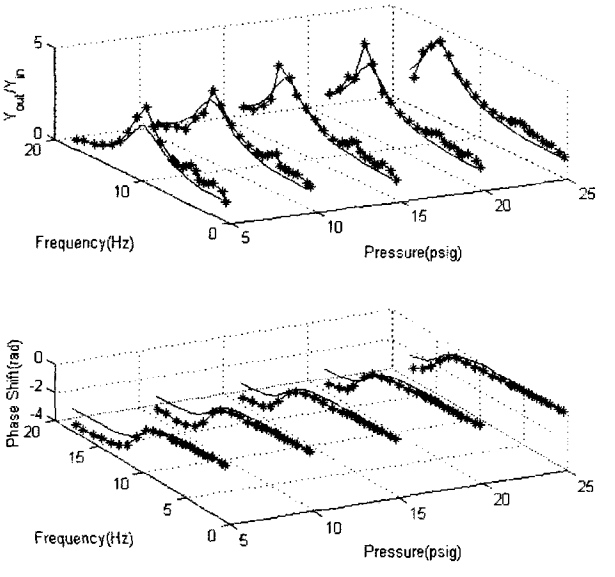

Figure 5.14: Theoretical and experimental frequency responses for a 6lb payload

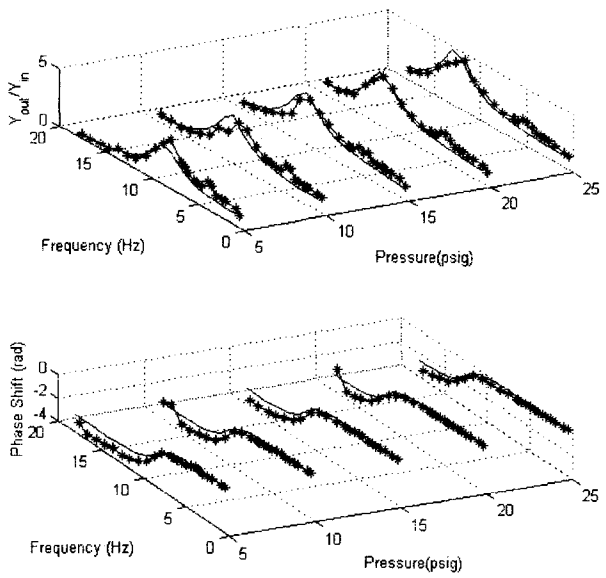

Figure 5.15: Theoretical and experimental frequency responses for a 8lb payload

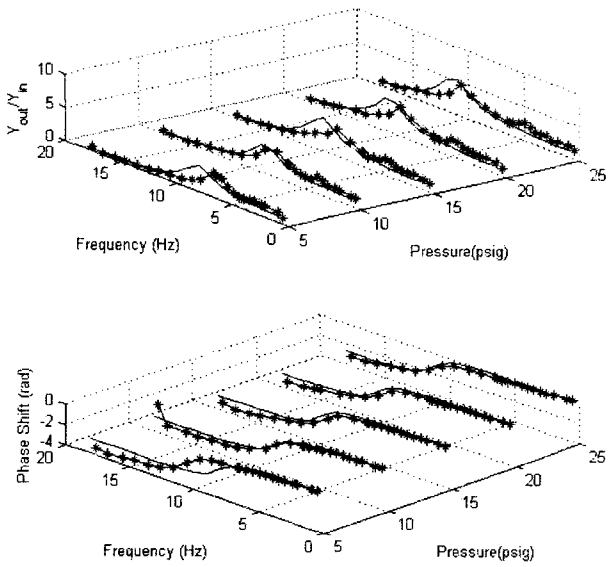

Figure 5.16: Theoretical and experimental frequency responses for a 10lb payload

These figures show a good agreement between the experimental and theoretical results. Since the bellows unfolding behaviour was not simulated, there is just one resonance peak in the theoretical frequency response. The two curves are very close at low frequencies. A shift exists around the natural frequency in some curves. At high

frequencies, because of small amplitude, the effects of the bellows diminish and the two curves converge.

The difference between the two curves around the air spring natural frequency can be explained by the uncertainties in the mathematical model, such as the thermodynamic process, unmodeled bellows unfolding behaviour, the errors in the air spring effective area and volume. The figures imply that the nonlinear mathematical model can represent the behaviour of an air spring for different pressures.

5.7 The sensitivity of the Air spring Dynamics to the Model Uncertainties

The air spring effective area is one of the major sources of imprecision in the air spring mathematical model. To examine the model sensitivity to the effective area uncertainty, two different look-up tables for effective area are established by shifting up and down 10 percent all elements of the effective area look up table. Figure 5.17 compares the air spring frequency responses of the two different look up tables with that of the original one. Initial pressure, payload and the input amplitude are 25 psig, 10 lbs and 0.1 inch, respectively.

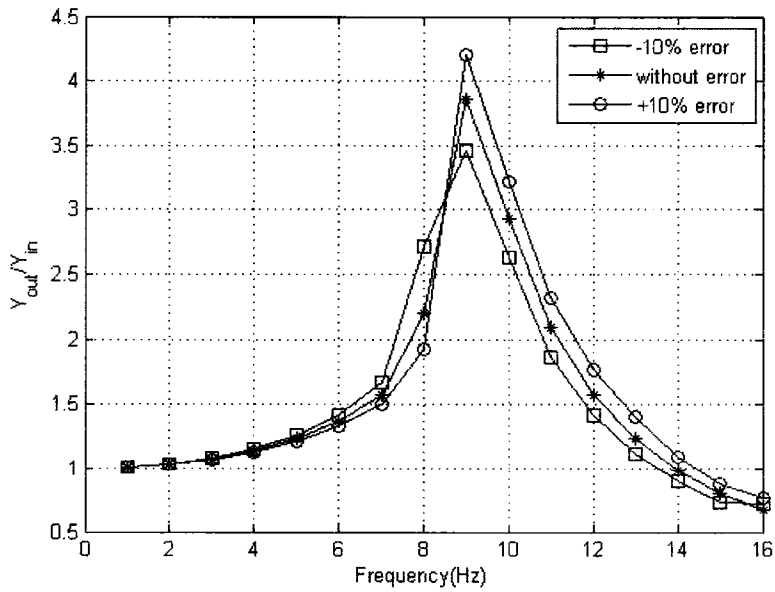

Figure 5.17 Frequency responses of the air spring with two different effective area look up tables when $Y_{in} = 0.1$ inch

At low frequencies where usually a vehicle works, the difference is small, but as the frequency increases, the system becomes more sensitive to effective area errors.

In order to show the effect of the excitation amplitude on the system response, the input amplitude decrease to 0.05in and the frequency responses are obtained with the same payload and initial pressure. Figure 5.18 compares the frequency responses for the three look up tables when the input amplitude is 0.05 inch.

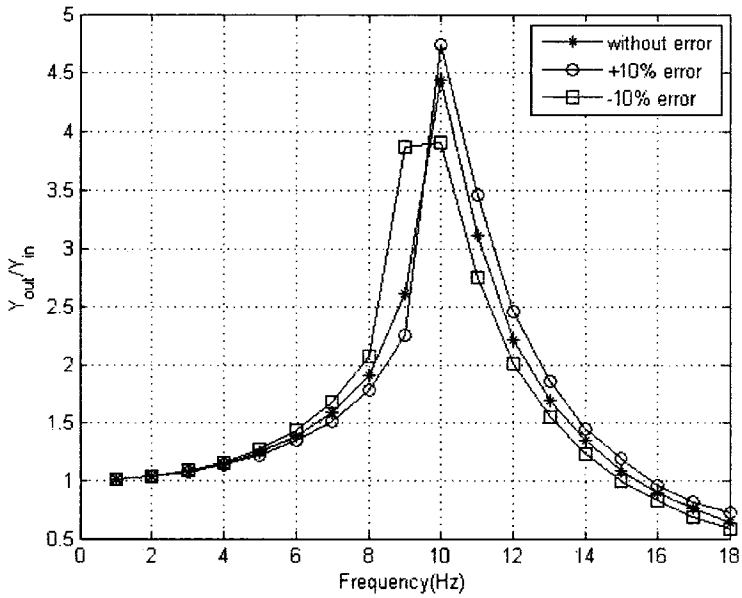

Figure 5.18 Comparing the air spring frequency responses of different effective area look up tables when $Y_{in} = 0.05$ in

The natural frequency increases from 9.5Hz to 10Hz, when the input amplitude decreases from 0.1in to 0.05in. The air spring height changes by the input amplitude. According to Table 5.2, the effective area is a function of the air spring height. Therefore, the effective area changes by the input amplitude. The effect of the effective area on the natural frequency can be explained by its effect on the air spring stiffness. The stiffness of the air spring K_A is defined by:

$$K_A = \frac{dF_l}{dh} \tag{5.9}$$

where F_l is the force exerted to the payload by the air spring and is given by Equation 5.5. Substituting for F_l from Equation 5.5 and taking derivative with respect to h gives:

$$K_A = \frac{dP}{dh} A_p + P\frac{dA_p}{dh} - \frac{dF_y}{dh} \qquad 5.10$$

Equation 5.10 shows that the stiffness of the air spring is a function of effective area. Therefore as the effective area changes by the input amplitude, the stiffness and consequently the natural frequency of the air spring change.

The thermodynamic process is another source of uncertainty. The frequency responses of the isothermal and isentropic processes are compared with that of the experimental one in Figure 5.19. Payload, the input amplitude and the initial air spring pressure are 10 lbs, 0.05 inch and 25 psig respectively. As the figure shows, the difference between the isothermal and isentropic curve is small at low frequencies but this difference increases around the natural frequency.

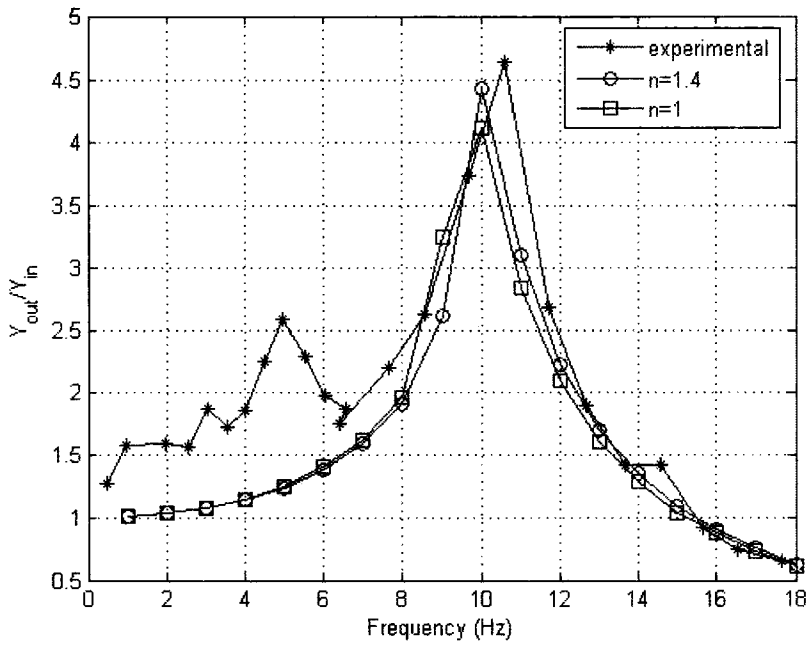

Figure 5.19 Comparing the isentropic and isothermal frequency response

Comparing the difference between the curves of two different processes in Figure 5.19 with that of the two modified look up tables either in Figure 5.17 or 5.19 proves that the model sensitivity to the thermodynamic process is smaller than that of the effective area. The model sensitivity to the thermodynamic process for total range of n is small and can be ignored. But the uncertainty of effective area cannot be ignored and should be considered when the mathematical model is used to analyze or control an air spring.

CHAPTER 6

Nonlinear Control of Quarter and Half Car Models with Pneumatic Suspension

6.1 Introduction

The conflict between ride comfort, handling and load variation also exist in pneumatic suspensions. Similar to conventional suspensions, control techniques are used to deal with this problem. Active and semi-active pneumatic suspensions are used to improve the performances of pneumatic suspensions. Unlike conventional suspensions, the mathematical models of pneumatic suspensions are highly nonlinear. Analyses in Chapter 5 show that these models are also not precise. In addition to the uncertainties that are introduced by the simplification assumptions, difficulties in measuring the air spring volume and effective area on-line introduce another set of uncertainties. Therefore, classical controllers cannot control pneumatic suspensions efficiently. In order to control such a nonlinear system with an imprecise model, the controller should be robust against uncertainties and be able to compensate for the inherent nonlinearities. The feedback linearization technique can deal with nonlinearity in a nonlinear system, but they are not robust against model uncertainties. Robust control techniques that can deal with such uncertainties include sliding mode and adaptive controllers. Feedback linearization technique in conjunction to the sliding mode and adaptive controller would be able to remove the nonlinearity and deal with different uncertainties.

In this chapter, feedback linearization, model reference, sliding mode and sliding mode controller with parameter estimator are applied to a quarter car model with pneumatic suspension. The sensitivities of these controllers to model uncertainties are studied. Finally the controller with the best performance is applied to the half car model.

6.2 Simulation of a Road Profile

To evaluate the performance of a suspension, a realistic simulation of the road profile is required. The profile of the road roughness can be represented by a Gaussian random signal. The power spectral densities (PSDs) of roads with different roughness have been introduced by the International Organization for Standardization (ISO) [10]. The one-sided spatial PSDs $G(\Omega)$ of roads with different degrees of roughness are formulated as follows:

$$G(\Omega) = G(\Omega_0)(\frac{\Omega}{\Omega_0})^{-N} \qquad 6.1$$

where Ω denotes the spatial frequency, and $G(\Omega_0)$ is the one-sided PSD of the road in m^3/cycles at Ω_0=1 rad/m. $G(\Omega_0)$ takes different values for different degrees of roughness. N is equal to 2 for $\Omega \leq \Omega_0$, and equal to 1.5 for $\Omega > \Omega_0$. Table 6.1 shows the values of $G(\Omega_0)$ for different degrees of roughness [49].

Table 6.1: Classification of road roughness proposed by ISO

Road Class	Range of $G(\Omega_0)$ 10^{-6} m^3/cycles	Mean of $G(\Omega_0)$ 10^{-6} m^3/cycles
A(Very Good)	<8	4
(B)Good	8-32	16
C(Average)	32-128	64
D(Poor)	128-512	256
E(Very Poor)	512-2048	1024
F	2048-8192	4096
G	8192-32768	16384
H	>32768	

The relationship between the power spectral density and the one-sided power spectral density is as follows:

$$G(\Omega) = 2S(\Omega) \qquad 6.2$$

Assuming that the vehicle is moving at a speed of V m/s, the temporal power spectral density can be calculated from the spatial power spectral density by the following equation:

$$G(f) = \frac{G(\Omega)}{V} \tag{6.3}$$

where f is the temporal frequency in Hz.

Substituting from Equation 6.1 into Equation 6.3 gives:

$$G(f) = \frac{G(\Omega_0)(\frac{\Omega}{\Omega_0})^{-N}}{V}$$

Dividing $G(f)$ which is in m^3/cycle by 2π, gives the temporal one-sided PSD of a road roughness $G(w)$ in m^3/rad as follows:

$$G(w) = \frac{\frac{G(\Omega_0)}{2\pi}(\frac{\Omega}{\Omega_0})^{-N}}{V} \tag{6.4}$$

where w is the temporal angular frequency in rad/s . The road profile unevenness can be simulated using the one-sided temporal PSD by taking the inverse Fourier Transform as follows:

$$u(t) = \sum_{k=1}^{N} A_k \cos(w_k t + \Phi_k) \tag{6.5}$$

where w_k is the discrete frequency and Φ_k is an independent random phase angle in the range of $[0, 2\pi]$. The amplitude A_k in Equation 6.5 can be calculated from the spatial PSD as follows:

$$A_k(k) = \sqrt{2 * G(w) * \Delta w} \tag{6.6}$$

where Δw is the sampling discrete frequency [50].

A poor road, which corresponds to the ISO class D road, is chosen for this research. It is assumed that a vehicle is travelling on this road at 80 km/h. Using the information in Table 6.1 and Equations 6.4 to 6.6, the road profile is simulated. Figure 6.1 shows the full scale road profile for 10 seconds.

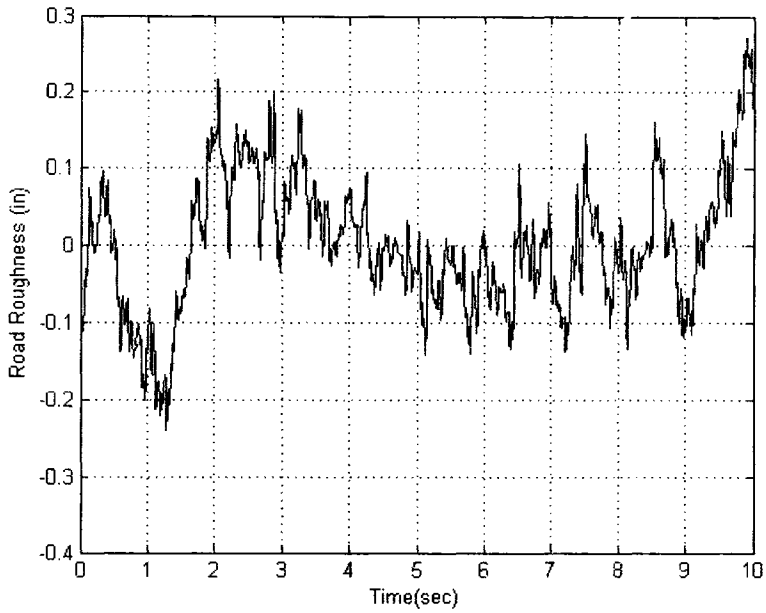

Figure 6.1: The D class road unevenness profile

Since the road profile will be used to study the behaviour of the scaled model of the Honda Civic, this profile should be scaled as well. The scaled road profile can be calculated either by substituting the scaled power density and scaled velocity in Equations 6.4 to 6.6, or by scaling down the full scale road profile by the scale factor of length. Figure 6.2 shows the scaled road profile.

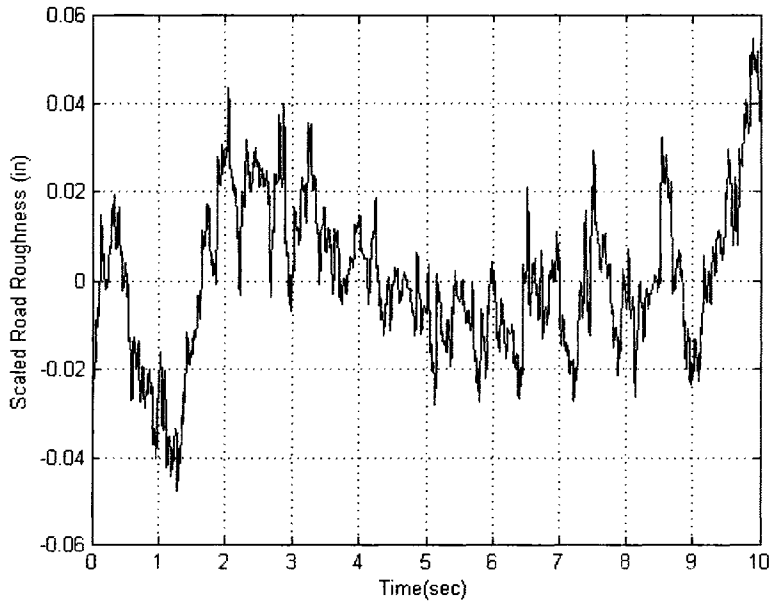

Figure 6.2: The D class scaled road unevenness profile

In a half car model, the rear wheel passes over the same profile as the front one after a time delay t_d equal to $\frac{V}{a+b}$ where V is the vehicle. In this study, for a scaled half car model, the front road profile is considered as shown in Figure 6.2, and the rear profile passes over the same profile after $t_d = 8.75$ seconds.

6.3 Feedback Linearization Control (FLC) of a Quarter Car Model with Pneumatic suspension

The idea of feedback linearization technique is to eliminate the nonlinearity of the system model first, and then inject the desired linear dynamic. To obtain the control input, the output of the system is differentiated again and again until the input appears in one of the derivatives. If the input appears in the k^{th} derivative, then the k^{th} derivative can be written as follows:

$$y^{(k)} = f(X) + b(X)u \tag{6.7}$$

where u and X are the input and the state vector of the system, respectively. Solving Equation 6.7 for u gives:

$$u = \frac{1}{b(X)}[y^{(k)} - f(X)] \tag{6.8}$$

where $b(X) \neq 0$. In the absence of the model uncertainty, if the control input is chosen as Equation 6.8, the nonlinearity will be eliminated. In order to obtain the desired dynamics, the control input is defined as follows:

$$u_c = \frac{1}{b(X)}[v - f(X)] \tag{6.9}$$

where v is the summation of the power products of the different output derivatives as:

$$v = -K_0(y - r) - K_1\dot{y} - \cdots K_{r-1}y^{(k-1)} \tag{6.10}$$

In Equation 6.10, r is the desired reference input and K_i is the control gain corresponding to i^{th} derivative of the output. If the control command is fed into the system, substituting Equation 6.9 into Equation 6.7, the nonlinearity is removed and the dynamic of the output is given by:

$$y^{(k)} + K_{k-1}y^{(k-1)} + \cdots + K_0 y = K_0 r \tag{6.11}$$

Taking the Laplace transform from both sides of Equation 6.11, the transfer function of the system is given as follows:

$$\frac{Y(s)}{R(s)} = \frac{K_0}{s^k + K_{k-1}s^{k-1} + \cdots + K_0} \tag{6.12}$$

In the case of an imprecise model, the model uncertainty appears as a disturbance in Equation 6.11. When a precise model is available, any desired output response can be achieved by choosing the proper gains.

In order to apply feedback linearization control to the quarter model with pneumatic suspension, the inlet orifice area and the sprung mass displacement are considered as the input and the output of the system respectively. To avoid complexity, the outlet orifice area is assumed to be constant. The mathematical model of the quarter car model with pneumatic suspension was derived in Section 4.4. Taking derivative with respect to time from Equation 4.53 and substituting for $\dot{P}_2$ from Equation 4.22, the inlet orifice area appears in the third derivative of the sprung mass displacement as follows:

$$\dddot{y} = \dot{P}_2 A = -\frac{1}{m_s}\frac{nP_2A}{V_2}\frac{dV_2}{dt} + \frac{nAKRP_2\sqrt{T_1}}{m_sV_2}\left[\frac{T_2}{T_1}(C_{12})A_{12} - \left(\frac{T_2}{T_1}\right)^{\frac{1}{2}}A_{23}N_{23}\right] \tag{6.13}$$

The derivative of the effective area is assumed to be zero. In fact, the time derivative of the effective area is not zero, and this assumption introduces another uncertainty into the model. Solving Equation 6.13 for the input gives:

$$A_{12} = \left[\frac{nKRAP_2\sqrt{T_1}}{m_sV_2}\frac{T_2}{T_1}C_{12}\right]^{-1}\left\{\dddot{y} + \frac{nAP_2}{m_sV_2}\frac{dV_2}{dt} + \frac{nAKRP_2\sqrt{T_1}}{m_sV_2}\left(\frac{T_2}{T_1}\right)^{\frac{1}{2}}A_{23}N_{23}\right\} \tag{6.14}$$

Equation 6.14 can be put in the form of Equation 6.9 as follows:

$$u_c = b^{-1}(X)\{v - f(X)\} \tag{6.15}$$

where

$$f(X) = -\frac{nP_2A}{m_sV_2}\frac{dV_2}{dt} - \frac{nAKRP_2\sqrt{T_1}}{m_sV_2}\left(\frac{T_2}{T_1}\right)^{\frac{1}{2}}A_{23}N_{23} \tag{6.16}$$

$$b(X) = \frac{nAKR\sqrt{T_1}}{m_sV_2}\frac{T_2}{T_1}C_{12} \tag{6.17}$$

$$v = K_a(\ddot{r} - \ddot{y}) + K_v(\dot{r} - \dot{y}) + K_p(r - y) \tag{6.18}$$

where X ,K_a ,K_v and K_p are the state vector of the system, acceleration gain, velocity gain and proportional gain respectively. Assuming a constant reference input, Equation 6.18 becomes:

$$v = -K_a\ddot{y} - K_v\dot{y} + K_p(r - y) \tag{6.19}$$

Substituting u_c from Equation 6.15 for A_{12} in Equation 6.13 and taking Laplace Transform gives the transfer function of the system in the absence of uncertainties as follows:

$$\frac{Y(s)}{R(s)} = \frac{K_p}{s^3 + K_a s^2 + K_v s + K_p} \tag{6.20}$$

To simplify the expression of the gain values, in this study, the gains are chosen so that Equation 6.20 has a triple pole. The magnitude of the triple pole is an indicator of the gain values. For example, the triple pole equal to λ means that the transfer function shown by Equation 6.20 has a denominator equal to $(s + \lambda)^3$; therefore the gains of the controller are as follows:

$$\begin{aligned} K_a &= 3 * \lambda \\ K_v &= 3 * \lambda^2 \\ K_p &= \lambda^3 \end{aligned} \tag{6.21}$$

The feedback linearization of the quarter car model is simulated in Matlab/Simulink. The block diagram is shown in Figure 6.3.

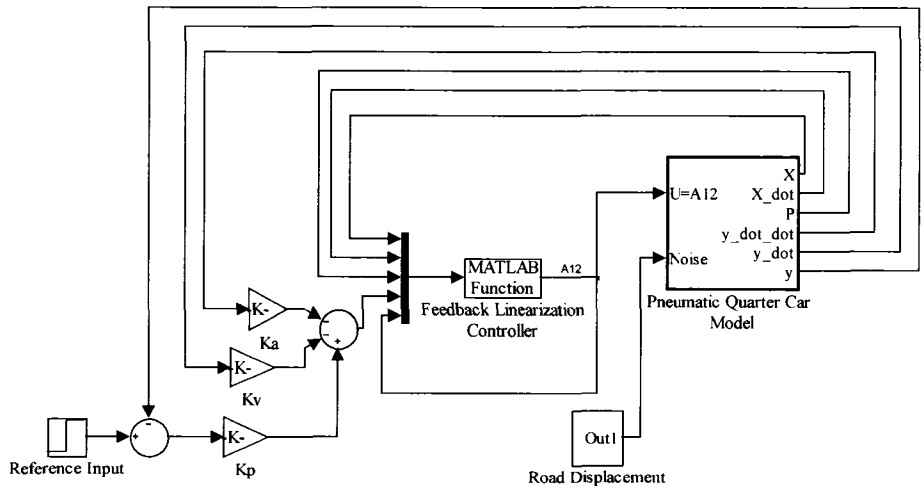

Figure 6.3: The block diagram of the FLC applied to the quarter car model with pneumatic suspension

The designed controller is applied to the scaled quarter car model with pneumatic cylinder which has a constant effective area equal to 5 in^2. The road is assumed to be an ISO class

D road, which is explained in Section 6.2. In the controller, the effective area is estimated by a constant area in the interval of 1 in^2 to 5 in^2. The supply pressure for all controllers in this research is considered 100 psig unless it is specified otherwise. Response of the system for different triple poles λ and different estimated effective areas are obtained. The root mean square (RMS) values of the sprung mass acceleration for each response are calculated. Calculated RMS's are based on system responses after 3 seconds, when the controller is adjusted. RMS's are multiplied by the scale factor to obtain RMS's corresponding to the full scale model. Figure 6.4 shows the sensitivity curves of FLC for a full scale quarter car model with pneumatic cylinder.

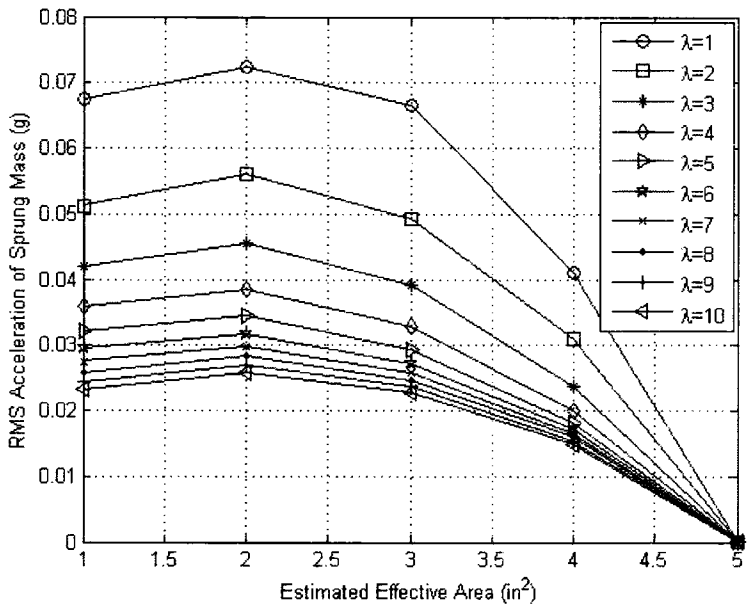

Figure 6.4: Sensitivity curves of FLC applied to a pneumatic cylinder based on RMS acceleration

The mean personal ratings (MPR) based on the Smith's equation, Equation 2.1, are calculated. Figure 6.5 shows the sensitivity curves based on MPR. Results show that MPR's for the gains correspond to triple poles larger than 5 and the estimation errors smaller than 1.5 in^2 are larger than 4, indicating a good ride comfort. When there is no uncertainty (A=5 in^2) the ride comfort is perfect and MPR reaches its maximum possible value.

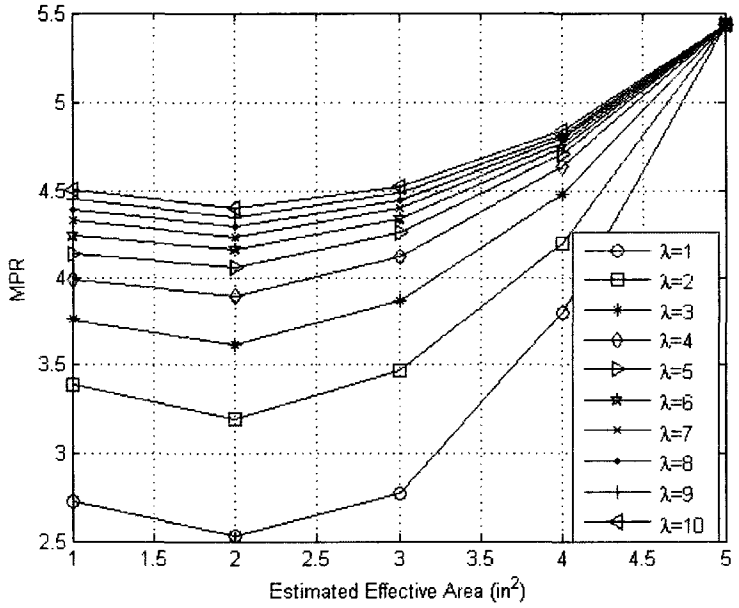

Figure 6.5: Sensitivity curves of FLC applied to a pneumatic cylinder based on MPR

As was discussed in Chapter 5, the effective area of an air spring is not constant. Therefore the behaviour of an air spring is different from a pneumatic cylinder. The designed controller is applied to the quarter car model with an air spring, on an ISO class D road. The effective area of the air spring is estimated by a constant area in the controller. The RMS's acceleration of the sprung mass, for different sets of gains and different estimated effective areas, are calculated and shown in Figure 6.6.

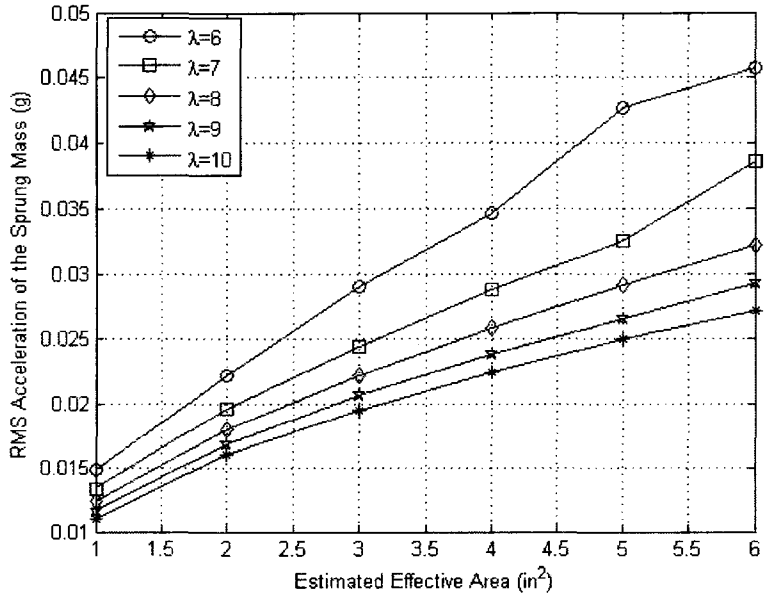

Figure 6.6: Sensitivity curves of FLC applied to the quarter car model based on RMS acceleration of the sprung mass

RMS's are calculated based on the responses after 3 sec when the controller is adjusted. MPR values are also calculated and Figure 6.7 shows the sensitivity curves based on these values. The MPR values corresponding to λ larger than 6 are found to be between 4 and 5, implying a good ride comfort in the presence of effective area uncertainty. As the gain increases, MPR increases and the ride comfort of the suspension improves.

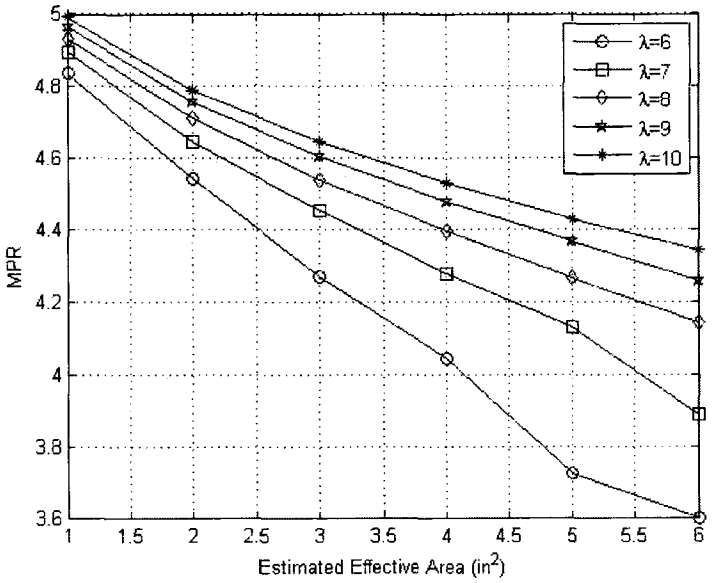

Figure 6.7: Sensitivity curves of FLC applied to the quarter car model Based on MPR

Figure 6.8 shows the air spring effective area for two different sets of gains and two different estimated effective areas.

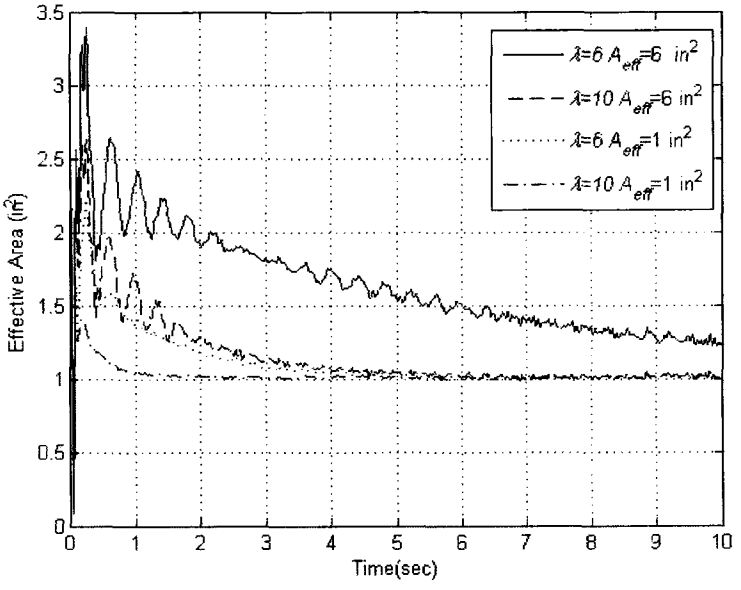

Figure 6.8: The effective area of the air spring for different gains and different estimated effective areas

When the estimated error is small the effective area converges to its final value sooner. Figure 6.8 also implies that in the presence of effective area uncertainty, the time derivative of the effective area is not small and appears as a major source of uncertainty.

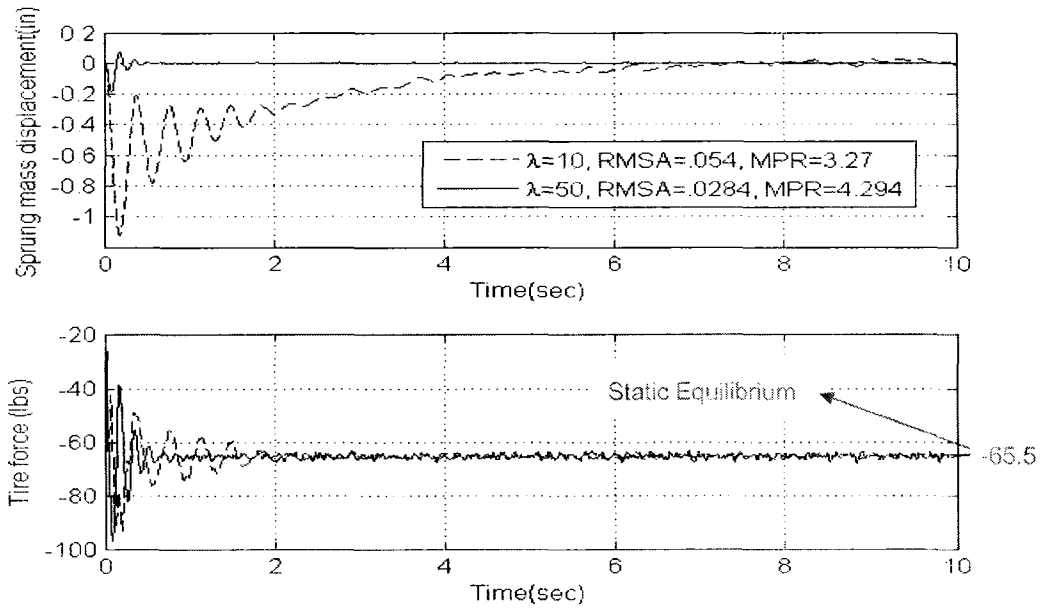

Figure 6.9: Comparing the performance of FLC for different gains

Figure 6.9 shows a comparison between the system responses for two different set of gains corresponding to triple poles equal to 10 and 50. The effective area is estimated as 6 in^2. The figure shows that as the gain increases, the oscillation decreases and the RMS of the sprung mass acceleration decreases. With reference to Figure 4.5, a zero tire force indicates potential loss of contact with the road. Figure 6.9 implies that the tire is always in contact with the road, and with the exception of the first fraction of a second the magnitude of the tire force is sufficiently large to ensure handling performance.

As the gain increases, the controller gets more robust against the effective area uncertainty. MPR increases from 3.27 to 4.294 by increasing the triple root from 10 to 50. Increasing the gains cannot be unlimited, because high gains demand high actuator power and saturation will be reached beyond the actuator power capacity. Actuator saturation highly affects the controller performance and, in some cases, can make the system unstable. Figure 6.10 shows the inlet orifice area for the two cases, shown in Figure 6.9. For $\lambda = 10$ a proportional valve with 0.025 in^2 orifice and a supply pressure equal to 100 psig is enough to control the system. But for $\lambda = 50$ this valve results in actuator saturation and a valve with higher capacity or a supply with higher pressure is required.

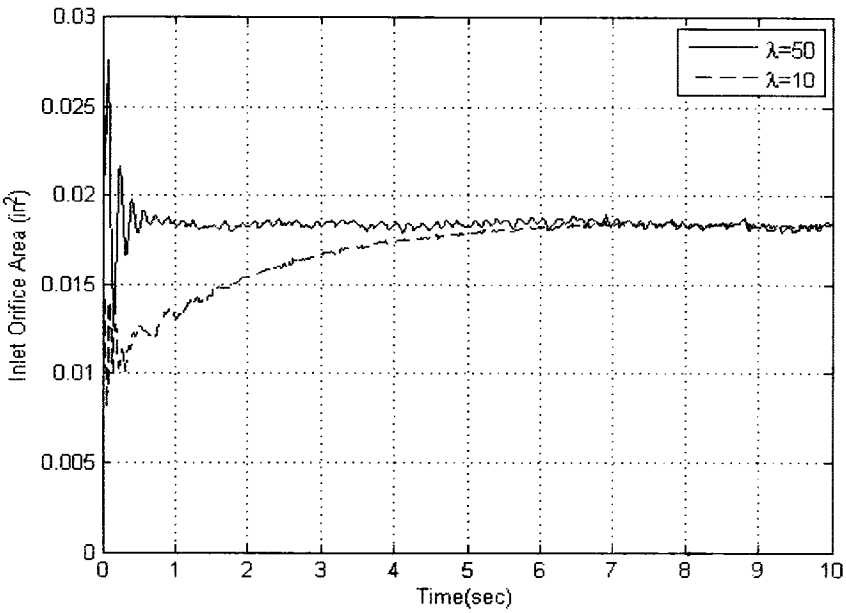

Figure 6.10: Comparing the inlet orifice for different gains

So far the air spring volume is assumed measurable. Since the bellows is made by compliant material and the shape of the air spring is not a simple geometrical shape, the measurement of the volume on line is very difficult. Therefore, the air spring volume has to be estimated by a constant value or estimated by a formula. This causes another uncertainty to the model. Figure 6.11 compares the sprung mass displacement and the tire force when the volume is known and when it is estimated at 4 in^3. The estimated effective area is 6 in^2 and the triple pole equal to 10.

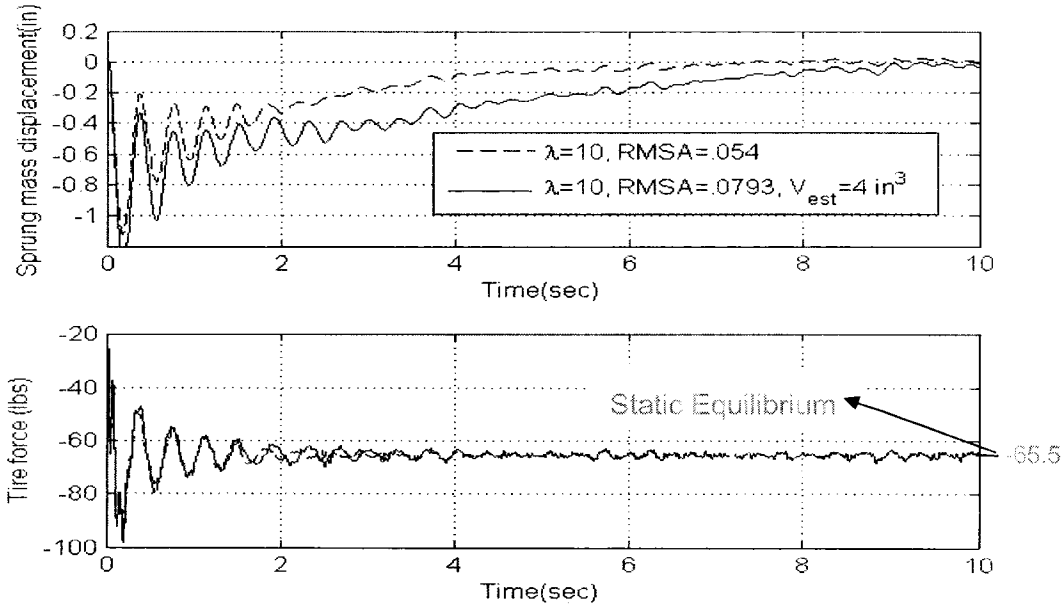

Figure 6.11: Comparing the system response in the presence and absence of volume uncertainty

As the figure shows, in the presence of volume uncertainty, the rise time increases and the RMS of the sprung mass acceleration increases by 47%. The tire force is always negative indicating that the tire is in contact with the road. The suspension performance and ride comfort gets worse in the presence of the volume uncertainty.

FLC controller demands high gains for good ride comfort in the presence of different uncertainties. On the other hand, high gain causes actuator saturation for an imprecise model. In fact, FLC demands a high actuator effort to cope with model uncertainties. Therefore a controller with a better performance in the presence of uncertainties is required.

6.4 Model Reference Feedback Linearization Control (MRFLC) of a Quarter Car Model with Pneumatic Suspension

The algorithm of MRFLC is very similar to FLC except that Equation 6.19 is substituted by the following equation.

$$v = \ddot{y}_d - K_a\ddot{e} - K_v\dot{e} - K_p e \qquad 6.22$$

where e is the tracking error between the model reference output y_d and the system output y:

$$e = y - y_d \qquad 6.23$$

Figure 6.12 shows the block diagram of MRFLC applied to the quarter car model.

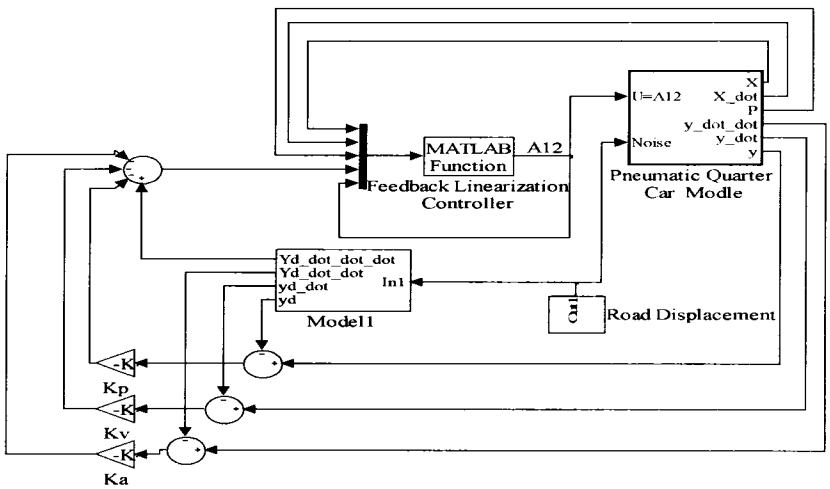

Figure 6.12: The block diagram of MRFLC

MRFLC is applied to the quarter car model with pneumatic suspension. Figure 6.13 shows the sensitivity curves for full scale quarter car model. The performance of MRFLC is very similar to FLC. The triple pole of the reference model is paced at -10.

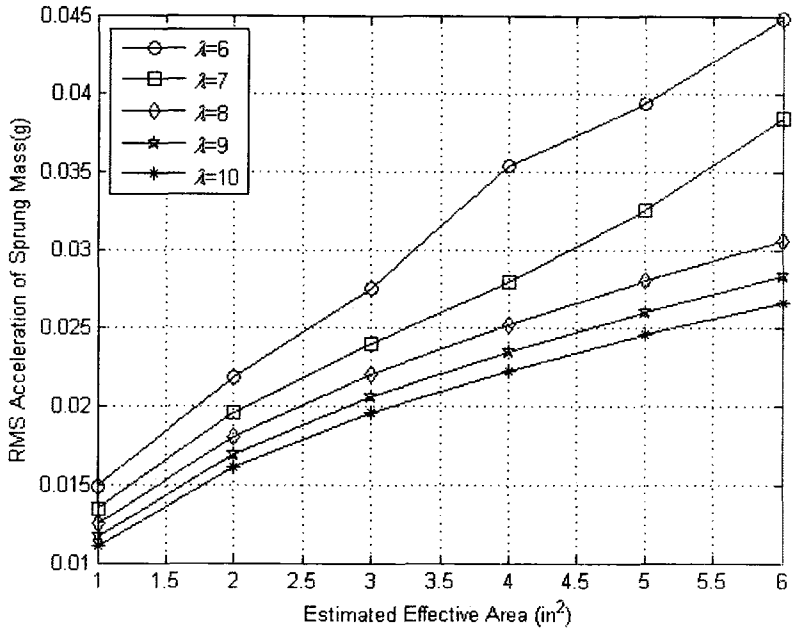

Figure 6.13: Sensitivity curves of MRFLC applied to the quarter car model based on RMS acceleration

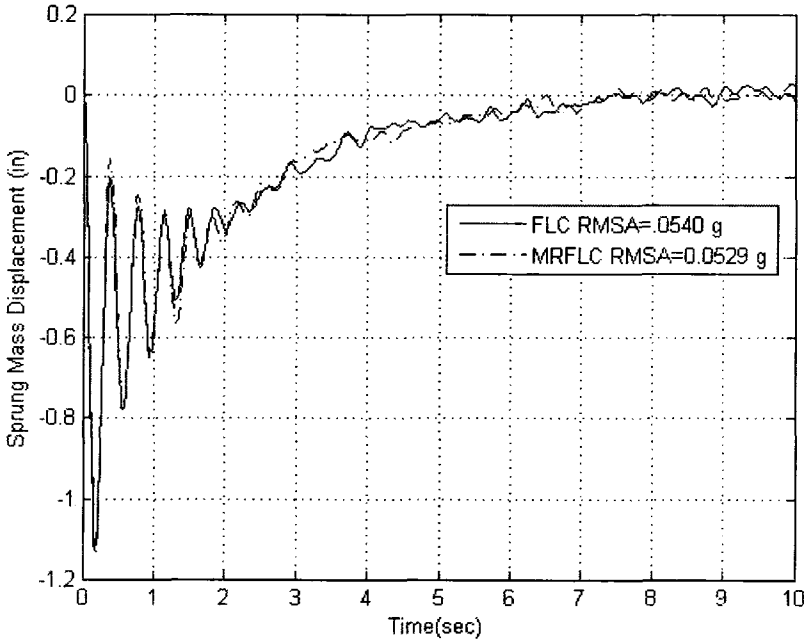

Figure 6.14: Comparing the performance of MRFLC and FLC

Figure 6.14 compares the responses of MRFLC and FLC. The effective area is estimated by 6 in^2 and the gains are calculated based on $\lambda = 10$. As the figure shows the sprung mass displacement and the RMS of sprung mass acceleration are very close.

6.5 Sliding Mode Control (SMC) of a Quarter Car with Pneumatic Suspension

In sliding mode control, a well behaved function of the tracking error named S is chosen. The control input is chosen so that the function $\frac{1}{2}S^2$ becomes a Lyapunov function. Therefore the control input is chosen to satisfy the Lyapunov stability criteria in the presence of the model uncertainty and disturbance. Different functions of tracking error are used in sliding mode control. Two frequently used forms of the tracking error function are as follows:

$$S = (\frac{d}{dt} + \lambda)^k \int e dt \qquad 6.24$$

$$S = (\frac{d}{dt} + \lambda)^{k-1} e \qquad 6.25$$

where k is the smallest order of the output derivative in which the input appears. The following function is considered as a candidate of Lyapunov function:

$$V_1 = \frac{1}{2}S^2 \qquad 6.26$$

V_1 is a positive definite function. According to the Lyapunov stability, the system is stable if the derivative of V is negative semi-definite as follows:

$$\frac{dV_1}{dt} \leq 0 \qquad 6.27$$

Taking derivative from Equation 6.26 gives:

$$\frac{dV_1}{dt} = S\dot{S} \qquad 6.28$$

If $\dot{S}$ is chosen as follows:

$$\dot{S} = -K_s \operatorname{sgn}(S) \qquad 6.29$$

where

$$\text{sgn}(S) = \begin{cases} +1 & if \quad S > 0 \\ -1 & if \quad S < 0 \\ 0 & if \quad S = 0 \end{cases} \tag{6.30}$$

then sliding gain K_s can be large enough to make $\frac{dV_l}{dt}$ a negative semi definite function in the presence of model uncertainties. Such a gain makes the system stable despite uncertainties.

In sliding mode control with a sign function defined by Equation 6.30, the output starts oscillating when it reaches the sliding surface $S=0$. This phenomenon is called chattering. In fact, abrupt changes in the input, due to the sign function, causes oscillation at the output. In order to remove chattering, a boundary layer with a thickness of ϕ is defined around the surface S=0. Outside this layer the control law will be governed by Equation 6.30 to make the boundary layer attractive. But inside the layer the sign function is replaced by a smooth function such as $\frac{S}{\phi}$, $\tanh(\frac{S}{\phi})$ or $\frac{2}{\pi}a\sin(\frac{S}{\phi})$. These functions make the abrupt change in the sign function smooth and are known as saturation function $sat(S)$. In this research the third one is used. In fact, the sign function is replaced with saturation function sat(S) which is defined as follows:

$$sat(S) = \begin{cases} \frac{2}{\pi}a\sin(\frac{S}{\phi}) & if \quad \left|\frac{S}{\phi}\right| \le 1 \\ \text{sgn}(\frac{S}{\phi}) & if \quad \left|\frac{S}{\phi}\right| > 1 \end{cases} \tag{6.31}$$

When the plant is a quarter car model with pneumatic suspension, the input appears in the third derivative of the output; therefore, Equation 6.24 and 6.25 become:

$$S = \dddot{e} + 3\lambda\ddot{e} + 3\lambda^2\dot{e} + \lambda^3\int e dt \tag{6.32}$$

$$S = \ddot{e} + 2\lambda\dot{e} + \lambda^2 e \tag{6.33}$$

Taking derivative from 6.32 and 6.33 gives:

$$\dot{S} = \ddot{e} + 3\lambda\dot{e} + 3\lambda^2\dot{e} + \lambda^3 e \tag{6.34}$$

$$\dot{S} = \ddot{e} + 2\lambda\dot{e} + \lambda^2\dot{e} \tag{6.35}$$

Substituting Equation 6.23 in 6.34 and 6.35 gives:

$$\dot{S} = \dddot{y} - \dddot{y}_d + 3\lambda\ddot{e} + 3\lambda^2\dot{e} + \lambda^3 e \tag{6.36}$$

$$\dot{S} = \ddot{y} - \ddot{y}_d + 2\lambda\ddot{e} + \lambda^2\dot{e} \tag{6.37}$$

Considering $f(X)$ and $b(X)$ as Equations 6.16 and 6.17 and substituting $\ddot{y}$ from Equation 6.13 into Equation 6.36 and 6.37 gives:

$$\dot{S} = f(X) + b(X)u - \dddot{y}_d + 3\lambda\ddot{e} + 3\lambda^2\dot{e} + \lambda^3 e \tag{6.38}$$

$$\dot{S} = f(X) + b(X)u - \ddot{y}_d + 2\lambda\ddot{e} + \lambda^2\dot{e} \tag{6.39}$$

where u is the input of the system; the inlet orifice area. Substituting Equation 6.38 and 6.39 individually in Equation 6.29 and solving for the input u yields:

$$u = b^{-1}(X)\{- f(X) + \dddot{y}_d - 3\lambda\ddot{e} - 3\lambda^2\dot{e} - \lambda^3 e - K_s \operatorname{sgn}(S)\} \tag{6.40}$$

$$u = b^{-1}(X)\{- f(X) + \ddot{y}_d - 2\lambda\ddot{e} - \lambda^2\dot{e} - K_s \operatorname{sgn}(S)\} \tag{6.41}$$

These inputs are obtained based on Equation 6.29, thus in the absence of uncertainties, they satisfy Equation 6.27 if and only if K_s is a positive number. Hence V_l is a Lyapunov function and the Lyapunov stability theorem guarantees the stability of the system. If the model is not precise, K_s is selected large enough to remove the effect of uncertainties and Equation 6.27 is satisfied. Since large values of K_s lead to actuator saturation, K_s cannot be taken unlimitedly large. K_s should be chosen to make a compromise between the control performance and actuator saturation.

Equation 6.40 gives the input corresponding to the tracking function defined by Equation 6.32. The system dynamic after eliminating the effects of uncertainties and reaching the sliding surface ($S = 0$) will be governed by Equation 6.20. Therefore the system is stable and the steady state error is zero. When the tracking error function is chosen as Equation 6.33, the system dynamic after eliminating the effects of uncertainties is as follows:

$$\frac{Y(s)}{R(s)} = \frac{1}{s(s^2 + 2\lambda s + \lambda^2)} \tag{6.42}$$

Considering the final value theorem, the final value of the output of this transfer function is not zero. Therefore, the sliding mode control based on the tracking error function defined by Equation 6.33 results in an output with offset.

Equation 6.40 is a combination of the FLC input given by Equation 6.15 and the pure sliding mode controller which is introduced in some literatures [49]. Following a similar approach, the control input given by Equation 6.40 can be used with different tracking error function. Therefore, in addition to the two introduced forms of tracking error function, another form can be defined as follows:

$$S = \dot{e} + \lambda e \tag{6.43}$$

In order to differentiate between different sliding mode controllers, the sliding mode based on Equations 6.32 and 6.33 are called third order integral SMC and third order SMC respectively. The controller with the input given by Equation 6.40 and the tracking error given by Equation 6.33 are called third order SMFLC and the controller with the input given by Equation 6.40 and the tracking error given by Equation 6.43 is called first order SMFLC.

The different sliding mode controllers are applied to the quarter car model with pneumatic suspension and their performances are compared in Figure 6.15.

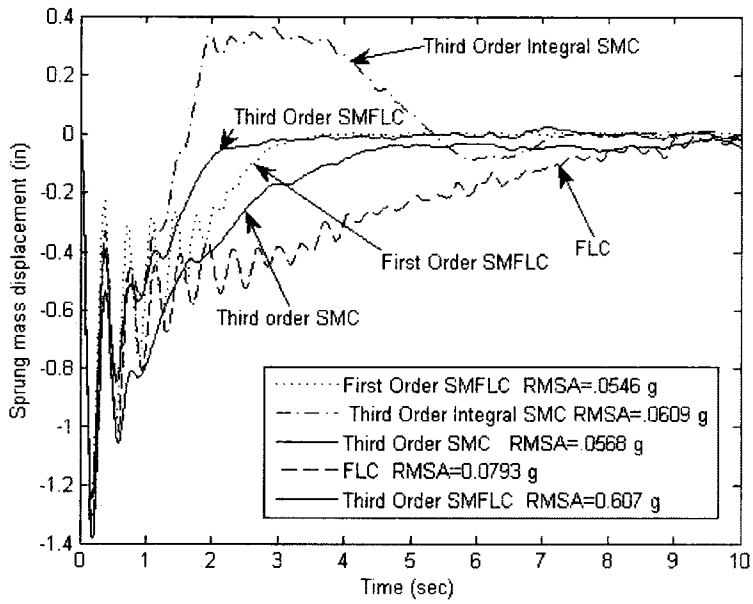

Figure 6.15: Comparing the performances of the different sliding mode controllers

The air spring volume and effective area are estimated by 6 in^2 and 4 in^3 respectively. In fact the controller estimates the air spring by a pneumatic cylinder with constant volume. λ is taken equal to 10. The sliding gain K_s and boundary layer thicknesses are 1000 and 1, respectively.

As was discussed before, the output of the third order SMC has an offset. The third order integral SMC has a large overshoot resulting from the integral element. The first order SMFLC has the best RMS of acceleration (RMSA) and the third order SMFLC has the best rise time. Since the RMSA is important for ride comfort, the first order SMFLC is the best controller for the pneumatic suspension system.

In order to obtain the sensitivity curves, the first order SMFLC is applied to the quarter car model with pneumatic suspension. The volume and effective area of the air spring are assumed to be unknown and are estimated by constant values in the controller. The volume of the air spring is estimated by a constant volume of 4 in^3. A 0.4 in error in the estimated air spring height is also assumed. The air spring height is used to calculate the mean area and the time derivative of the air spring volume using Equations 4.26 and 4.27. The sliding gain is increased to 10000 to decrease the rise time. The boundary layer thickness is increased to 5, to avoid saturation inside the boundary layer. The sensitivity curves for different estimated effective areas and different triple poles are shown in Figure 6.16. The sensitivity curves based on mean personal rating is shown in Figure 6.17. In spite of the presence of different uncertainties, all curves are in the area of very good ride comfort. The sensitivity of the ride comfort to the triple pole has reduced considerably and the sliding mode gain K_s plays a more important role than the location of the triple pole.

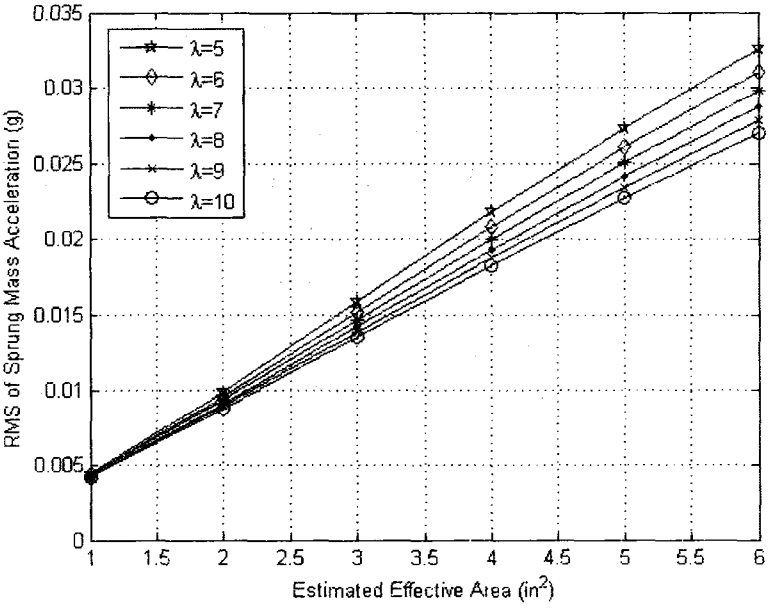

Figure 6.16: Sensitivity curves of first order SMFLC based on RMS of acceleration

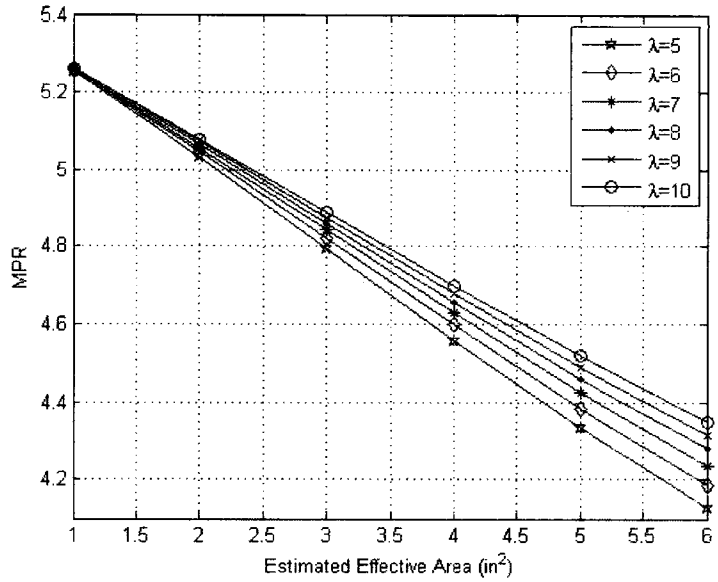

Figure 6.17: Sensitivity curves of first order SMFLC based on MPR

The sprung mass displacement of the point corresponding to A=6 in^2 and $\lambda = 10$ is compared with that of the first order SMFLC with K_s=1000, ϕ =1 and the same A and λ in Figure 6.18.. The figure shows that increasing the sliding gain and the boundary thickness improves considerably the controller performance. The RMS of sprung mass acceleration decreases from .0546 g to .0263 g, implying that the ride comfort is also improved considerably.

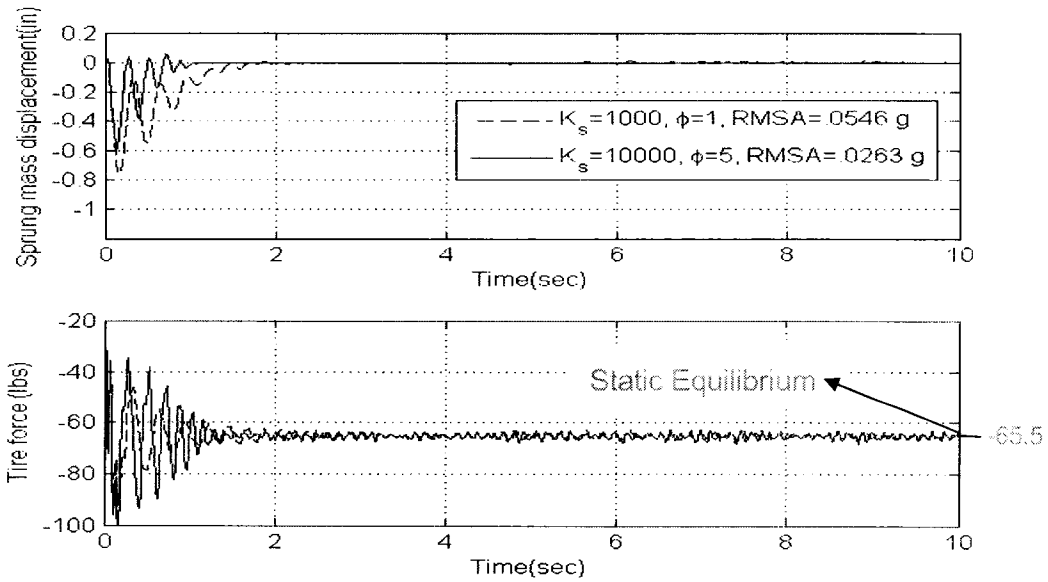

Figure 6.18: The sprung mass displacement and tire force of the first order SMFLC in the presence of different uncertainties

The tire force increases in transient part but decreases after settling time. The inlet orifice area of this point is shown in Figures 6.19. The figure shows that, despite different uncertainties, a proportional valve with 0.025 in^2 orifice can still control the system without saturation.

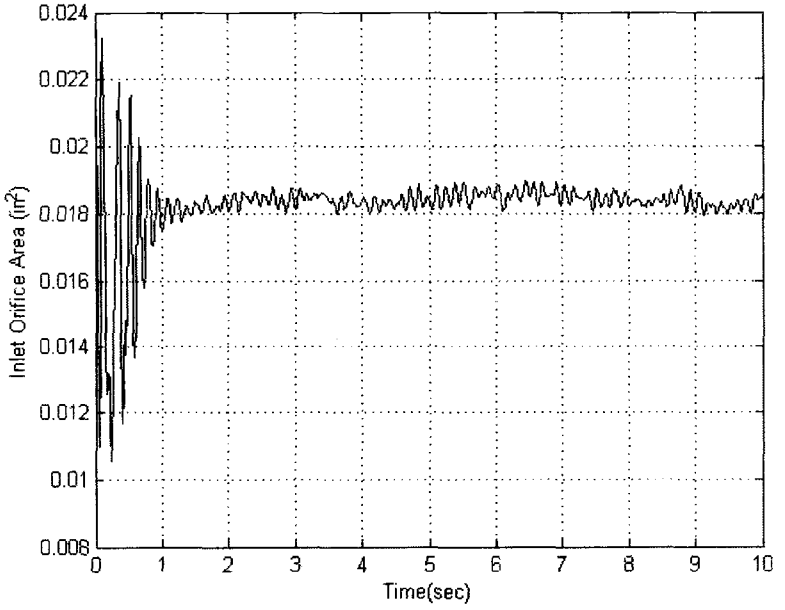

Figure 6.19: The inlet orifice area for first order SMFLC in the presence of different uncertainty

6.6 Sliding Mode Control with Parameter Estimator of a Quarter Car Model with Pneumatic Suspension

It was shown previously that the effective area of the air spring and its derivative are one of the major sources of model uncertainties in pneumatic suspension. If the effective area can be estimated online by a parameter estimator, the uncertainty can be partially removed.

There are some nonlinear adaptive techniques, such as adaptive sliding mode, that can estimate the unknown parameters based on the tracking error. The unknown parameters are estimated so that the tracking error converges zero. The ultimate goal behind using these techniques is to reduce the tracking error not the parameter estimation error. On the other hand, these techniques are based on the assumption that the unknown parameter is the only model uncertainty and there is no other uncertainty. Even though, these

techniques result in good performances for suspensions with pneumatic cylinders, their performance is not so good for suspensions with air springs. In an air spring, in addition to the unknown effective area, there are other uncertainties. The effective area is changing fast and its time derivative is an important source of uncertainty. On the other hand, the parameter estimation based on the estimation error can track the unknown parameters very well and remove the uncertainties caused by the time derivative of these parameters. In this section a parameter estimator is implemented to estimate the effective area while the first order SMFLC controls the suspension.

6.6.1 Algorithm of Different Parameter Estimations Based on Prediction Error

In order to estimate unknown parameters, the unknown parameters are assumed to be related to the known parameters and variables as follows:

$$\mathbf{Y}(t) = \mathbf{W}(t)\mathbf{a}(t) + \mathbf{\Psi}(t) \tag{6.44}$$

where $\boldsymbol{Y}$ is a vector of measurable variables, $\boldsymbol{W}$ and $\boldsymbol{\Psi}$ are functions of known variables and parameters, and $\boldsymbol{a}$ is the vector of unknown parameters. The variable vector $\boldsymbol{Y}$ either can be measured by sensors or estimated using the following equation:

$$\hat{\mathbf{Y}}(t) = \mathbf{W}(t)\hat{\mathbf{a}}(t) + \mathbf{\Psi}(t) \tag{6.45}$$

where the estimated variables and parameters are denoted by superscript "^".

There would be an error between the estimated output vector and the measured one. This error is called prediction error and is denoted by $\mathbf{e}_1$. Denoting the parameter estimation error by superscript "~" the prediction error $\mathbf{e}_1$ can be expressed as follows:

$$\begin{aligned} \mathbf{e}_1 &= \hat{\mathbf{Y}}(t) - \mathbf{Y}(t) \\ &= \mathbf{W}(t)\tilde{\mathbf{a}}(t) \end{aligned} \tag{6.46}$$

There are different estimation methods based on the prediction error such as gradient, standard least-square, least-square with exponential forgetting, and least-square with variable forgetting factor. The gradient method simply estimates the parameter as follow:

$$\begin{aligned} \dot{\hat{\mathbf{a}}}(t) &= -p\frac{\partial\left|\mathbf{e}_1{}^T\mathbf{e}_1\right|}{\partial\hat{\mathbf{a}}} \\ &= -p\mathbf{W}(t)\mathbf{e}_1 \end{aligned} \tag{6.47}$$

where p is a positive number or a diagonal positive definite matrix. The gradient estimator can track the parameter in the absence of noise and disturbance. But in the

presence of the noise and disturbance, the faster the parameter varies, the larger parameter estimation error is.

The least-square estimator estimates the unknown parameter as follows:

$$\dot{\hat{\mathbf{a}}}(t) = -\mathbf{P}(t)\mathbf{W}(t)\mathbf{e}_1 \tag{6.48}$$

where $\mathbf{P}(t)$ is called the estimator gain matrix and is calculated as follows:

$$\dot{\mathbf{P}} = -\mathbf{P}\mathbf{W}^T\mathbf{W}\mathbf{P} \tag{6.49}$$

Since the least-squares estimator fits all previous data to estimate the parameter, it is robust against noise and disturbance but has a poor tracking ability. To eliminate the effect of the old data and improve the tracking properties of the least square, a forgetting factor is used and the gain matrix is updated as follows:

$$\dot{\mathbf{P}} = \lambda_f(t)\mathbf{P} - \mathbf{P}\mathbf{W}^T\mathbf{W}\mathbf{P} \tag{6.50}$$

In order to avoid the divergence of $\mathbf{P}$, λ_f is a chosen variable whose values are updated as follows:

$$\lambda_f(t) = \lambda_0\left(1 - \frac{\|\mathbf{P}\|}{k_0}\right) \tag{6.51}$$

where λ_0 is the initial forgetting factor and k_0 is the maximum value of the magnitude of $\mathbf{P}$. The least-square estimator with updating gain matrix given by Equation 6.49 and updating forgetting factor given by Equation 6.51 is called bounded forgetting factor least-square estimator [50].

6.6.2 Applying Least-Square Estimator with Bonded Forgetting Factor to the Quarter Car Model with Pneumatic Suspension

In order to estimate the effective area, a relationship between the effective area and the measurable parameters and variables should be established. Considering Equation 4.53, the sprung mass acceleration is related to the effective area by pressure and sprung mass. The air spring pressure and the sprung mass are a measurable variable and known parameter respectively. The acceleration can be calculated from the sprung mass displacement using a robust differentiator technique [51] or can be measured directly using

an accelerometer. Therefore Equation 4.53 can be written in the form of Equation 6.44 as follows:

$$\overbrace{\ddot{Z}_s}^{Y} = \frac{\overbrace{P_2}^{W}}{m_s}\overbrace{A}^{a} - \overbrace{g}^{\Psi} \tag{6.52}$$

Considering Equation 6.48 and 6.52, the estimated effective area can be updated by the following equation:

$$\dot{\hat{A}}(t) = -\mathbf{P}(t)(\frac{P_2}{m_s})\mathbf{e}_1 \tag{6.53}$$

where $\mathbf{P}(t)$ and $\lambda(t)$ are updated using Equations 6.50 and 6.51, respectively. The prediction error is calculated as follows:

$$\mathbf{e}_1 = \hat{\ddot{Z}}_s - \ddot{Z}_s \tag{6.54}$$

where $\hat{\ddot{Z}}_s$ is estimated sprung mass acceleration . $\hat{\ddot{Z}}_s$ is calculated by the following equation:

$$\hat{\ddot{Z}}s = \frac{P_2}{ms}\hat{A} - g \tag{6.55}$$

The first order SMFLC with bounded forgetting factor least-square estimator is applied to the quarter car model with pneumatic suspension. Figure 6.20 compares the sprung mass displacement and the tire force of this controller with first order SMFLC without parameter estimator.

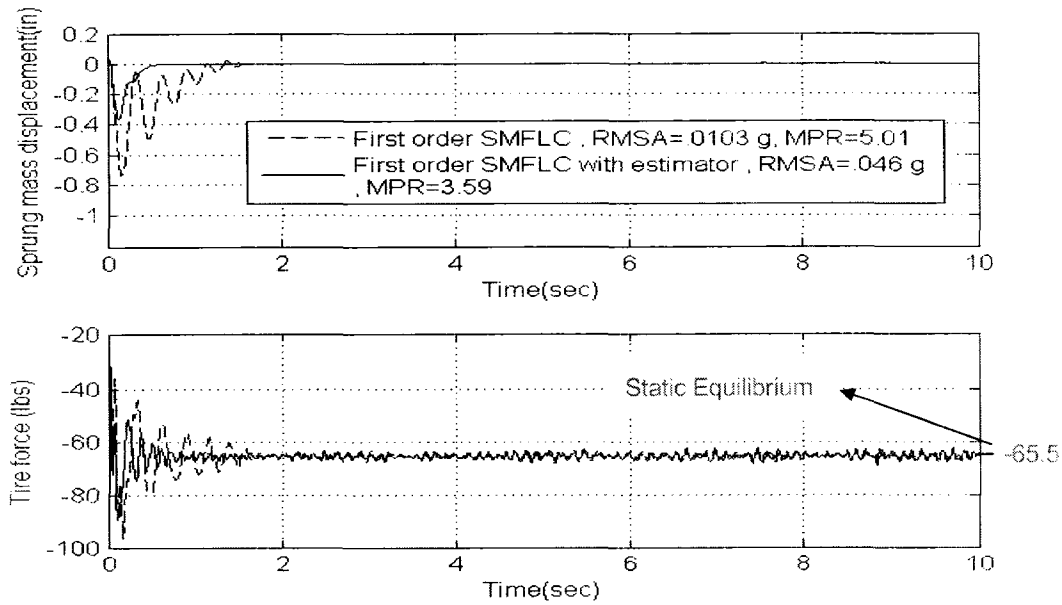

Figure 6.20: Comparing performance of first order SMFLC in the presence and absence of the parameter estimator

Different uncertainties are assumed to exist in the volume and assembly height of the air spring. The volume of the air spring is estimated by a constant volume of 4 in^3 and it is assumed that the air spring height is read by an error equal to 0.4 inches. The sliding gain and the boundary layer thickness are chosen 2000 and 2, respectively. Figure 6.20 shows that the estimator improves the performance of the system considerably. Ride comfort increases from 3.59 MPR to 5 MPR. The oscillation and rise time of the sprung mass displacement and the tire force decrease considerably.

Figure 6.21 shows the parameter tracking ability of the estimator in the presence of uncertainties. The estimator estimates the effective area of the air spring in less than 0.5 s. The RMS of estimation error after 0.5 sec is .003 in^2.

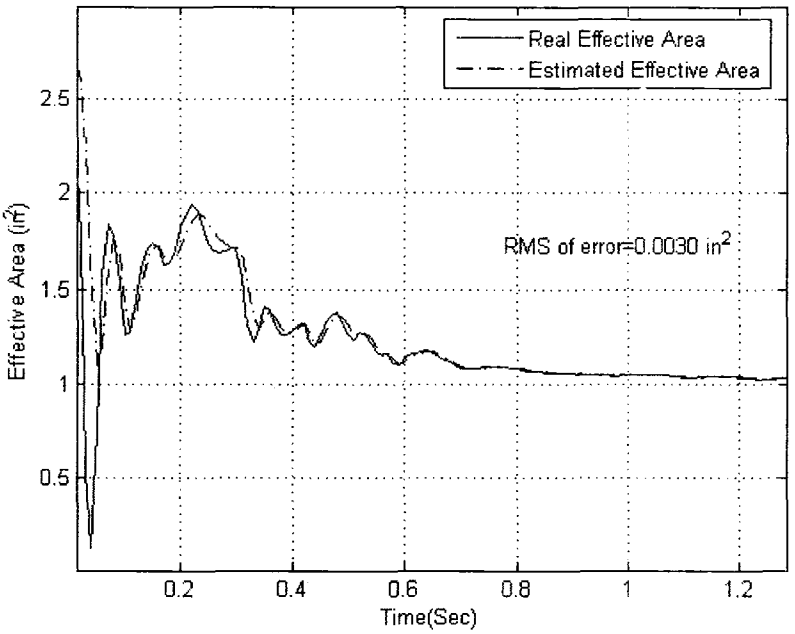

Figure 6.21: Comparison of the real and estimated effective area for the first order SMFLC in the presence of different uncertainties

Inlet orifice areas for the two cases are compared in Figure 6.22. The actuator effort increases in the presence of the estimator, especially in the transient part of the response. But the increase in the actuator effort does not cause saturation. In fact a control valve with .025 in^2 maximum orifice area can produce the desired control input.

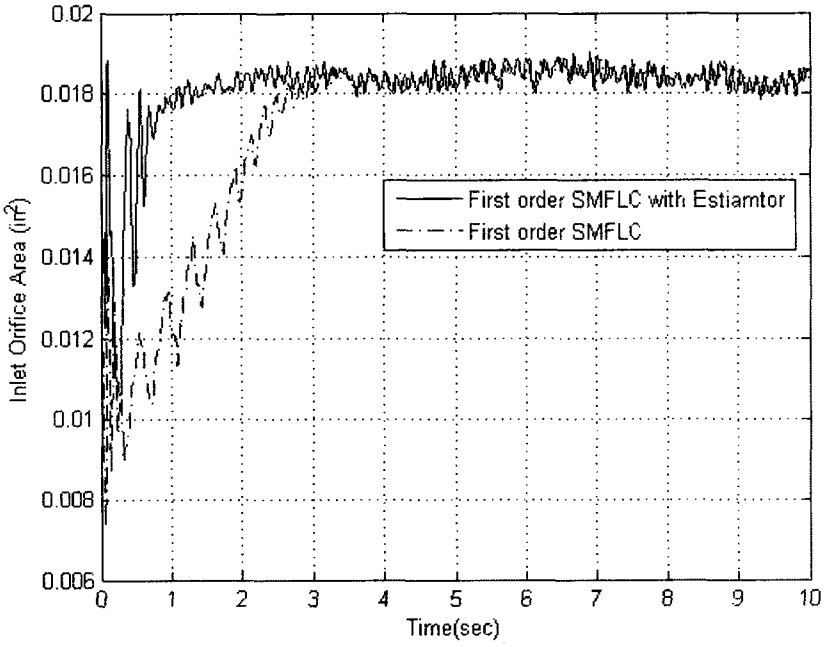

Figure 6.22: Comparison of inlet orifice areas for first order SMFLC with and without estimator in the presence of different uncertainty

The sensitivity curve of the first order SMFLC with estimator with the same uncertainties in the air spring volume and height is shown in Figure 6.23. The sliding gain and the layer boundary thickness are 2000 and 2 respectively. As the figure shows MPR is very high even for small λ . The sensitivity to the magnitude of the triple pole λ decreases considerably.

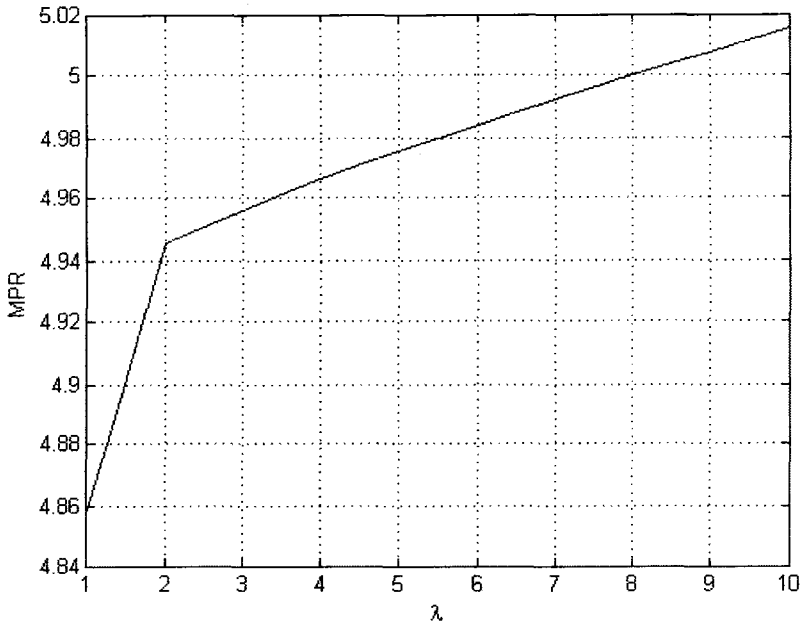

Figure 6.23: The sensitivity curve of first order SMFLC with estimator

Another uncertainty which is more probable is the payload uncertainty. The sprung mass consists of the car and passengers masses. Since the number of passenger and their weight vary, another uncertainty is introduced to the mathematical model. This uncertainty affects both the estimator and the SMFLC. In order to study the effect of the payload uncertainty on the controller, its effect on the estimator should be studied carefully. Substituting Equations 6.55 and 6.52 in 6.54 and rearranging give the prediction error as:

$$\mathbf{e}_1 = (\frac{\hat{A}}{\hat{m}_s} - \frac{A}{m_s})P_2$$

where $\hat{m}_s$ is the estimated sprung mass. Since the estimator tries to make the prediction error zero, the following condition should be satisfied:

$$\frac{\hat{A}}{\hat{m}_s} = \frac{A}{m_s} \qquad 6.56$$

Rearranging Equation 6.56 gives:

$$\frac{m_s}{\hat{m}_s} = \frac{A}{\hat{A}} \qquad 6.57$$

This relation implies that if the estimated sprung mass is taken equal to the maximum mass capacity of the car, the estimated effective area is tuned by payload as Equation 6.56. For example, if the payload is half of the mass capacity of the car, then the estimated effective area becomes twice the real effective area. It should be noted that the effective area and sprung mass appear in the mathematical model are as a ratio of $\frac{A}{m_s}$. Therefore, if the controller is designed based on the maximum capacity of the car, the effective area and the sprung mass uncertainties compensate each other. Since the air spring should be chosen based on the maximum mass capacity of the car, designing the controller based on that is reasonable. In this research, the maximum mass capacity of the car is assumed to be twice the mass of the car body. Figure 6.24 shows a comparison the sprung mass displacement with and without payload uncertainty. In the absence of uncertainty, the estimated and real sprung masses are both equal to the car body mass. In the presence of uncertainty, the estimated sprung mass is twice the car body mass. The performance of the controller in the presence and absence of the payload uncertainty is almost the same. The load tire variation also does not change considerably. It should be noted that the uncertainties in the volume and height of the air spring are as the previous case.

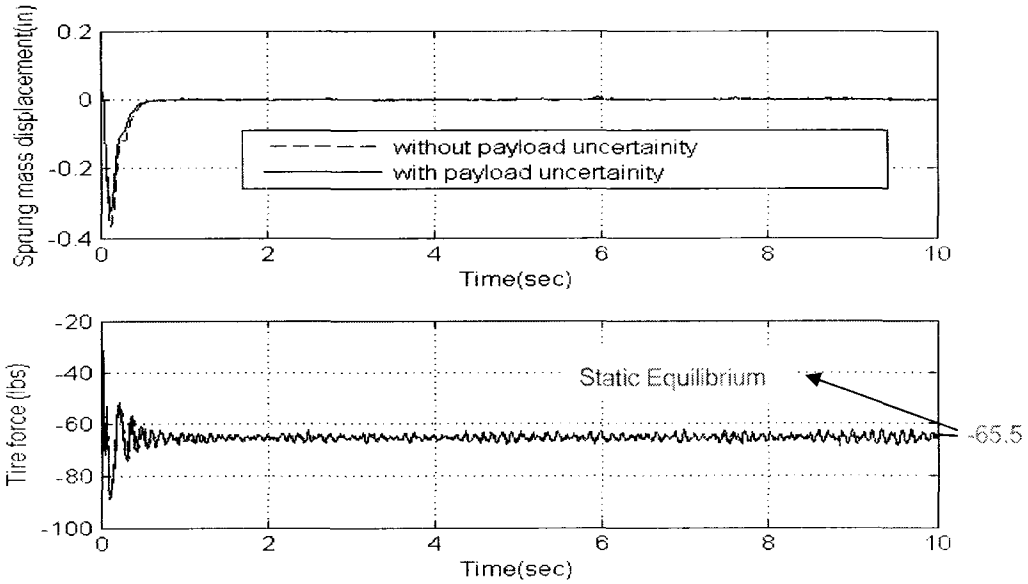

Figure 6.24: The sprung mass displacement and the tire force of the first order SMFLC

The inlet orifice area is shown in Figure 6.25. Comparing Figure 6.25 with Figure 6.22 shows that the inlet orifice in the presence and absence of payload uncertainty is almost the same. Obviously the larger payload demands the larger actuator efforts. Thus the possibility of actuator saturation increases as the payload increases. Actuator saturation can be avoided by either choosing an air spring with large effective area or by increasing the supply pressure. Since there is limitation in supply pressure, the air spring should be chosen based on the maximum pay load.

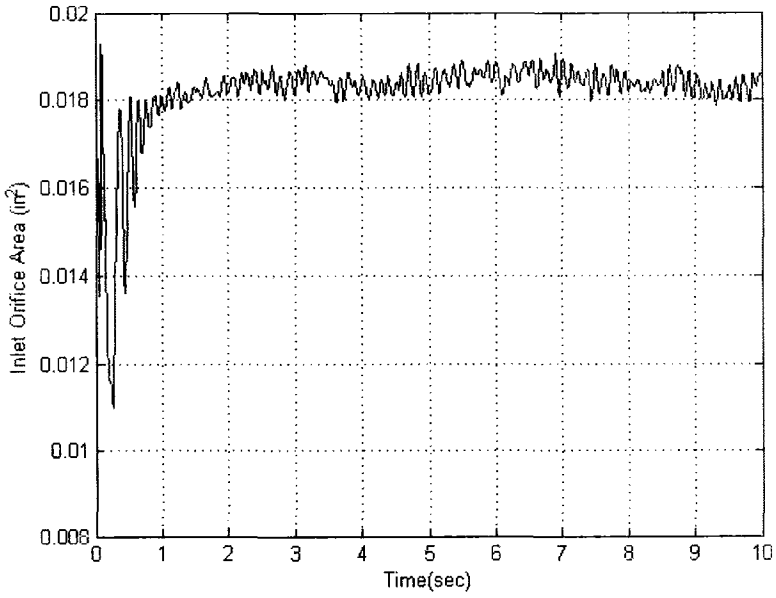

Figure 6.25: The inlet orifice area in the presence of payload uncertainty

6.7 Sliding Mode Control with Parameter Estimator of a Half Car Model with Pneumatic Suspension

6.7.1 The Algorithm of Feedback Linearization Control (FLC)

The mathematical model of a half car model with pneumatic suspension was presented in Section 4.6. Equations 4.63 to 4.72 are the mathematical model of a half car model with pneumatic suspension. Heave displacement Z_s and pitch angle θ are considered as the outputs of the system. The output vector $\mathbf{Y}$ is defined as:

$$\mathbf{Y} = \begin{bmatrix} Z_s \\ \theta \end{bmatrix} \tag{6.58}$$

The inputs of the system are front and rear inlet orifice areas. The input vector $\mathbf{U}$ is defined as:

$$\mathbf{U} = \begin{bmatrix} A_{12f} \\ A_{12r} \end{bmatrix} \tag{6.59}$$

The second time derivative of the output vector is as follows:

$$\ddot{\mathbf{Y}} = \begin{bmatrix} \ddot{Z}_s \\ \ddot{\theta} \end{bmatrix} \tag{6.60}$$

Substituting for $\ddot{Z}_s$ and $\ddot{\theta}$ from Equations 4.63 and 4.64, respectively, gives:

$$\ddot{\mathbf{Y}} = \begin{bmatrix} \dfrac{P_{2f}A_f + P_{2r}A_f - m_s g}{m_s} \\ \dfrac{aP_{2f}A_f - bP_{2r}A_f}{J} \end{bmatrix} \tag{6.61}$$

Taking the third derivative of the output:

$$\dddot{\mathbf{Y}} = \begin{bmatrix} \dfrac{\dot{P}_{2f}A_f + \dot{P}_{2r}A_f}{m_s} \\ \dfrac{a\dot{P}_{2f}A_f - b\dot{P}_{2r}A_f}{J} \end{bmatrix} \tag{6.62}$$

Substituting for $\dot{P}_{2f}$ and $\dot{P}_{2r}$ from Equations 4.67 and 4.68 respectively gives:

$$\ddot{\mathbf{Y}} = \begin{bmatrix} -\dfrac{nP_{2f}A_f}{V_{2f}m_s}\dfrac{dV_{2f}}{dt} - \dfrac{nP_{2r}A_r}{V_{2r}m_s}\dfrac{dV_{2f}}{dt} + \dfrac{nKR\sqrt{T_1}}{m_s}\left\{\dfrac{A_fP_{2f}}{V_{2f}}\right. \\ \left.\left[\dfrac{T_2}{T_1}(C_{12f})A_{12f} - (\dfrac{T_2}{T_1})^{\frac{1}{2}}A_{23f}N_{23f}\right] + \dfrac{A_rP_{2r}}{V_{2r}}\left[\dfrac{T_2}{T_1}(C_{12r})A_{12r} - (\dfrac{T_2}{T_1})^{\frac{1}{2}}A_{23r}N_{23r}\right]\right\} \\ -\dfrac{naP_{2f}A_f}{V_{2f}J}\dfrac{dV_{2f}}{dt} + b\dfrac{nP_{2r}A_r}{V_{2r}J}\dfrac{dV_{2f}}{dt} + \dfrac{nKR\sqrt{T_1}}{J}\left\{\dfrac{aA_fP_{2f}}{V_{2f}}\right. \\ \left.\left[\dfrac{T_2}{T_1}(C_{12f})A_{12f} - (\dfrac{T_2}{T_1})^{\frac{1}{2}}A_{23f}N_{23f}\right] - \dfrac{bA_rP_{2r}}{V_{2r}}\left[\dfrac{T_2}{T_1}(C_{12r})A_{12r} - (\dfrac{T_2}{T_1})^{\frac{1}{2}}A_{23r}N_{23r}\right]\right\} \end{bmatrix} \quad 6.63$$

Equation 6.63 can be written in the following form:

$$\ddot{\mathbf{Y}} = \mathbf{BU} + \mathbf{F} \quad 6.64$$

where matrixes F and B are defined as:

$$B = \begin{bmatrix} b_{11} & b_{12} \\ b_{21} & b_{22} \end{bmatrix} \quad 6.65$$

$$F = \begin{bmatrix} f_1 \\ f_2 \end{bmatrix} \quad 6.66$$

with the following elements:

$$f_1 = -\frac{nP_{2f}A_f}{V_{2f}m_s}\frac{dV_{2f}}{dt} - \frac{nP_{2r}A_r}{V_{2r}m_s}\frac{dV_{2f}}{dt} - \frac{nKR\sqrt{T_1}}{m_s}\frac{A_fP_{2f}}{V_{2f}}(\frac{T_2}{T_1})^{\frac{1}{2}}A_{23f}N_{23f} - \frac{nKR\sqrt{T_1}}{m_s}\frac{A_rP_{2r}}{V_{2r}}(\frac{T_2}{T_1})^{\frac{1}{2}}A_{23r}N_{23r} \quad 6.67$$

$$f_2 = -\frac{naP_{2f}A_f}{V_{2f}m_s}\frac{dV_{2f}}{dt} + \frac{nbP_{2r}A_r}{V_{2r}m_s}\frac{dV_{2f}}{dt} - \frac{naKR\sqrt{T_1}}{m_s}\frac{A_fP_{2f}}{V_{2f}}(\frac{T_2}{T_1})^{\frac{1}{2}}A_{23f}N_{23f} + \frac{nbKR\sqrt{T_1}}{m_s}\frac{A_rP_{2r}}{V_{2r}}(\frac{T_2}{T_1})^{\frac{1}{2}}A_{23r}N_{23r} \quad 6.68$$

$$b_{11} = \frac{nKR\sqrt{T_1}}{m_s}\frac{A_f P_{2f}}{V_{2f}}\frac{T_2}{T_1}(C_{12f}) \tag{6.69}$$

$$b_{12} = \frac{nKR\sqrt{T_1}}{m_s}\frac{A_r P_{2r}}{V_{2r}}\frac{T_2}{T_1}(C_{12r}) \tag{6.70}$$

$$b_{21} = \frac{naKR\sqrt{T_1}}{m_s}\frac{A_f P_{2f}}{V_{2f}}\frac{T_2}{T_1}(C_{12f}) \tag{6.71}$$

$$b_{22} = -\frac{nbKR\sqrt{T_1}}{m_s}\frac{A_r P_{2r}}{V_{2r}}\frac{T_2}{T_1}(C_{12r}) \tag{6.72}$$

Solving Equation 6.64 for the input vector **U** gives:

$$\mathbf{U} = \mathbf{B}^{-1}(\ddot{\mathbf{Y}} - \mathbf{F}) \tag{6.73}$$

$\ddot{\mathbf{Y}}$ is considered as:

$$\ddot{\mathbf{Y}} = -K_a\ddot{\mathbf{Y}} - K_v\dot{\mathbf{Y}} - K_p(\mathbf{Y} - \mathbf{R}) \tag{6.74}$$

where vector **R** is the vector of reference input.

Substituting Equation 6.74 into 6.73 the FLC input $\mathbf{U}_c$ is as follows:

$$\mathbf{U}_c = \mathbf{B}^{-1}(-K_a\ddot{\mathbf{Y}} - K_v\dot{\mathbf{Y}} - K_p(\mathbf{Y} - \mathbf{R}) - \mathbf{F}) \tag{6.75}$$

6.7.2 The Algorithm of Model Reference Control (MRC)

In order to obtain the model reference control input the tracking error vector is defined as follows:

$$\begin{aligned}\mathbf{E} &= \mathbf{Y} - \mathbf{Y}_d \\ &= \begin{bmatrix} Z_s \\ \theta \end{bmatrix} - \begin{bmatrix} Z_{sd} \\ \theta_d \end{bmatrix} \\ &= \begin{bmatrix} Z_s - Z_{sd} \\ \theta - \theta_d \end{bmatrix}\end{aligned} \tag{6.76}$$

where Z_{sd}, θ_d and $\mathbf{Y}_d$ are desired heave displacement, desired pitch angle and the desired output vector of the reference model, respectively. The model reference input is calculated by Equation 6.73, where $\ddot{\mathbf{Y}}$ is defined as follows:

$$\ddot{\mathbf{Y}} = \ddot{\mathbf{Y}}_d - K_a\ddot{\mathbf{E}} - K_v\dot{\mathbf{E}} - K_p\mathbf{E} \tag{6.77}$$

Substituting Equation 6.77 into Equation 6.73 gives the MRFLC input as follows:

$$\mathbf{U}_c = \mathbf{B}^{-1}(\ddot{\mathbf{Y}}_d - K_a\ddot{\mathbf{E}} - K_v\dot{\mathbf{E}} - K_p\mathbf{E} - \mathbf{F}) \tag{6.78}$$

6.7.3 The Algorithm of Sliding Mode control SMC

In order to obtain the sliding mode controller input, a sliding function vector is defined as follows:

$$\begin{aligned}\mathbf{S} &= (\frac{d}{dt}+\lambda)^3 \int \mathbf{E}dt \\ &= \ddot{\mathbf{E}} + 3\lambda\dot{\mathbf{E}} + 3\lambda^2\mathbf{E} + \lambda^3 \int \mathbf{E}dt\end{aligned} \tag{6.79}$$

Taking the time derivative from Equation 6.79 gives:

$$\begin{aligned}\dot{\mathbf{S}} &= \dddot{\mathbf{E}} + 3\lambda\ddot{\mathbf{E}} + 3\lambda^2\dot{\mathbf{E}} + \lambda^3\mathbf{E} \\ &= \dddot{\mathbf{Y}} - \dddot{\mathbf{Y}}_d + 3\lambda\ddot{\mathbf{E}} + 3\lambda^2\dot{\mathbf{E}} + \lambda^3\mathbf{E}\end{aligned} \tag{6.80}$$

Considering the following function as a Liapunov function candidate:

$$V_l = \frac{1}{2}\mathbf{S}^T\mathbf{S} \tag{6.81}$$

its time derivative is as follows:

$$\dot{V}_l = \dot{\mathbf{S}}^T\mathbf{S} \tag{6.82}$$

Equation 6.82 is a negative definite if

$$\dot{\mathbf{S}} = -\mathbf{K}sign(\mathbf{S}) \tag{6.83}$$

where $\mathbf{K}$ sliding gain matrix which is a diagonal positive matrix. Substituting for $\dot{\mathbf{S}}$ from Equation 6.80 gives:

$$\dddot{\mathbf{Y}} - \dddot{\mathbf{Y}}_d + 3\lambda\ddot{\mathbf{E}} + 3\lambda^2\dot{\mathbf{E}} + \lambda^3\mathbf{E} = -\mathbf{K}sign(\mathbf{S}) \tag{6.84}$$

Substituting for $\dddot{\mathbf{Y}}$ from Equation 6.64 and solving for the input $\mathbf{U}$ gives the sliding mode control input $\mathbf{U}_c$ as follows:

$$\mathbf{U}_c = \mathbf{B}^{-1}(\ddot{\mathbf{Y}}_d - 3\lambda\ddot{\mathbf{E}} - 3\lambda^2\dot{\mathbf{E}} - \lambda^3\mathbf{E} - \mathbf{F} - \mathbf{K}sign(\mathbf{S})) \tag{6.85}$$

Equation 6.85 implies that existence of the control input depends to singularity of matrix $\mathbf{B}$. The determinant of Matrix $\mathbf{B}$ is as follows:

$$\det(\mathbf{B}) = b_{11}b_{22} - b_{12}b_{21} \tag{6.86}$$

Comparing Equation 6.69 with Equation 6.71 and Equation 6.70 with Equation 6.72, following relations can be found between the elements of Matrix $\mathbf{B}$:

$$\begin{aligned}b_{21} &= ab_{11} \\ b_{22} &= bb_{12}\end{aligned} \tag{6.87}$$

Substituting Equations 6.87 into Equation 6.86 gives:

6.88

$$\det(\mathbf{B}) = -(a+b)b_{11}b_{12}$$

Since $a \neq -b$, Equation 6.88 implies that $\det(\mathbf{B})$ is zero only if one of the elements of the first row of matrix $\mathbf{B}$ is zero. Equations 6.69 and 6.71 imply that b_{11} and b_{12} are zero only if C_{12f} and C_{12r} are zero. On the other hand, Equations 4.12 and 4.30 proves that C_{12f} and C_{12r} will not be zero unless the supply pressure and the air spring pressure are the same. Therefore in order to have a controllable system the following condition should be satisfied:

$$\begin{aligned} P_{1f} &\neq P_{2f} \\ P_{1r} &\neq P_{2r} \end{aligned} \qquad 6.89$$

Therefore the supply pressure should be chosen high enough so that Equation 6.82 is always satisfied. The above discussion is also valid for the controllability of the model reference and feedback linearization controllers.

Defining the first order sliding surface as:

$$\mathbf{S} = \dot{\mathbf{E}} + \lambda \mathbf{E} \qquad 6.90$$

Similar to the first order SMFLC for the quarter car model in Section 6.3.1, if the input is defined as in Equation 6.85 and the sliding surface as in Equation 6.90, the resulted controller is the first order SMFLC.

6.7.4 Parameter Estimator

The algorithm of the parameter estimation based on prediction error was presented in Section 6.4.2. Considering Equations 4.63 and 4.64, the unknown parameters are related to known parameters and variables. Equations 4.63 and 4.64 can be rearranged and put in the form of Equation 6.44 as follows:

$$\overbrace{\begin{bmatrix} \ddot{Z}_s \\ \\ \ddot{\theta} \end{bmatrix}}^{\mathbf{Y}} = \overbrace{\begin{bmatrix} \frac{P_{2f}}{m_s} & \frac{P_{2r}}{m_s} \\ \\ \frac{aP_{2f}}{J} & \frac{-bP_{2r}}{J} \end{bmatrix}}^{\mathbf{W}} \overbrace{\begin{bmatrix} A_f \\ \\ A_r \end{bmatrix}}^{\mathbf{a}} + \overbrace{\begin{bmatrix} -g \\ \\ 0 \end{bmatrix}}^{\Psi} \qquad 6.91$$

Therefore, the bounded forgetting factor least-square estimator estimates the parameters by:

$$\dot{\hat{\mathbf{a}}}(t) = -\mathbf{P}(t)\mathbf{W}(t)\mathbf{e}_1 \tag{6.92}$$

where $\mathbf{e}_1$ is the prediction error vector which is defined as:

$$\mathbf{e}_1 = \mathbf{Y} - \hat{\mathbf{Y}} = \begin{bmatrix} \ddot{Z}_s - \hat{\ddot{Z}}_s \\ \\ \ddot{\theta} - \hat{\ddot{\theta}} \end{bmatrix} \tag{6.93}$$

and $\mathbf{P}(t)$ is a diagonal gain matrix updated by Equations 6.50 and 6.51.

6.7.5 Simulation and Results

The First order SMFLC with estimator is applied to the half car model with pneumatic suspension. The volumes of air springs are estimated by constant volumes equal to 4 in^3. It is also assumed that sensors read the displacements with 0.2 inches error.

The gain matrix $\boldsymbol{K}$ should be chosen to avoid saturation and improve the controller performance. Since the centre of mass is closer to the rear axle, the rear actuator needs a higher effort to control the system. In other words, the saturation is more possible for high gains in the rear valve than the front one. Thus, the gain corresponding to the rear valve should be taken smaller to avoid saturation. The sliding gain of the front actuator is chosen to be twice the gain used for the quarter car model and the sliding gain of the rear actuator is chosen smaller than that. The sliding mode gain matrix is as follows:

$$\mathbf{K} = \begin{bmatrix} 20000 & 0 \\ 0 & 100 \end{bmatrix}$$

The sign function is substituted by a saturation function and the boundary layer thicknesses of heave and pitch angle are taken 10 and 2 respectively. The triple pole λ is considered 10. The ISO class D road is chosen as the road profile. The simulation of the road profile is explained in Section 6.2. Figure 6.26 shows the heave displacement and

pitch angle of the half car model with pneumatic suspension controlled by first order SMFLC. Based on the MPR value, the suspension offers a very good ride comfort.

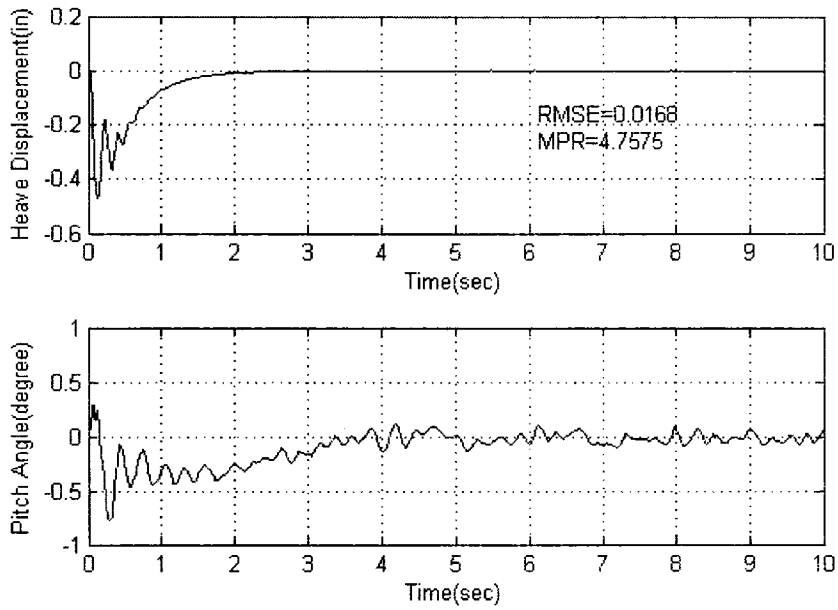

Figure 6.26: The heave and pitch angle of the half car model Controlled by a first order SMFLC with estimator

Figure 6.27 shows the front and rear tire load variations. Since the centre of mass is close to the rear axle the rear tire force is larger than the front one.

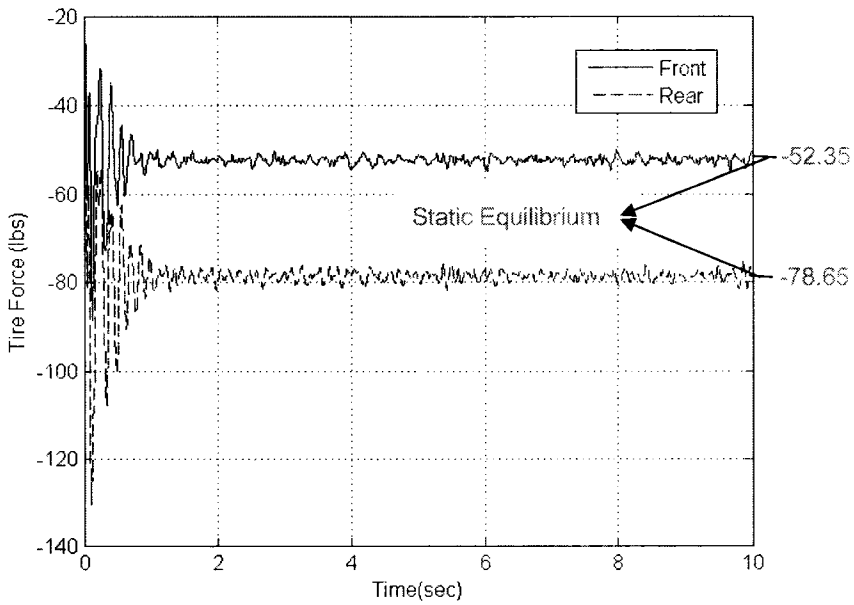

Figure 6.27: The front and rear tire load variations

Figure 6.28 shows the actuator efforts required to control the system. Even though the sliding gain of the rear actuator is smaller than that of the front one, the rear actuator effort

is larger than the front one. Therefore, the rear air spring needs a larger control valve than the front one.

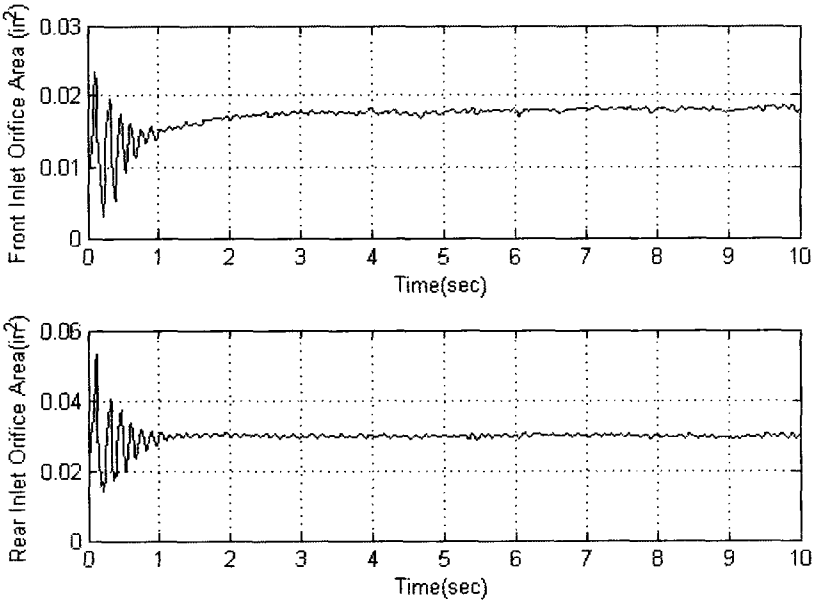

Figure 6.28: The front and rear inlet orifice areas

The real and estimated effective areas of the front and rear air springs are shown in Figure 6.29. The figure shows in the present of uncertainty the estimator can estimate the parameter very well. The root mean square of the prediction error is calculated after 1 sec and is very small.

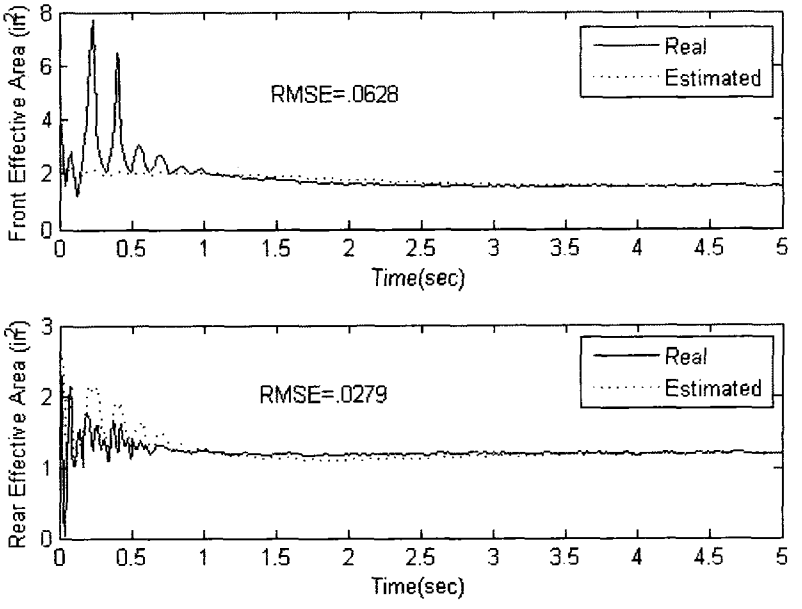

Figure 6.29: The Estimated and real effective areas of front and rear air springs

As was explained before, the controller should be designed based on the maximum mass capacity of the vehicle. Figure 6.30 shows the control performance in the presence of payload uncertainty. It is assumed that the maximum capacity is twice the mass of the car body. The RMS of the heave acceleration in the presence of the payload uncertainty is almost the same as before, and the controller is robust to the payload uncertainty.

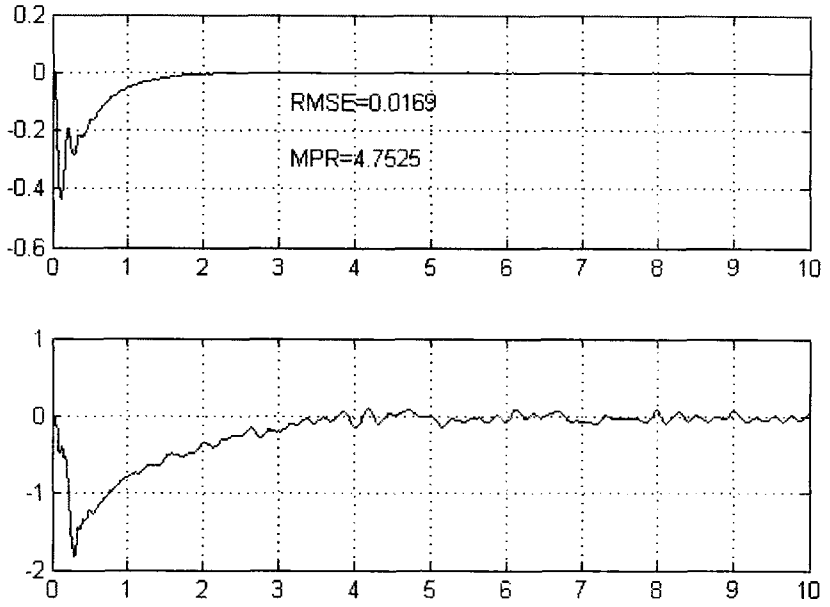

Figure 6.30: The pitch angle for first order SMFLC in the presence of payload uncertainty

Figure 6.31 shows the front and rear tire load variation in the presence of payload uncertainty. Comparing Figures 6.27 and 6.31 implies that the tire load variations remain almost the same in the presence of the payload uncertainty.

Figure 6.32 shows actuator efforts in the presence of the payload uncertainty. The front and rear inlet orifice areas increase in the presence of payload uncertainty. Similar to quarter car model, a higher actuators effort is demanded as the payload increases. To solve this problem either a higher supply pressure is required or a valve with larger capacity should be used.

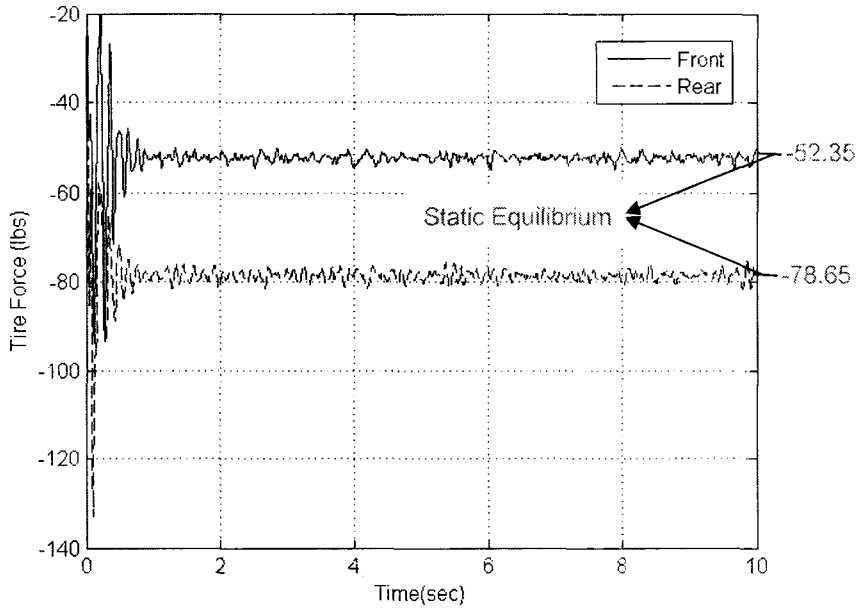

Figure 6.31: The front and rear tire load variations in the presence of payload uncertainty

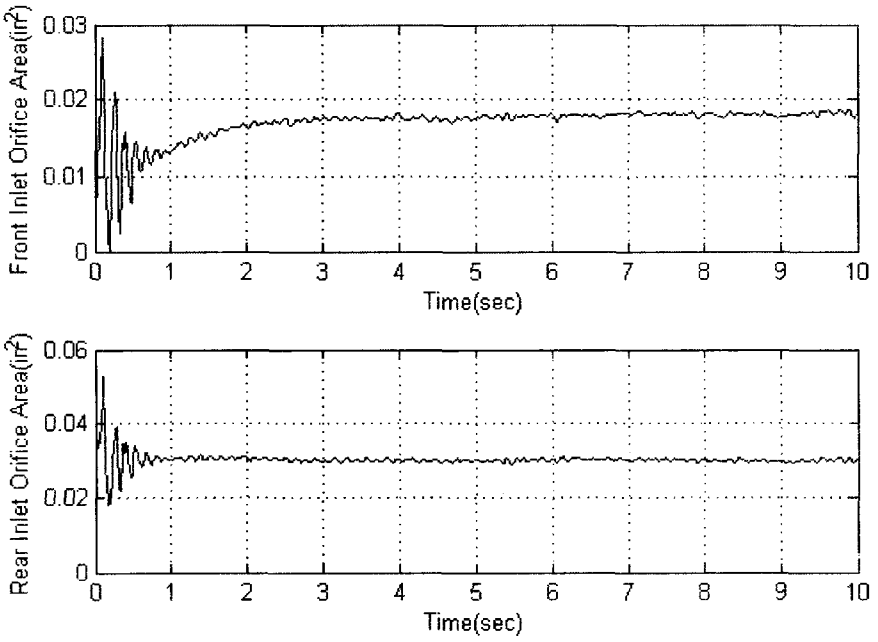

Figure 6.32: The front and rear orifice areas in the presence of different uncertainties

Figure 6.33 shows the estimated and real effective areas. Similar to the quarter car model, since the effective area and sprung mass appear in mathematical model as a ratio, their uncertainties compensate each other.

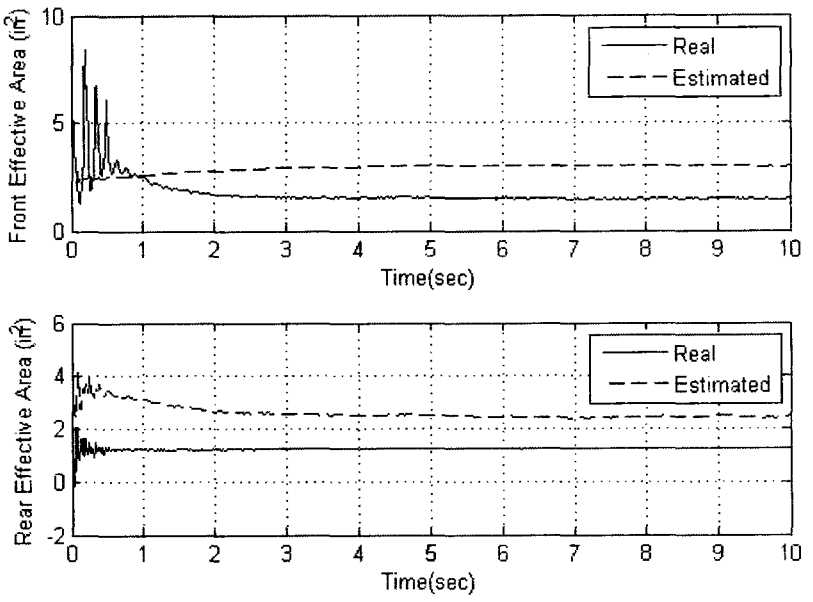

Figure 6.33: The real and estimated effective areas in the presence of the payload uncertainty

CHAPTER 7

Conclusion and Recommendations

7.1 Conclusion

In this thesis, dimensional analysis was used to design a similitude model of a half car model with conventional suspension. The dimensional analysis showed that in order to have a similitude scaled model, the scale factors of the mass, the stiffness and the damping coefficient must be the same and independent of the scale factor chosen for the length. The scale factors of stiffness, mass and damping coefficient are chosen to be 12, and the scale factor of the length is 5. Using these scale factors, a scaled half car model of the Honda Civic is obtained. The Firestone Model 2M2A Airmount air spring is found to be the most suitable one for this scaled model and was used in the pneumatic suspension system.

The dimensional analysis on the quarter and half car models with pneumatic suspension showed that, in order to have a similitude model, the scale factor of the valve orifice area must be chosen based on the scale factor of length as shown by Equation 4.45. The scale factor of the pressure is the ratio of the mass and length scale factors. If the air spring stiffness is used to design a similitude model, the scale factor of the air spring stiffness and that of the mass must be kept equal. This is the same relationship obtained for the similitude model of the conventional half car model.

Results from static experiments showed that the behaviour of the air spring effective area is different from that of the mean cross section area. For a given height, the air spring mean cross section increases while the effective area decreases. The air spring effective area is the subtraction of two terms. The minuend is the effective projected area and increases slightly with an increase in pressure. The subtrahend is a term introduced by the y-component of the force applied to the payload by the air spring bellows. This term increases with the air spring pressure and results in a total decrease of the effective area.

The frequency response of an experimental air spring system showed that the natural frequency increases with the air spring pressure and with an increase in the applied load Two peaks appear on the magnitude curves. The major peak corresponds to the natural frequency of the system while the frequency of the second peak is independent of the payload and pressure. The second peak is the result of the folding and unfolding behaviour of the bellow's composite material. The Bode diagrams indicate that the behaviour of the system is similar to that of a second order one with a zero phase shift at very small frequencies and a phase shift of π at very large ones. A system identification analysis was performed and the results show that the natural frequency changes by 4 to 6 Hz for a specific payload, proving that a quasi-linear model cannot accurately represent the air spring. There is a slight increase in the system's damping ratio as the pressure increases

Comparing the frequency responses obtained using the mathematical model with those of the experimental air spring/load system shows good agreement between them. Therefore, the nonlinear mathematical model can represent the behaviour of an air spring for different pressures. The sensitivity analysis shows that the air spring model is sensitive to the effective area. The model sensitivity to the thermodynamic process is small. The analysis shows that the natural frequency of the air spring changes with the excitation amplitude.

Different nonlinear controllers were applied to the quarter car model with pneumatic suspension. Feedback Linearization Control (FLC) is applied to the quarter car model with a pneumatic cylinder. The sensitivity curves show that FLC offers a good ride comfort in the presence of the effective area uncertainty if the magnitude of the triple pole is larger than 5 and the estimation error of effective area is smaller than 1.5 in^2. FLC on the quarter car model with an air spring also results in good ride comfort for a triple pole larger than 6 in the presence of effective area uncertainty. The rise time, however, was found to be large for a triple pole smaller than 10. As the triple pole increases, ride comfort and the performance improves and the actuator effort increases. When a volume uncertainty exists the system performance worsens. The general performance of the model reference feedback linearization (MRFLC) was found to be very similar to that of the FLC.

Different types of sliding mode controllers were applied to the quarter car model with pneumatic suspension. Their performances were compared. The third order integral SMFLC has a large overshoot and the third order sliding mode feedback linearization

(SMFLC) has a non zero steady state error. The first order SMFLC results in a better ride comfort and a good performance when compared to other controllers used in this research. The sensitivity curves of the first order SMFLC show that this controller also results in a good ride comfort in the presence of different uncertainties. The sensitivity of the system to the triple pole value decreases. The performance and ride comfort improves by increasing the sliding gains and boundary layer thickness.

The least-square estimator was used to estimate the effective area of the air spring with a good convergence and resulted in a decrease in model uncertainties. The estimator also improves the performance of the system considerably. Ride comfort gets close to its largest possible value. The oscillation and rise time decrease considerably. The sensitivity curves show that the sensitivity to the magnitude of the triple pole λ decreases considerably. The analysis of the estimator algorithm shows that the effective area and the sprung mass uncertainties compensate each other if the controller is designed based on the maximum payload capacity of the car. The first order SMFLC with least-square estimator also results in a good ride comfort and performance in the presence of the payload uncertainty.

The first order SMFLC with least-square estimators is applied to the half car models with air springs. This controller resulted in a good ride comfort and performance in the presence of different uncertainties. The estimator was able to estimate the effective areas of the front and rear air springs. Since the center of mass is closer to the rear axle, the rear suspension needs a valve with larger orifice than the front one. The performance of the controller in the presence of the payload uncertainty was found to be satisfactory.

7.2 Recommendations for Future Works

- The effective area is the most important and complicated parameter of an air spring. Formulating the effective area in terms of air pressure and geometric parameters of an air spring can be very useful for developing a precise mathematical model of an air spring.
- The simulated controllers can be implemented on the half car model that has been built in this study and their performances can be verified by experiments.

- Adaptive sliding mode controllers result in good performances when they are applied to suspensions with pneumatic cylinders. They need some modification to improve the performance of suspensions with air springs.
- The discussed nonlinear controllers can be applied to a full car model with pneumatic suspension to study the rollover and ride comfort of the pneumatic suspension.

References

[1] Reiher, H. and Meister, F.J., "The Effect of Vibration on People", Published in German in 1931, English Translation in Report No. F-TS-616-R.E.H.Q. Air Material Command, Wright Field, Ohio,1949.

[2] Craig, M. Favor, 1997 "Evaluation of a Floating Aerobics Floor", Master's Thesis submitted to the Faculty of the Virginia Tech.

[3] Janeway, R.N., "Vertical Vibration Limits for Passenger Comfort," SAE Ride Vib. Manual, SAEJ.,6a (1965), 28 p.

[4] Smith, C.C., Mcgehee, D.M., Healey, A.J., "The Prediction of Passenger Riding Comfort from Acceleration Data" Research Report No.16, The Council for Advanced Transportation Studies, The University of Texas at Austin, March 1976.

[5] Hrovat, D., 1997, "Survey of Advanced Suspension Developments and Related Optimal Control Applications." Automatica, 33(10), pp. 1781–1817.

[6] "A Guide to the Evaluation of Human Exposure to Whole Body Vibration," ISO/DIS 2631, International Organizaition for Standardization, New York, 1972.

[7] Genta, G, "Motor Vehicle Dynamics: Modeling and Simulation", World Scientific, 1996.

[8] A.J.Healey, "Digital Processing of Measure Vibration Data for Automobile Evaluation", The Proceeding of the Design Engineering Technical Conference, Chicago, Illinois,Sept. 26-28, 1997, pp. 45-53.

[9] ElBeheiry, EM, Karnopp, D., ElAraby, ME, and Abdelraaouf, AM, 1995, "Advanced Ground vehicle Suspension Systems-A Classified Bibliography." Vehicle System Dynamics, 24, 231-258, 1995.

[10] Wong, J.Y., 1993. "Theory of Ground Vehicles." John Wiley & Sons Ltd, New York.

[11] Smith, R.E. and D.R., Sigman (1981). "Experimental verification of linear rigid body model", Ford Motor Company Research Report, Dearborn.

[12] Sharp, R. S., and Crolla, D.A., "Road vehicle suspension system design - a review", 1987, Vehicle System Dynamics, 16 (1987), pp. 167-192

[13] Ryba, D., "Improvement in dynamic characteristics of automobile suspension systems (Part I Two-mass systems)" , Veh.Sys.Dyn., 3, 1974, 17-46

[14] Sharp, R.S. and Hassan, S.A.: "The fundamental of passive automotive suspension system design", Society of Environmental Engineers Conference on Dynamics in Automotive Engineering, 1984, 104-115.

[15] Thompson, A.G., "Optimum damping in a randomly excited non-linear suspension", Proceedings of the Institution of Mechanical Engineers, 184 (2A), 1969-70, 169--184.

[16] Sharp,R.S. and Hassan, S.A., "An evaluation passive automotive suspension systems with variable stiffness and damping parameters" Veh.Sys.Dyn., 15, 1986, 335-350.

[17] Sharp, R.S. and Hassan, S.A.: "The relative performance capabilities of passive, active and semi-active car suspension systems", Proceedings of the Institution of Mechanical Engineers, 200, D3, 1989, 219-228.

[18] Segal, L. and Lang, HH, "The Mechanics of Automotive Hydraulic Dampers at High Stroking Frequencies", Vehicle Syst. Dyn. 10 (1981), pp. 82–85.

[19] Yabuta, K., Hidaka, K. and Fukushima, N. "Influence of Suspension Friction on Riding Comfort", Swets Publishing Service, Cambridge University, pp. 181-193, 1981.

[20] Thompson, A. G., "An Active Suspension with Optimal Linear State Feedback ", Vehicle System Dynamics, 5, 187--203 (1976).

[21] D.Karnopp, "Theoretical limitations in active suspension.", Vehicle system Dynamics, 15:41--54, 1986.

[22] D.Karnopp, "Are Active Suspension Really Necessary", ASME Paper No. 78, WA/DE-12, 1978.

[23] Karnopp, D.C., "Active and Semi-Active Vibration Isolation," Journal of Vibration and Acoustics, Vol. 117, No. 3b, 1995, pp.177--185

[24] Karnopp, D.C., Crosby, M.J., and Harwood, R.A., 1974, "Vibration control using semi-active force generation," ASME Journal of Engineering for Industry, 96(2): 619–626.

[25] R. D. Cavanaugh, "Air suspension and servo-controlled isolation systems", 1961, Shock and Vibration Handbook, Volume 2 (editors C. M. Harris and C. E. Crede), New York: McGraw-Hill, Chapter 33.

[26] R. A. WAILER and P. P. BENHAM, "Fatigue machine mounted on air springs", 1963 Engineering, Lond. 195,338.

[27] J.I.SOLIMAN and D. TAJER-ARDABILI 1966 " Self-damped pneumatic isolator for variable frequency excitation", Journal of Mechanical Engineering Science 8, 284-293.

[28] D.GEE-CLOUGH and R.A.WALLER, "An improved self-damped pneumatic isolator", Journal Sound and Vibration 8, 364-376, 1968.

[29] E.Esmailzadeh, "Compact self-damped pneumatic isolators for road vehicles", Transactions of the American Society of Mechanical Engineers, Journal of Mechanical Design 102, 1980, 270-277.

[30] M.S.Hundal "Passive pneumatic shock isolator: Analysis and design", Journal of Sound & Vibration, Vol 84, No 1, 1982, 1-9.

[31] Bachrach BI, Rivin E. "Analysis of a damped pneumatic spring", J Sound Vib. 1983; 86:191–197.

[32] Katsuya Toyofuku, Chuuji Yamada, Toshiharu Kagawa, Toshinori Fujita, "Study on Dynamic Characteristic analysis of Air Spring with Auxiliary Chamber", JSAE Review, 20, 349~355 (1999).

[33] Quaglia, G. and Sorli, M.: "Experimental and theoretical analysis of an air spring with auxiliary reservoir", Proc. of the 6th Internationales Symposium on Fluid Control Measurement and Visualization (FLUCOME 2000), Sherbrooke, Canada, August 2000.

[34] G.Quaglia, M.Sorli, et al., "Air suspension dimensionless analysis and design procedure", Vehicle System Dynamics, 2001,55(6):443-475.

[35] T.Takagami and Y.Jimbo, Study of an active vibration isolation system . Precision Engineering, Volume 10, Issue 1, January 1988, Pages 3-7.

[36] Winfred K.N.Anakwa, (Dept. of Elec. and Comp. Eng., Bradley University); Thomas, Dion R.; Jones, Scott C.; Bush, Jon; Green, Dale; Anglin, George W.; Rio, Ron; Sheng, Jixiang; Garrett, Scott; Chen,Li, "Development and control of a prototype pneumatic active suspension system", IEEE Transactions on Education, v 45, n1, February, 2002, p 43-49.

[37] J.Xiao, B.T.Kulakowskf, "Sliding Mode Control of Active Suspension for Tansit Buses Based on A Novel Air Spring Model", Proceeding of the American Conference, Denver, June 4-6, 2003

[38] Galilei, Galileo, "Two New Sciences", (page 62) available at http://galileoandeinstein.physics.virginia.edu/tns61.htm

[39] Schuring, Dieterich J. 1977 "Scale models in engineering: fundamentals and applications", Oxford ; New York : Pergamon press, c.

[40] E. Szucs, Similitude and Modeling, Elsevier Scientific Publishing Company, NY; 1980

[41]] Victor J. Skoglund, 1967"Similitude : theory and applications "Scranton, Pa. : International textbook Co.,

[42] Murphy, Glenn. 1950 "Similitude in engineering", New York, Ronald Press Co.

[43] Greg Wilson, Canadian Driver (Canada's online magazine) April 30, 2004 http://www.canadiandriver.com/testdrives/04civic_si.htm

[44] Firestone Airstroke™ / Airmount™ Literature "Engineerin manual & Design Guide", http://www.firestoneindustrial.com/Industrial/Literature/Airstroke_Airmount /EMDG.pdf

[45] Firestone Airstroke™/Airmount™ Technograms, No116, "Hydraulic and Pneumatic Cylinder Crossovers", "http://www.firestoneindustrial.com/Industrial Technigrams /116_Tech.pdf"

[46] B. W. Anderson, "The Analysis and Design of Pneumatic Systems", New York: JohnWiley & Sons, Inc., 1976.

[47] Pan, T.C., Mita, A. and Li, J., "Vehicle-Induced Floor Vibrations in a Multistory Factory Building'', J. of Performance of Constructed Facilities, American Society of Civil Engineers, Vol. 16, No. 2, pp. 54 – 61 (2001).

[48] Lu Sun, " Simulation of pavement roughness and IRI based on power spectral density," Mathematics and Computers in Simulation, Volume 61, Number 2, 1 January 2003, pp. 77-88.

[49] Levant, A., "Universal single-input-single-output (SISO) sliding-mode controllers with finite-time convergence", Automatic Control, IEEE Transactions on Volume 46, Issue 9, Sept. 2001 Page(s):1447 – 1451.

[50] Jean-Jacques E.Slotine., "Applied Nonlinear Control", Prentice-Hall, Englewood Cliffs, New Jersy, 1 edition, 1991.

[51] Smaoui, M., Brun, X., Thomasset, D., "A Robust Differentiator-Controller Design for an Electropneumatic System", Proceedings of the 44th IEEE Conference on Decision and Control, and the European Control Conference 2005, Seville, Spain, December 12-15, 2005.

Appendix A

Engineering Drawings of the Honda Civic Half Car Model

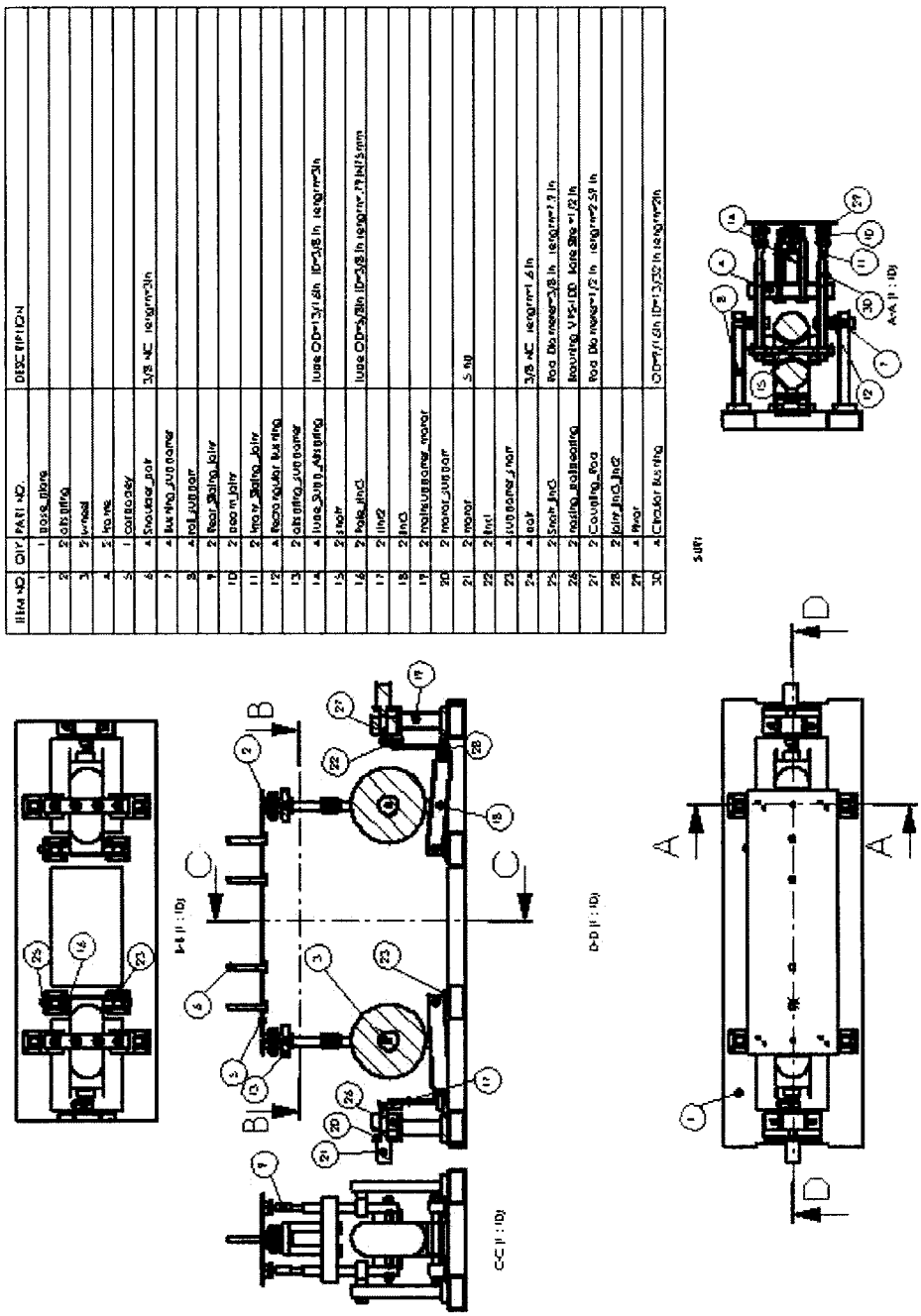

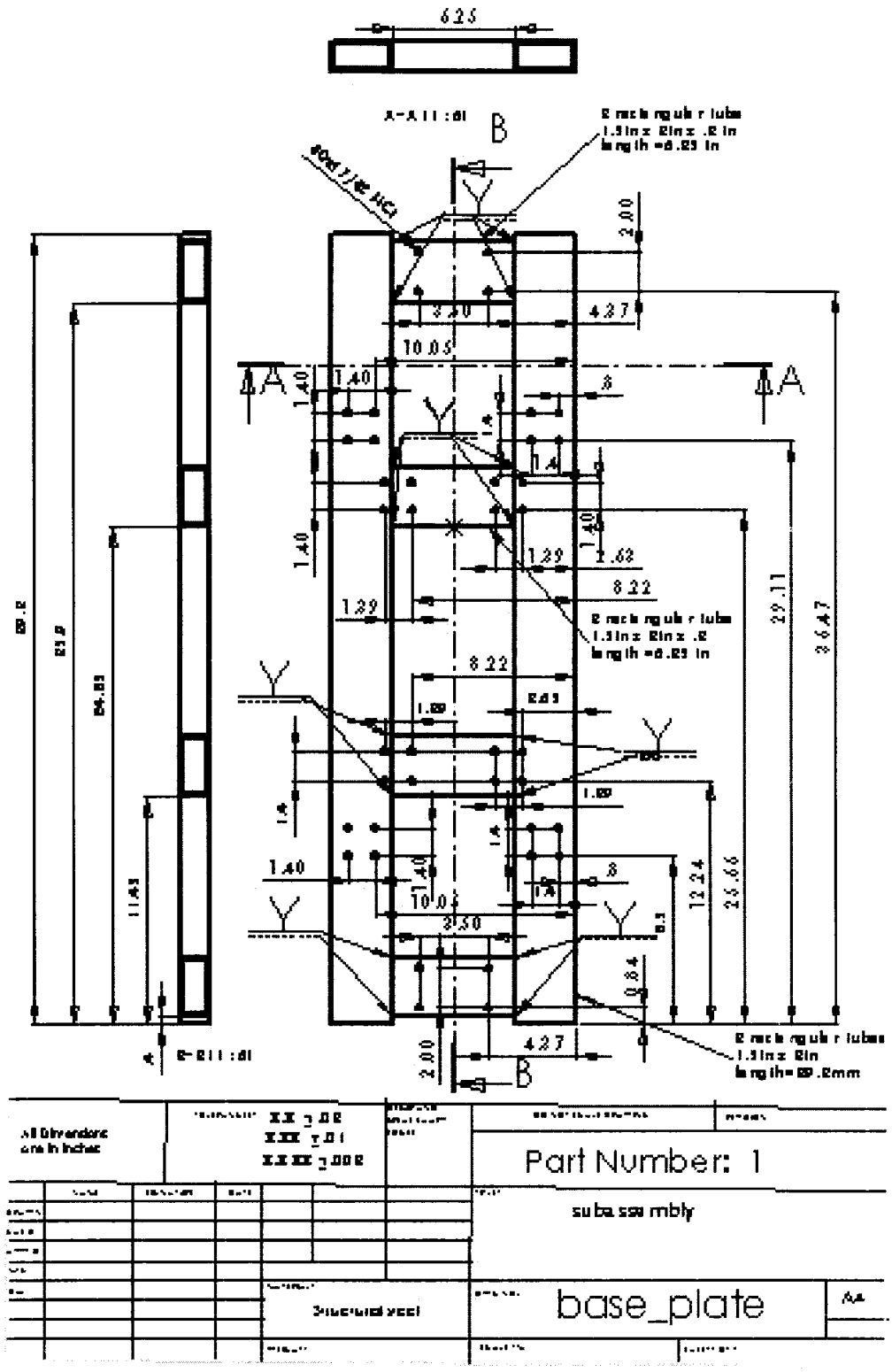

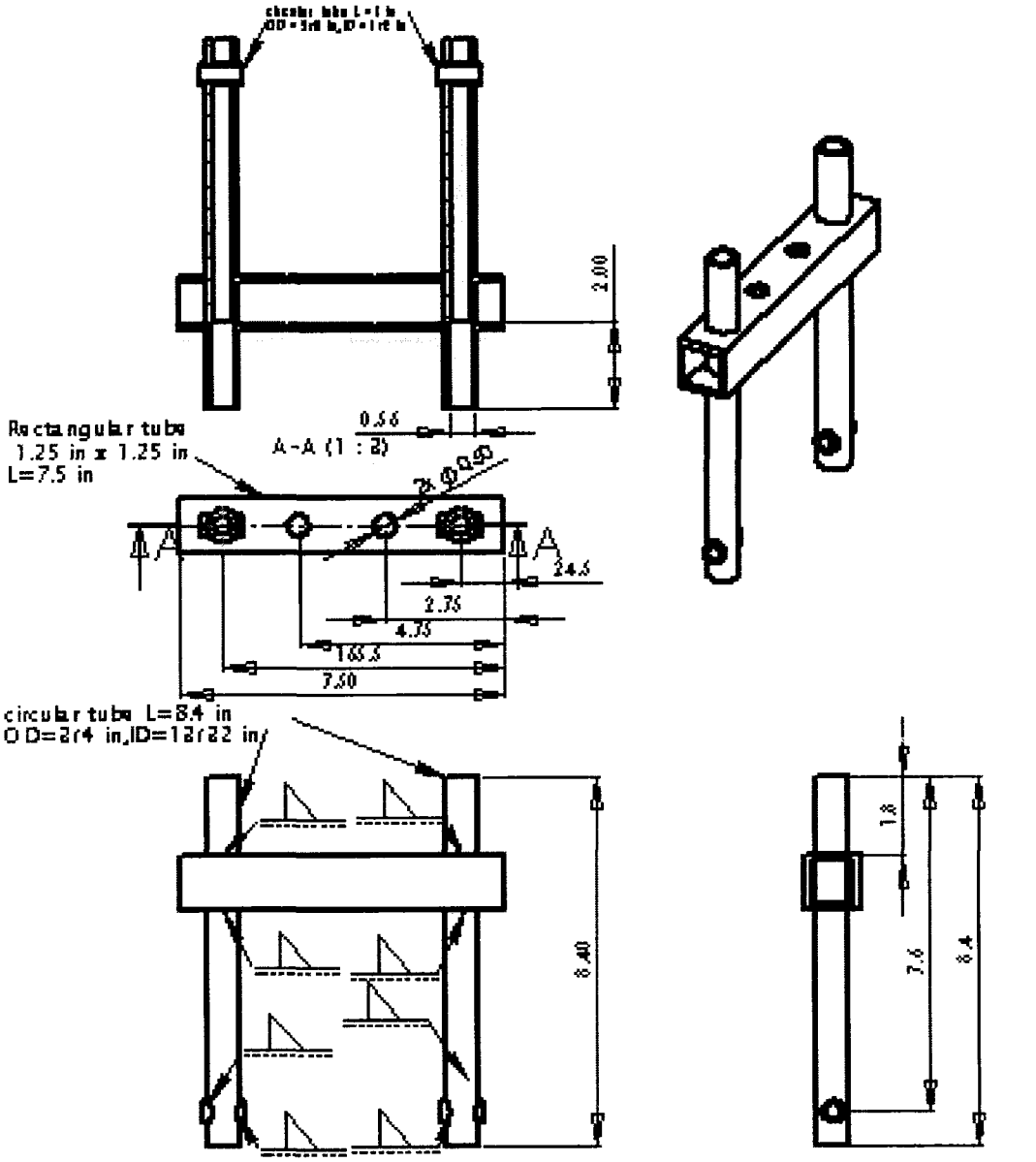

All Dimensions are in Inches	XX ±.02 XXX ±.01 XXXX ±.005		Part Number: 4
	Structural Steel Cold Finish Steel		Frame

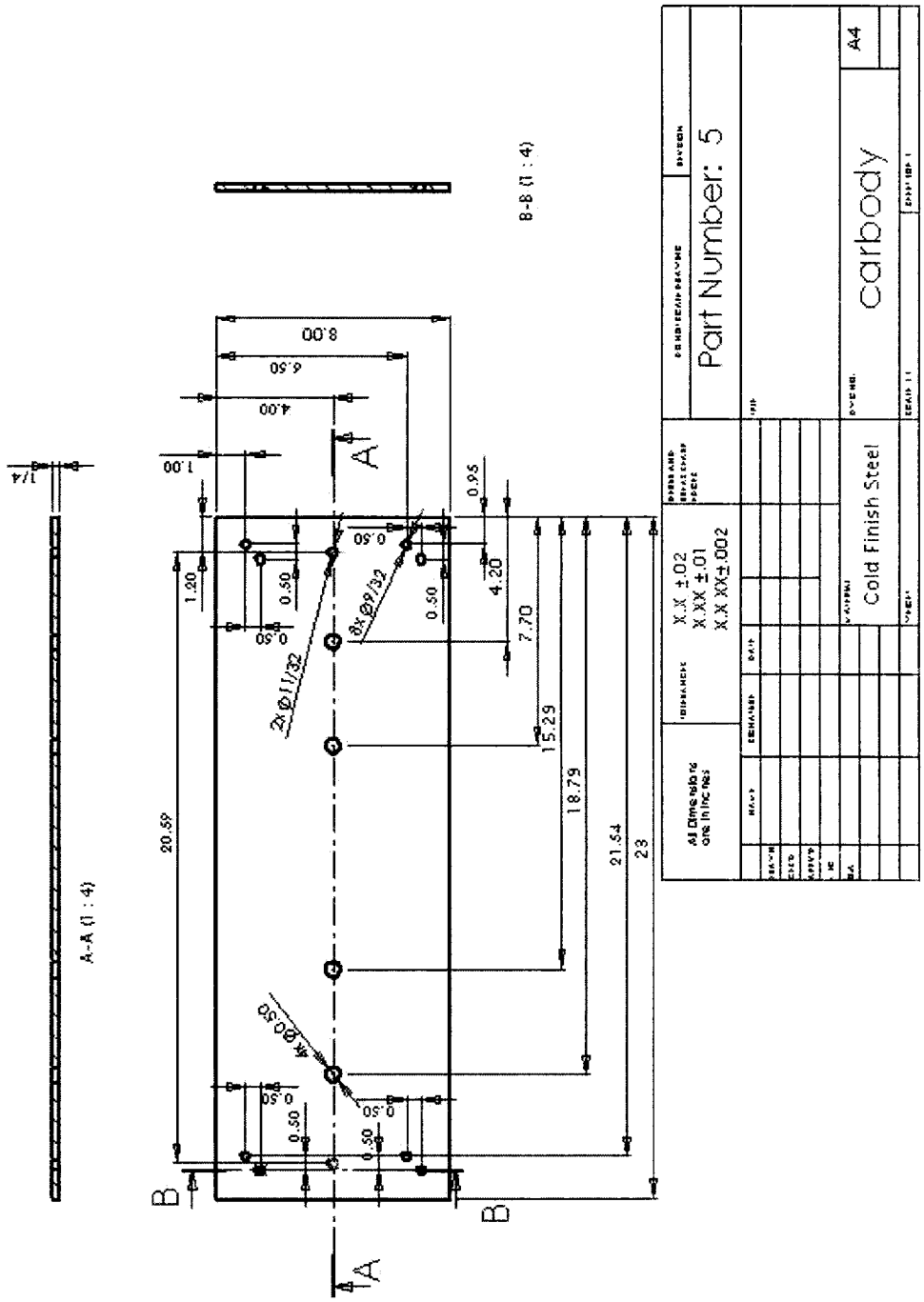

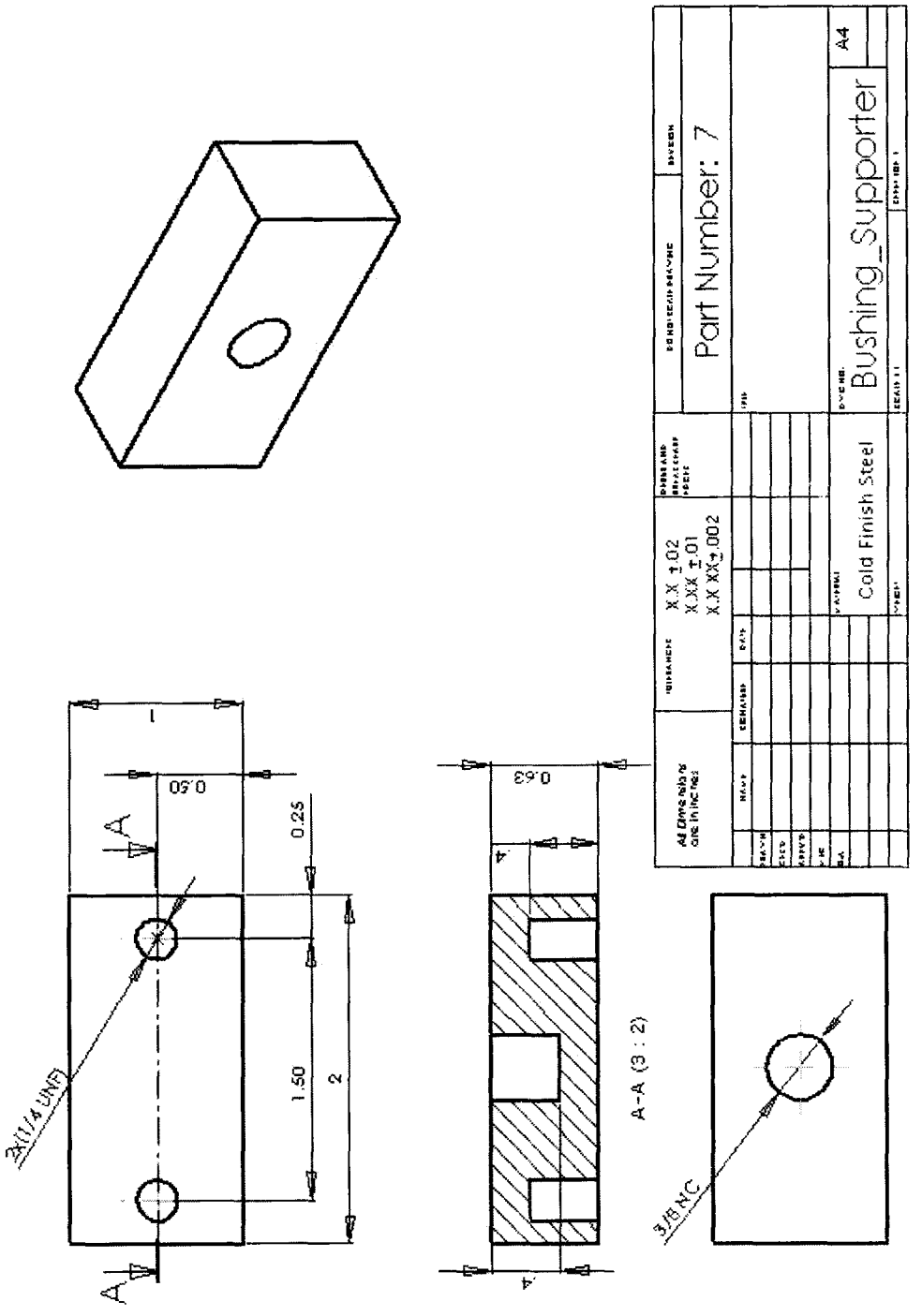

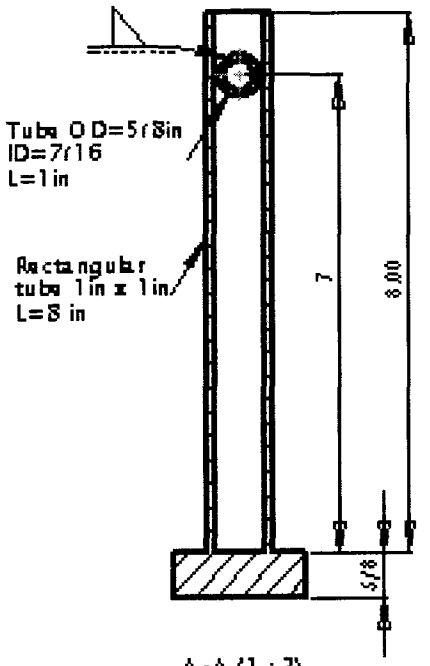

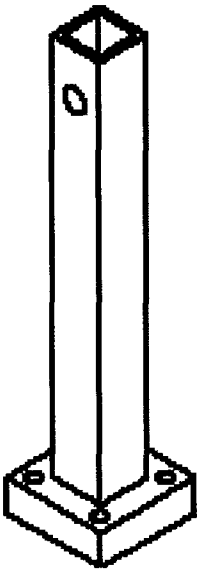

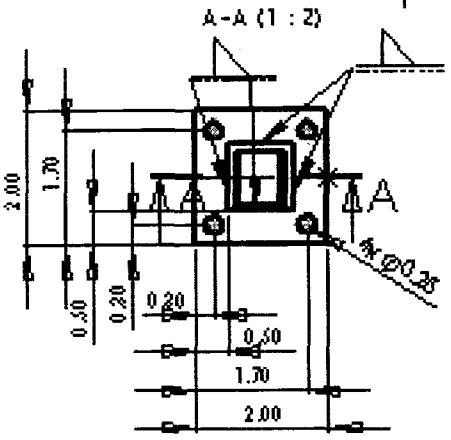

			Part Number: 8
			subassembly
	Cold Finish Steel		Rail_Suppor

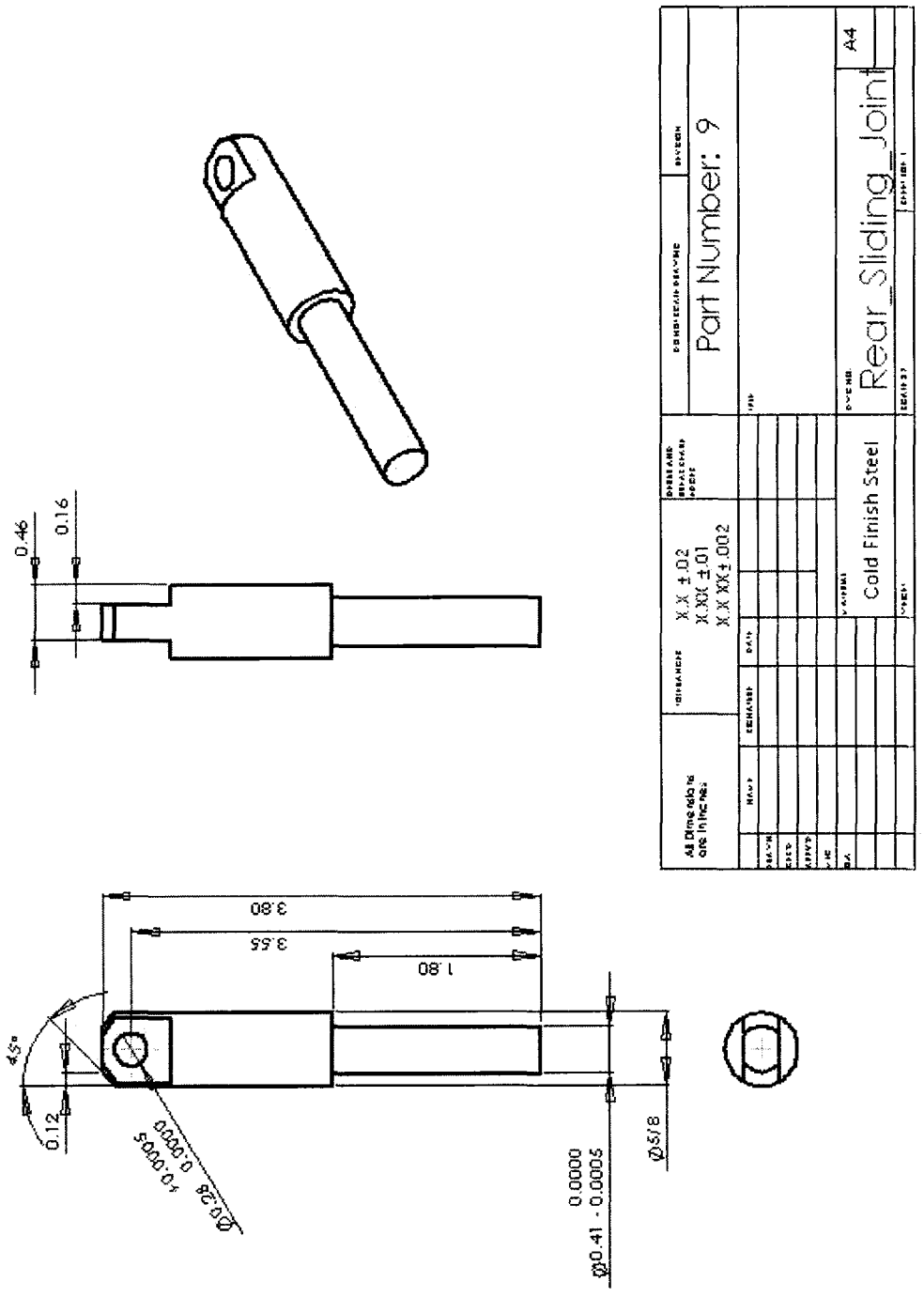

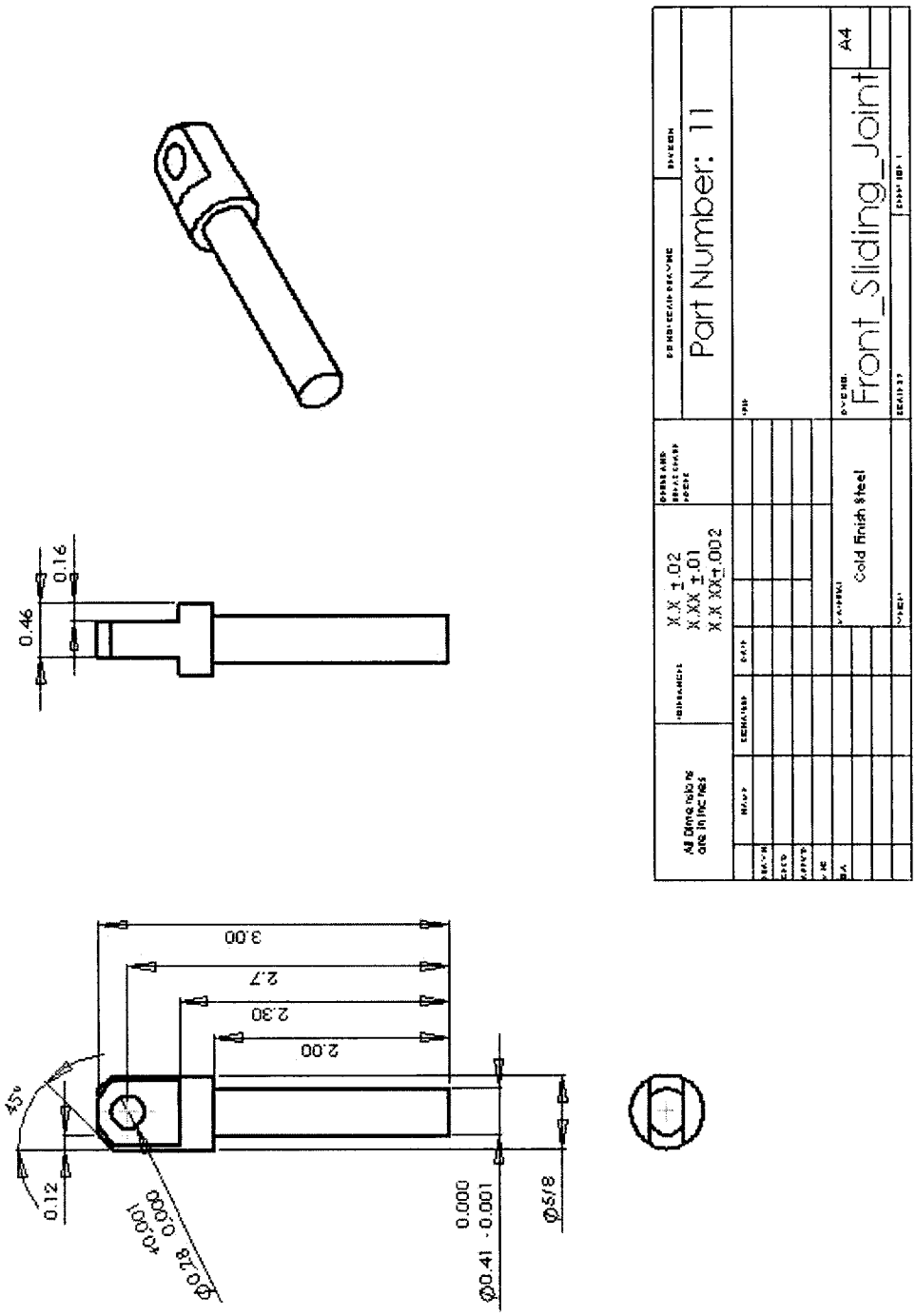

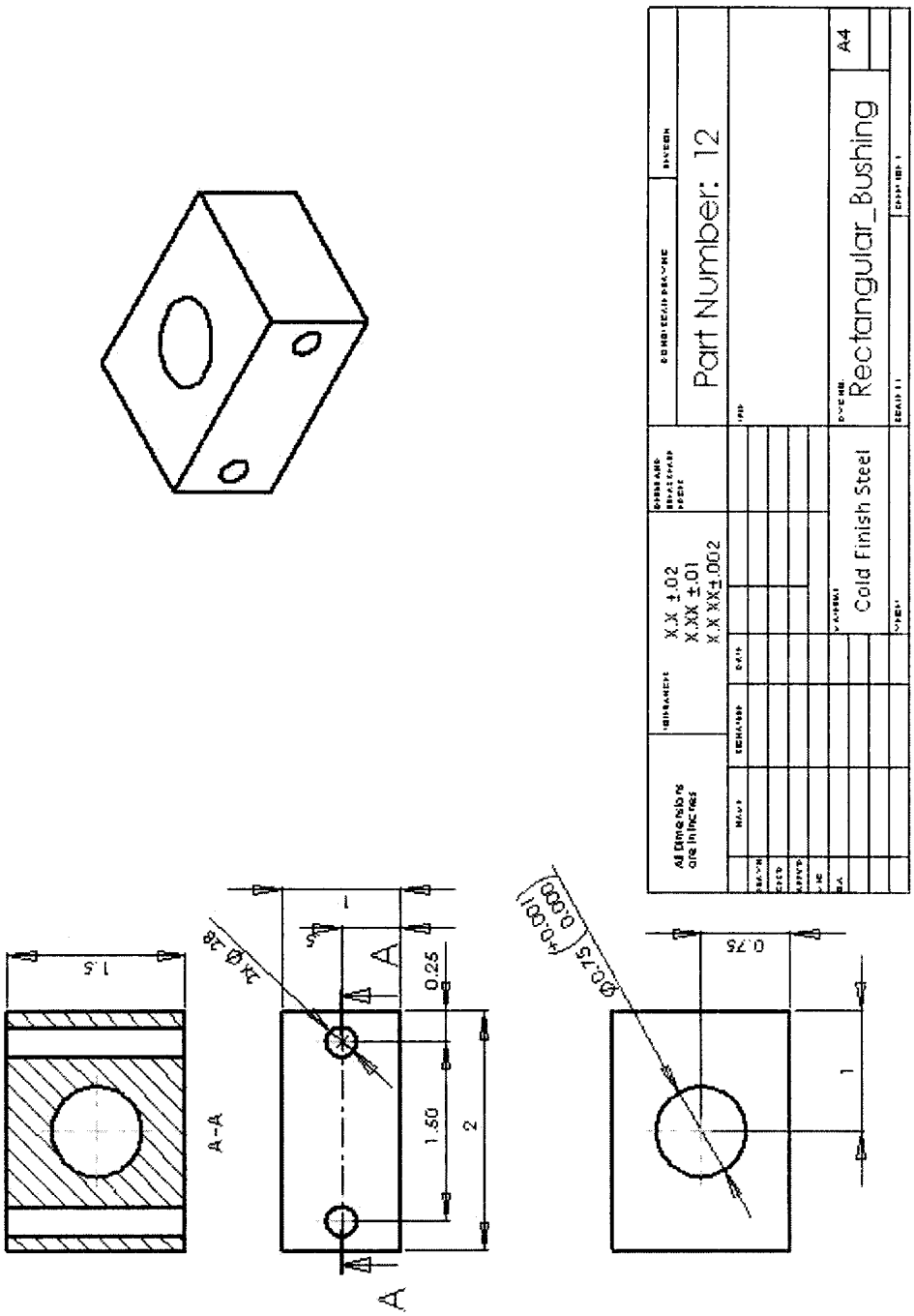

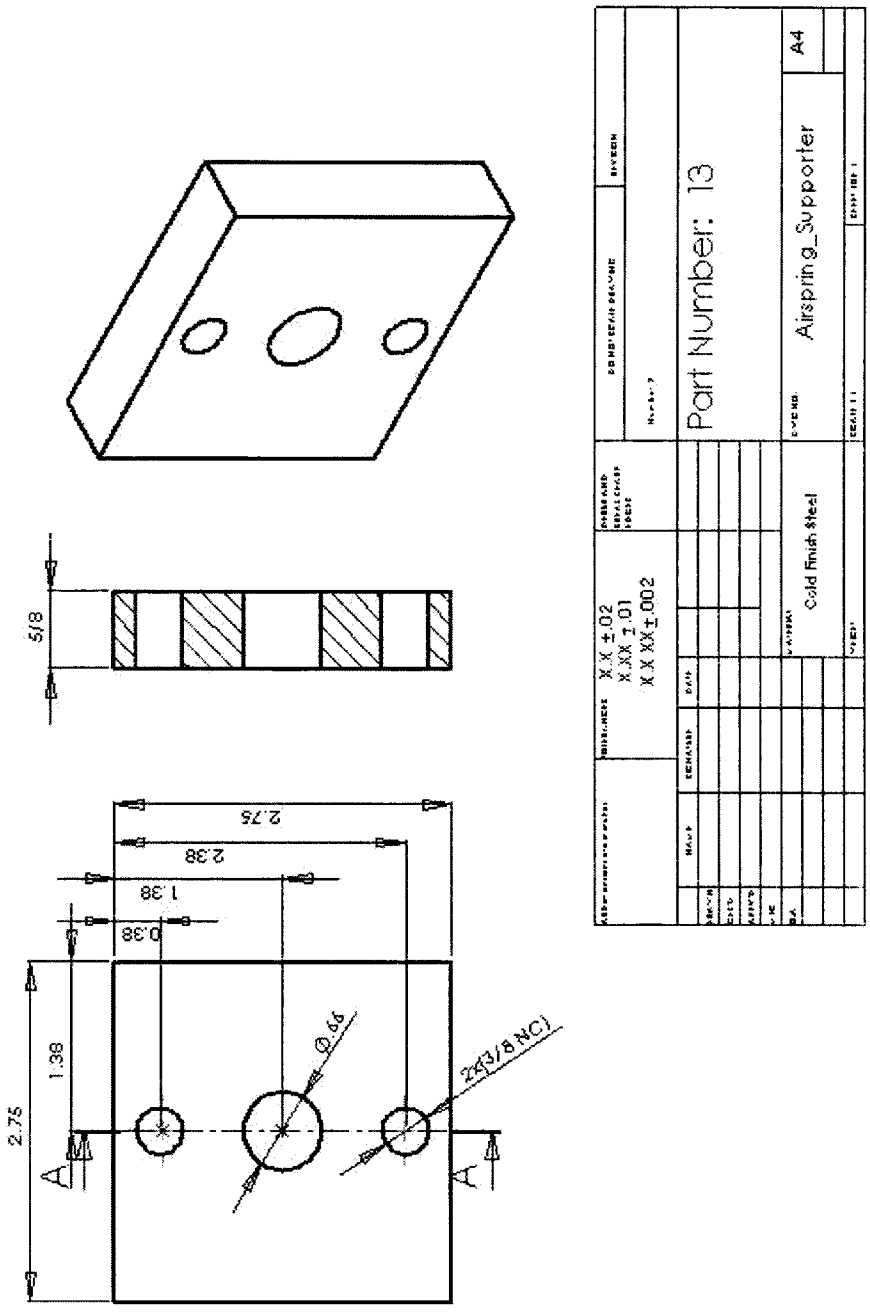

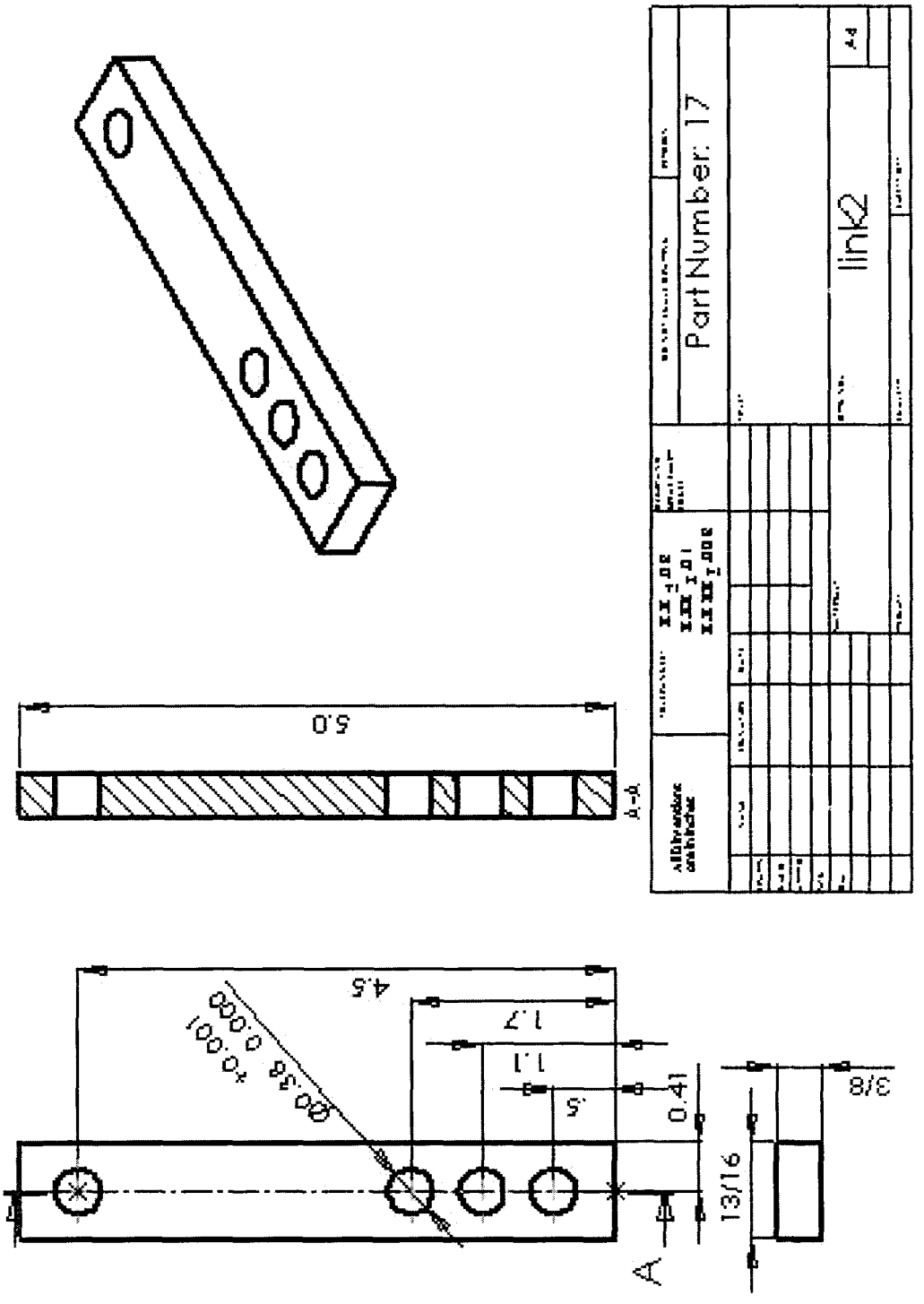

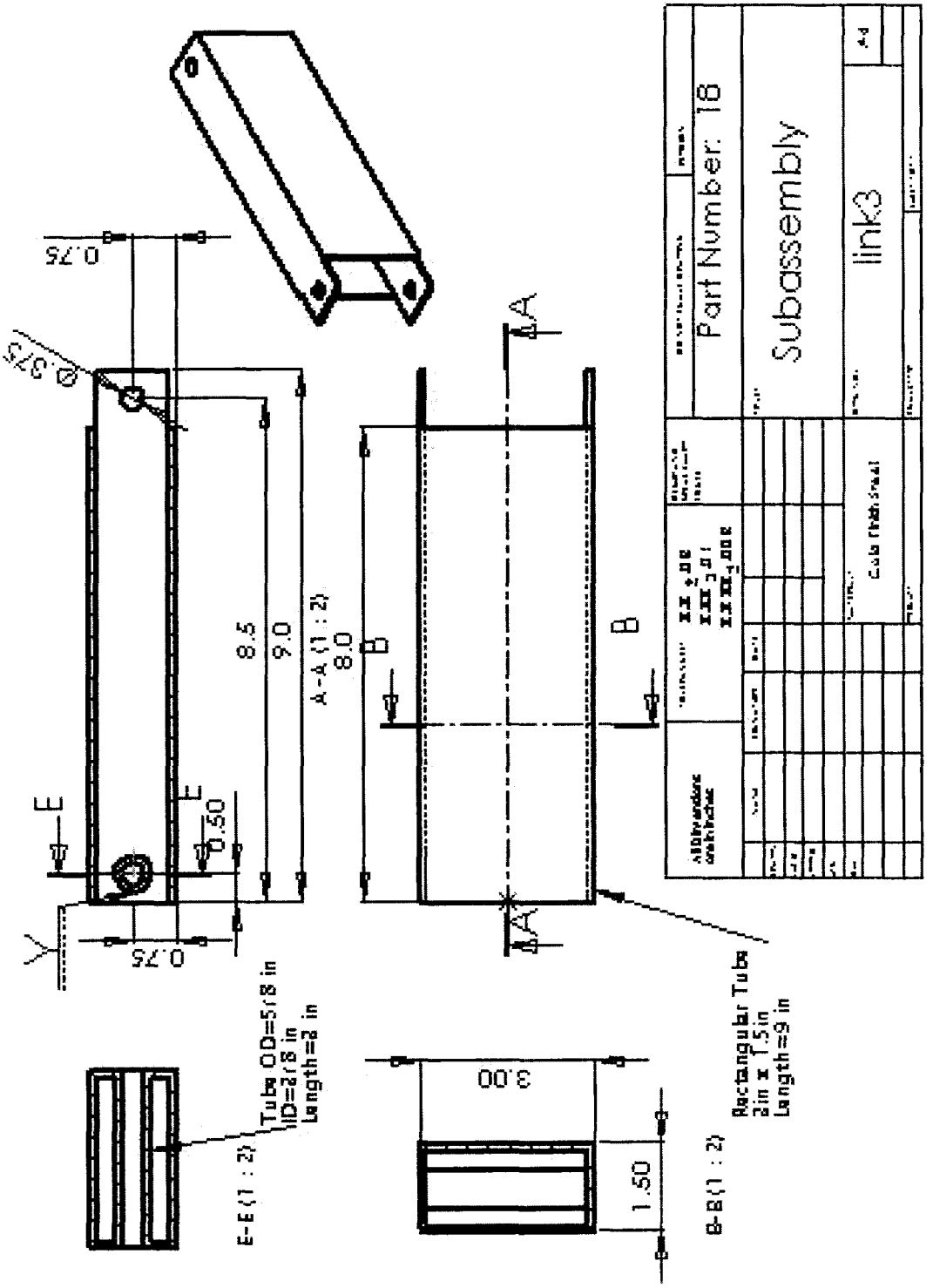

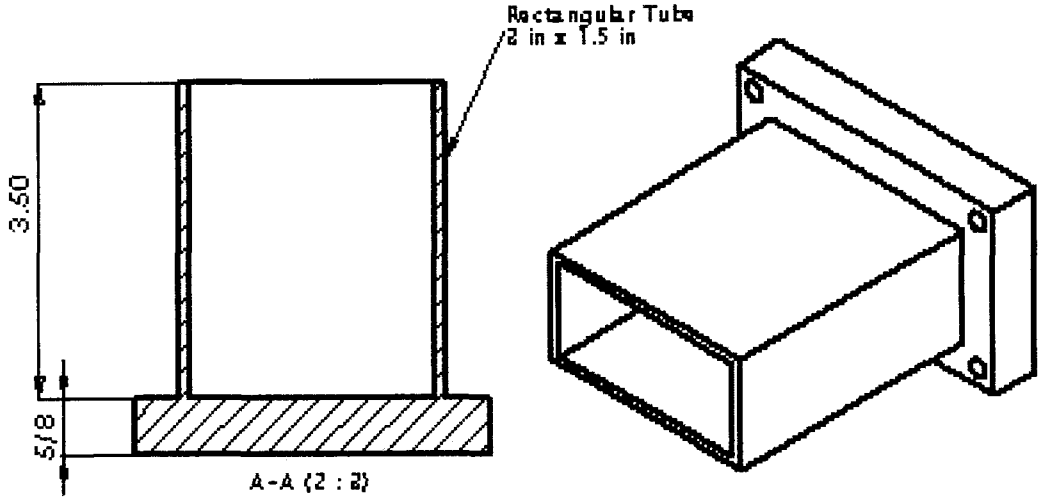

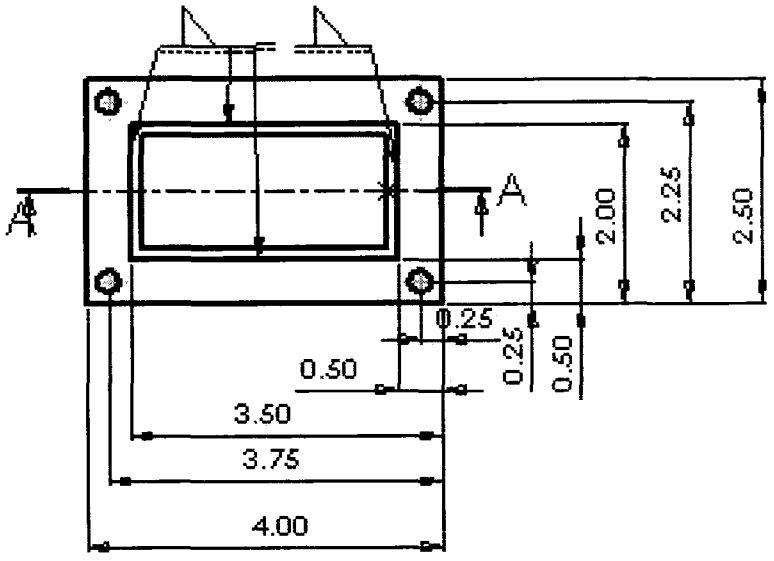

Part Number: 19

subassembly

Cold finish Steel

mainsupporter_motor

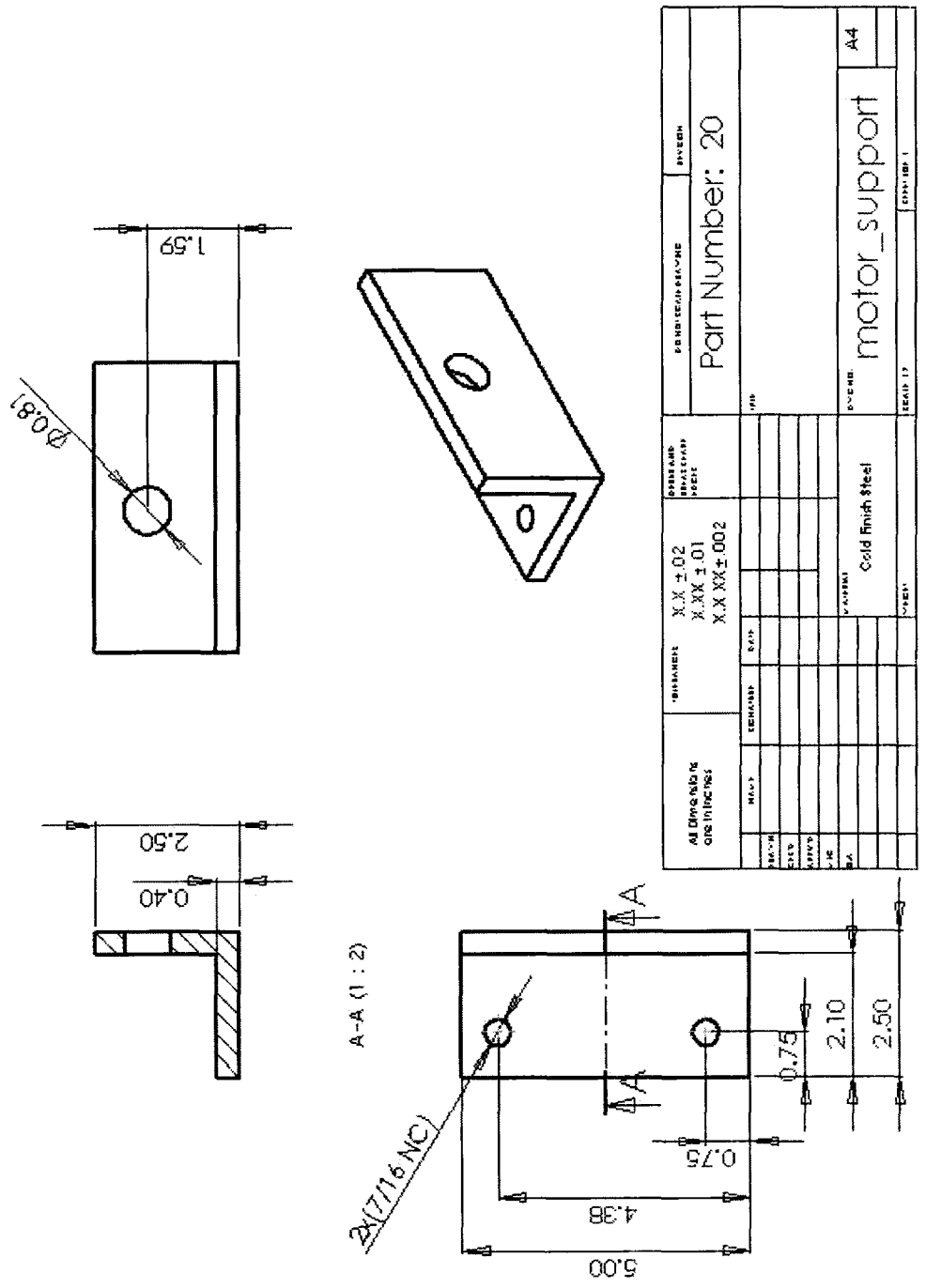

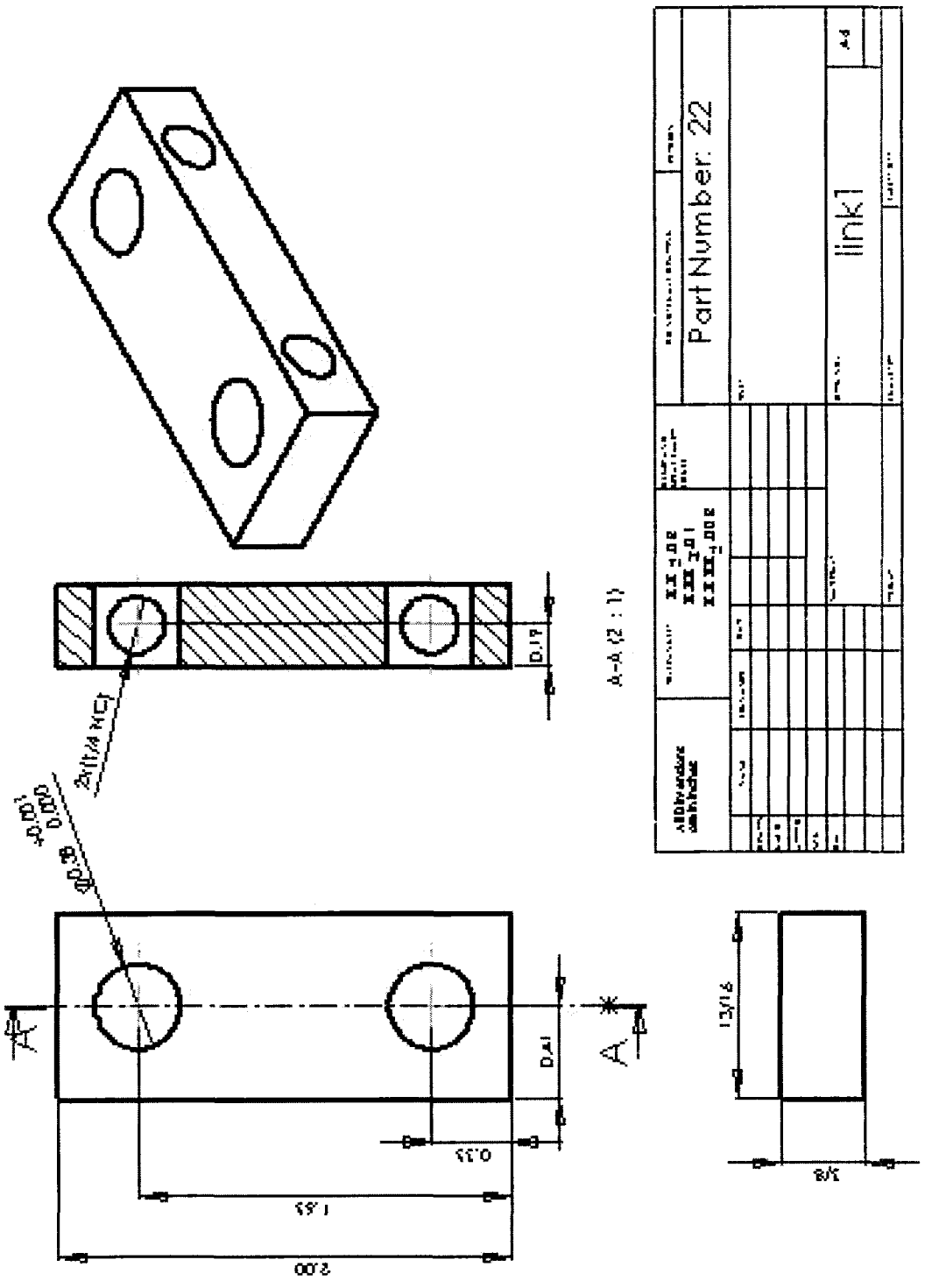

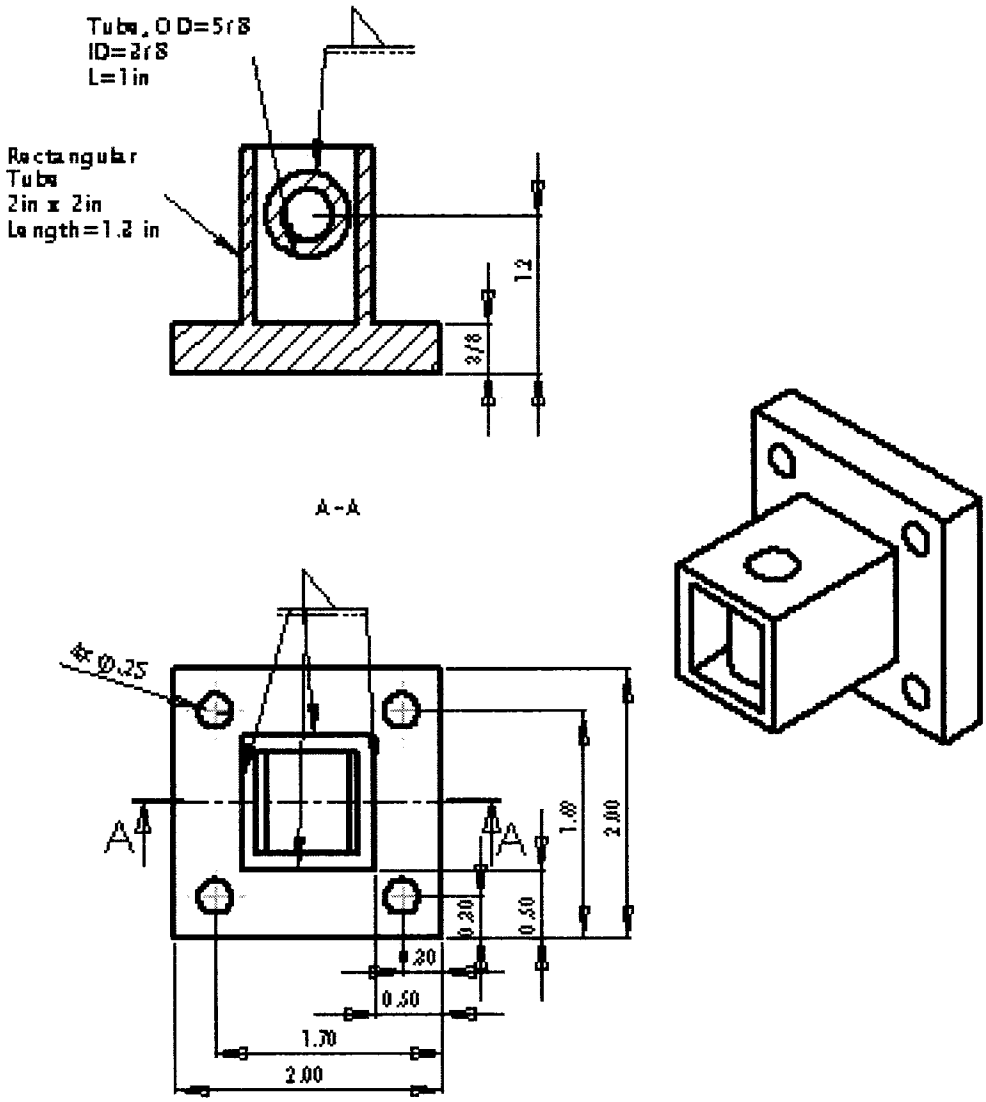

All Dimensions are in Inches	XX ±.02 XXX ±.01 XXXX ±.005	Part Number: 23
		subassembly
	Cold Finish Steel	Supporter_short

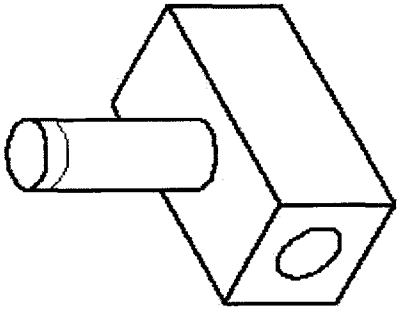

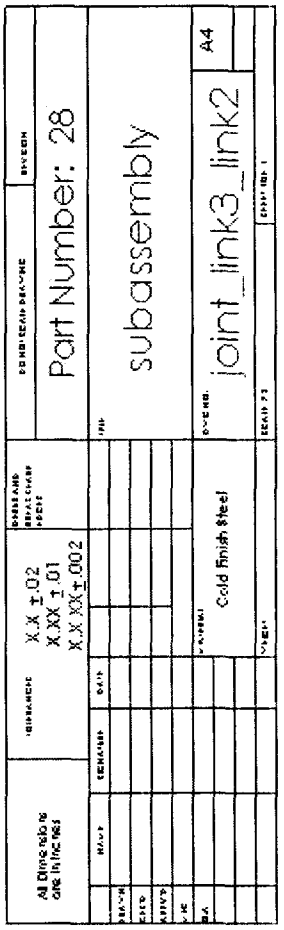

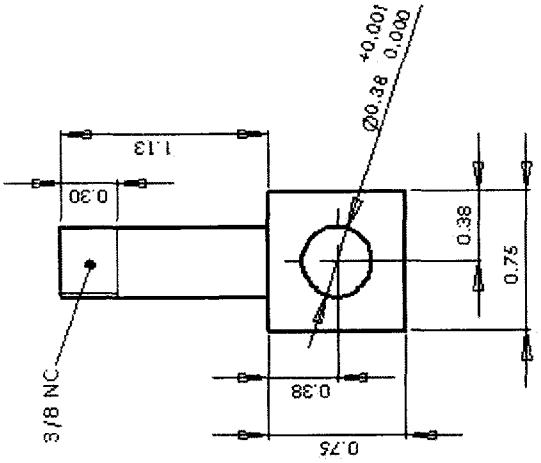

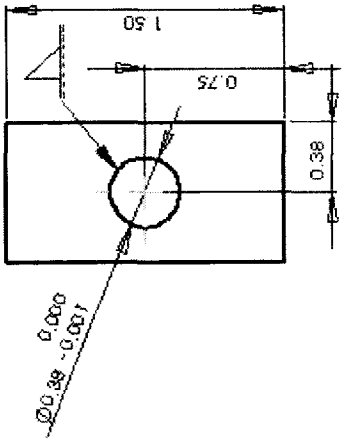

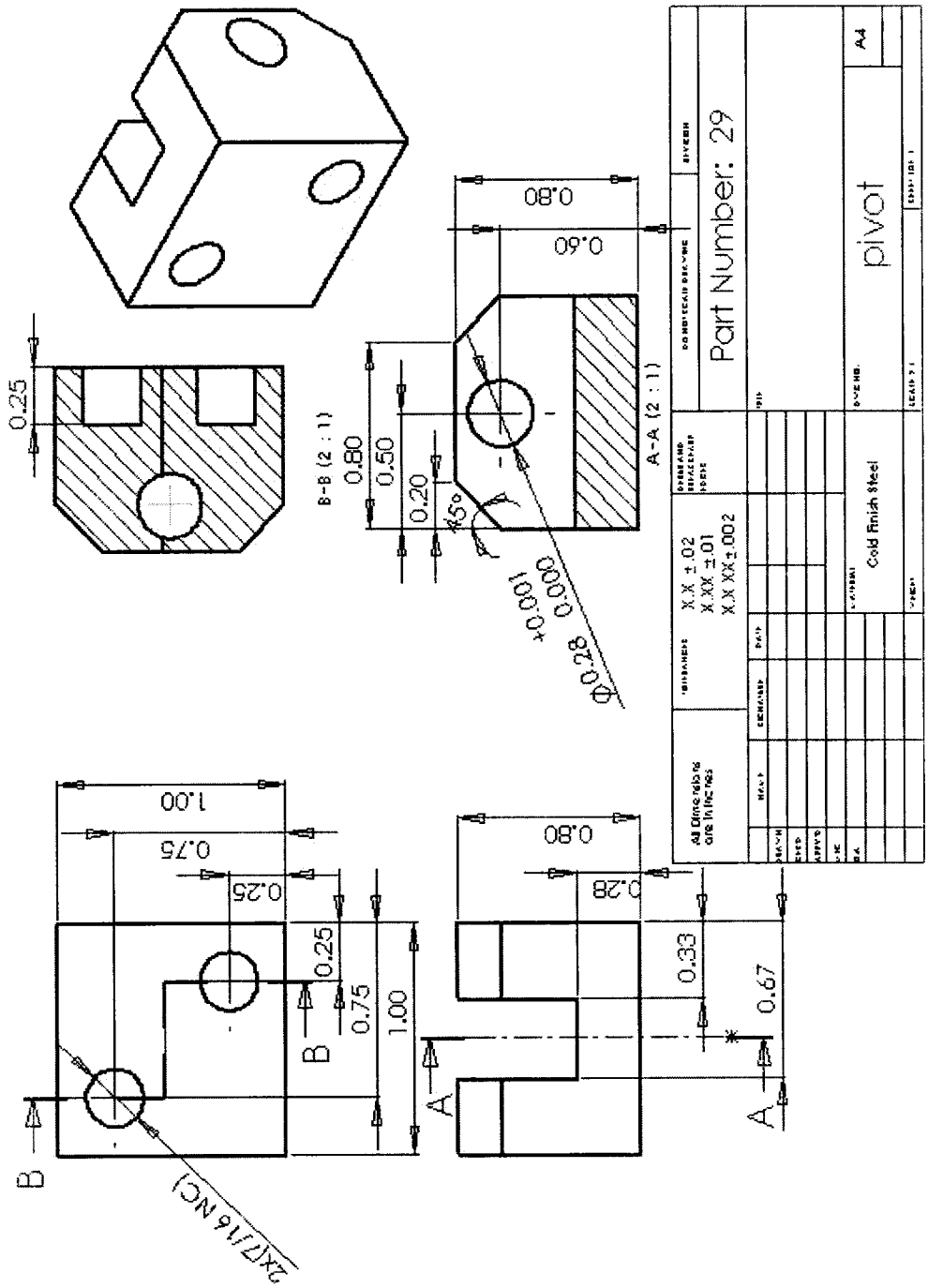

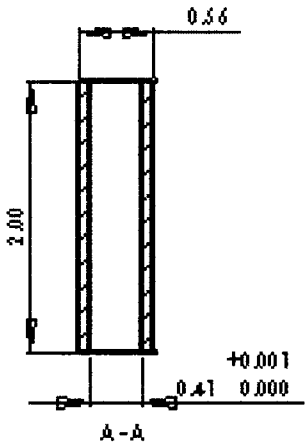

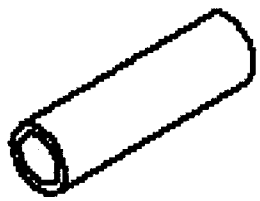

All Dimensions are in Inches						XX ± .02 XXX ± .01 XXXX ± .005	Part Number: 34
						Brass	circular bushing

Appendix B

Derivation of Basic Equation for Air spring Nonlinear Model

The ultimate goal of this Appendix is to derive an equation which relates the supplier pressure to the air spring static pressure. It is assumed that gas is flowing through an orifice with a cross section equal to A_{12} , with a speed equal to u_2 and a static pressure equal to P_2. Equation B.1 states the stagnation pressure (P_1) as a function of static pressure and gas flow velocity [46].

$$P_1 = P_2(1+\frac{\gamma-1}{2g\gamma RT_1}u_2{}^2)^{\frac{-\gamma}{\gamma-1}} \qquad \text{B.1}$$

In this Appendix, It is shown that if the process is assumed to be polytropic, the equation B.1 is valid also for the supplier pressure and the air spring pressure except for γ which is replaced by "n" a number between 1 and 4.

Equation B.2 is Bernoulli equation connecting the gradient of the fluid pressure $\nabla\vec{P}$ to the fluid density " ρ "and its acceleration " $\vec{a}$ ".

$$-\nabla\vec{P} - p\vec{K} = \frac{\rho\vec{a}}{g} \qquad \text{B.2}$$

Considering the pressure component in the direction of the gas flow, Equation B.2 can be written in the following form:

$$\frac{dP}{\rho}+\frac{1}{2g}d(u^2)=0 \qquad \text{B.3}$$

where u is the gas flow velocity.

Assuming a polytrophic process and considering air as an ideal gas, the relationship between the pressure and density can be written as follows:

$$\frac{P}{\rho^n} = a = \text{constant} \qquad \text{B.4}$$

Solving Euation B.4 for ρ yields:

$$\rho = \frac{P^{\frac{1}{n}}}{a^{\frac{1}{n}}} \qquad \text{B.5}$$

Substituting Equation B.4 into Equation B.3 gives:

$$a^{\frac{1}{n}} \frac{dP}{P^{\frac{1}{n}}} + \frac{1}{2g} d(u^2) = 0 \qquad \text{B.6}$$

Taking integrator from both sides of Equation B.6 yields:

$$a^{\frac{1}{n}} \frac{n}{n-1} P^{\frac{n-1}{n}} + \frac{1}{2g} u^2 = const \qquad \text{B.7}$$

The air flow velocity in the supplier is zero and at the orifice cross section is u_2. Writing Equation B.7 for these two points, the relationship between the air spring and the supplier states is obtained in terms of "a".

$$a^{\frac{1}{n}} \frac{n}{n-1} P_2^{\frac{n-1}{n}} + \frac{1}{2g} u_2^2 = a^{\frac{1}{n}} \frac{n}{n-1} P_1^{\frac{n-1}{n}} + \frac{1}{2g}(0)^2 \Rightarrow P_1^{\frac{n-1}{n}} = P_2^{\frac{n-1}{n}} + \frac{n-1}{2gna^{\frac{1}{n}}} u_2^2 \qquad \text{B.8}$$

Considering the ideal gas relation between the gas pressure, temperature and density:

$$P = \rho RT \qquad \text{B.9}$$

Subsisting ρ from Equation B.5 into Equation B.9 and rearranging gives:

$$a^{\frac{1}{n}} = RTP^{\frac{1-n}{n}} \qquad \text{B.10}$$

Substituting Equation B.10 into Equation B.8 and solving the obtained equation for P_1 gives:

$$P_1^{\frac{n-1}{n}} = P_2^{\frac{n-1}{n}} + \frac{n-1}{2gnRT_1} P_1^{\frac{n-1}{n}} u_2^2$$

Solving this equation for P_1 yields:

$$P_1 = P_2 \left(1 + \frac{n-1}{2gnRT_1} u_2^2\right)^{\frac{-n}{n-1}} \qquad \text{B.11}$$

Therefore, in order to obtain Equation B.11, the following assumptions are considered:

1. Air is assumes to be an ideal gas.
2. The process is assumed to be a polytrophic process.
3. The air velocity at the supplier is zero

Appendix C

Sensor Calibration

Calibration of the LVDT was carried out on an experimental setup built to accurately measure the LVTD's displacements using a micrometer. Different displacements and the corresponding voltage measured were recorded. In order to reduce the noise affect, the voltage was read 100 times for each displacement and the mean value is recorded.

The displacement-voltage data are shown in Figures C.1 and C.2 for the LVDT's connected to the air spring piston and the load respectively. The linear regressions lines of the two data sets are also shown on the respective graphs, their equation are given respectively by:

$$y_{input} = -106.41V + 5.63 \text{ inch} \quad \text{C.1}$$

$$y_{output} = -1.151V + 9.82 \text{ inch} \quad \text{C.2}$$

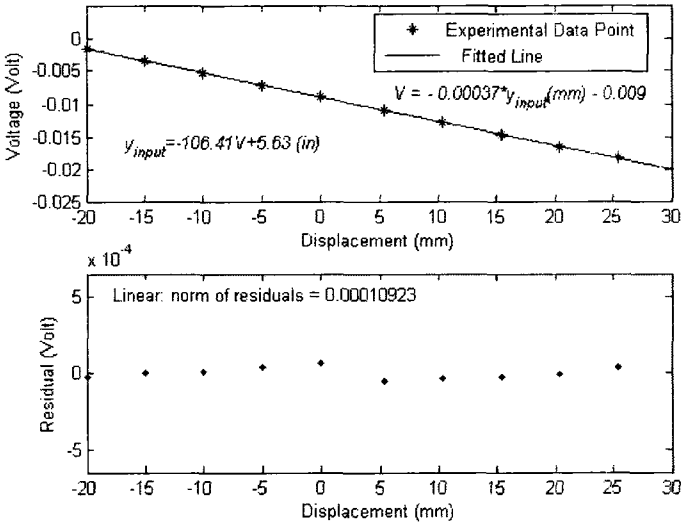

Figure 5.2: Input LVDT Calibration Curves

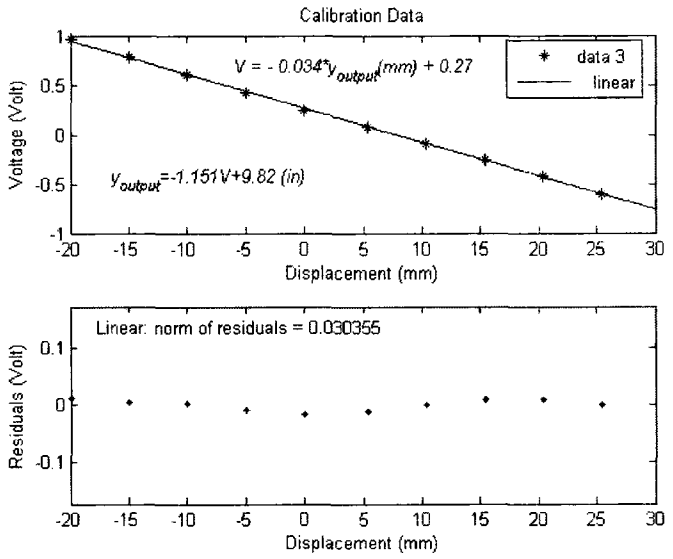

Figure 5.3: Output LVDT Calibration Curves

where y_{input} and y_{output} are the input and the output LVDT displacement, respectively, and V is the output voltage. As the figure shows the data are fitted on lines with small residuals.

A Sensata pressure transducer model 63CP is used to measure the air spring pressure. The transducer output voltage changes from 0.5 to 4.5 volts when the pressure changes from 0 psig to 100 psig, therefore the equation relating the pressure to the voltage is given by:

$$p = 25V - 12.5 \qquad \text{C.3}$$

The accuracy and linearity of this relationship was experimentally verified.